

NASA CR-182218

MTI 89TR6

Contractor Final Report

---

# SPACE POWER FREE-PISTON STIRLING ENGINE SCALING STUDY

---

Prepared for:

NASA-Lewis Research Center  
21000 Brookpark Road  
Cleveland, Ohio 44135

Prepared under:

Contract NAS3-25148

Prepared by:

Mechanical Technology Incorporated  
968 Albany-Shaker Road  
Latham, New York 12110

1 October 1989



# TABLE OF CONTENTS

SECTION	PAGE
LIST OF FIGURES .....	ix
LIST OF TABLES .....	xiii
1.0 INTRODUCTION .....	1-1
1.1 Introduction and Summary .....	1-1
1.2 Conclusions .....	1-6
1.3 Recommendations .....	1-9
2.0 ENGINE CONCEPT EVALUATION AND SELECTION .....	2-1
2.1 Design Requirements .....	2-1
2.2 Engine Concepts .....	2-1
2.2.1 Modular Heat Exchangers .....	2-2
2.2.2 Radial-Flow Heat Exchangers .....	2-7
2.3 Scaling Considerations .....	2-13
2.3.1 Structural Aspects .....	2-13
2.3.2 Thermodynamic Aspects .....	2-15
2.3.3 Heat Pipes .....	2-15
2.3.4 Alternator .....	2-15
2.3.5 Dynamic Balancer .....	2-15
2.4 Concept Comparisons .....	2-15
2.4.1 Engine Geometry .....	2-16
2.4.2 Performance .....	2-20
2.4.3 Specific Mass .....	2-21
2.4.4 Scalability .....	2-21
2.4.5 Risk .....	2-23
2.5 Concept Selection .....	2-23
3.0 DESIGN FEASIBILITY OF 150-kW <sub>e</sub> FPSE/LA RADIAL-FLOW ENGINE DESIGN. ....	3-1
3.1 Pressure Vessel Assembly .....	3-1
3.2 Displacer Drive Assembly .....	3-8
3.3 Heat Exchanger Assembly .....	3-11
3.4 Heat Transport Systems .....	3-13
3.4.1 Heater Heat Pipes .....	3-13
3.4.2 Coolant System .....	3-16
3.5 Alternator Assembly and Power Piston .....	3-16
3.6 Dynamic Balancer Assembly .....	3-18
4.0 PARAMETRIC STUDY .....	4-1
4.1 Parametric Study Requirements and Procedure .....	4-1
4.2 Power Module Analysis .....	4-2
4.2.1 Engine Thermodynamics and Dynamics .....	4-2
4.2.2 Thermal Analysis .....	4-9
4.2.3 Alternator Analysis .....	4-14
4.2.4 Dynamic Balancer Analysis .....	4-31

PRECEDING PAGE BLANK NOT FILMED

II III IV

DATA IV INTERNATIONALLY BLANK

## TABLE OF CONTENTS (Continued)

SECTION	PAGE
4.3 Results .....	4-40
4.3.1 General Performance Characteristics .....	4-40
4.3.2 Heat Exchanger Temperature Ratio Sensitivity .....	4-40
4.3.3 Power Level Sensitivity .....	4-44
4.3.4 Results for Opposed Power Modules Without Dynamic Balancer .....	4-44
4.4 Empirical Equation - Empirical Relationship Between System Thermal Efficiency and System Specific Mass, System Power Output, and Temperature Ratio .....	4-59
5.0 ALTERNATIVE CONFIGURATIONS .....	5-1
5.1 Multicylinder Arrangement .....	5-1
5.1.1 Renia Configuration FPSE/LA Description .....	5-1
5.1.2 Thermodynamics .....	5-3
5.2 Alternative Power Takeoff .....	5-3
6.0 MAXIMUM ACHIEVABLE POWER LEVEL PER CYLINDER .....	6-1
6.1 Task Objective .....	6-1
6.2 Summary .....	6-1
6.3 Technical Discussion .....	6-1
6.3.1 Seal Clearances .....	6-1
6.3.2 Ratio of Bearing Length to Diameter .....	6-5
6.3.3 Heat Pipes .....	6-5
6.3.4 Heat Exchanger Relative Location .....	6-5
6.3.5 Vibration Absorber .....	6-5
6.3.6 Alternator .....	6-8
6.4 Large-Engine Design Problems .....	6-8
7.0 REFERENCES .....	7-1

## LIST OF FIGURES

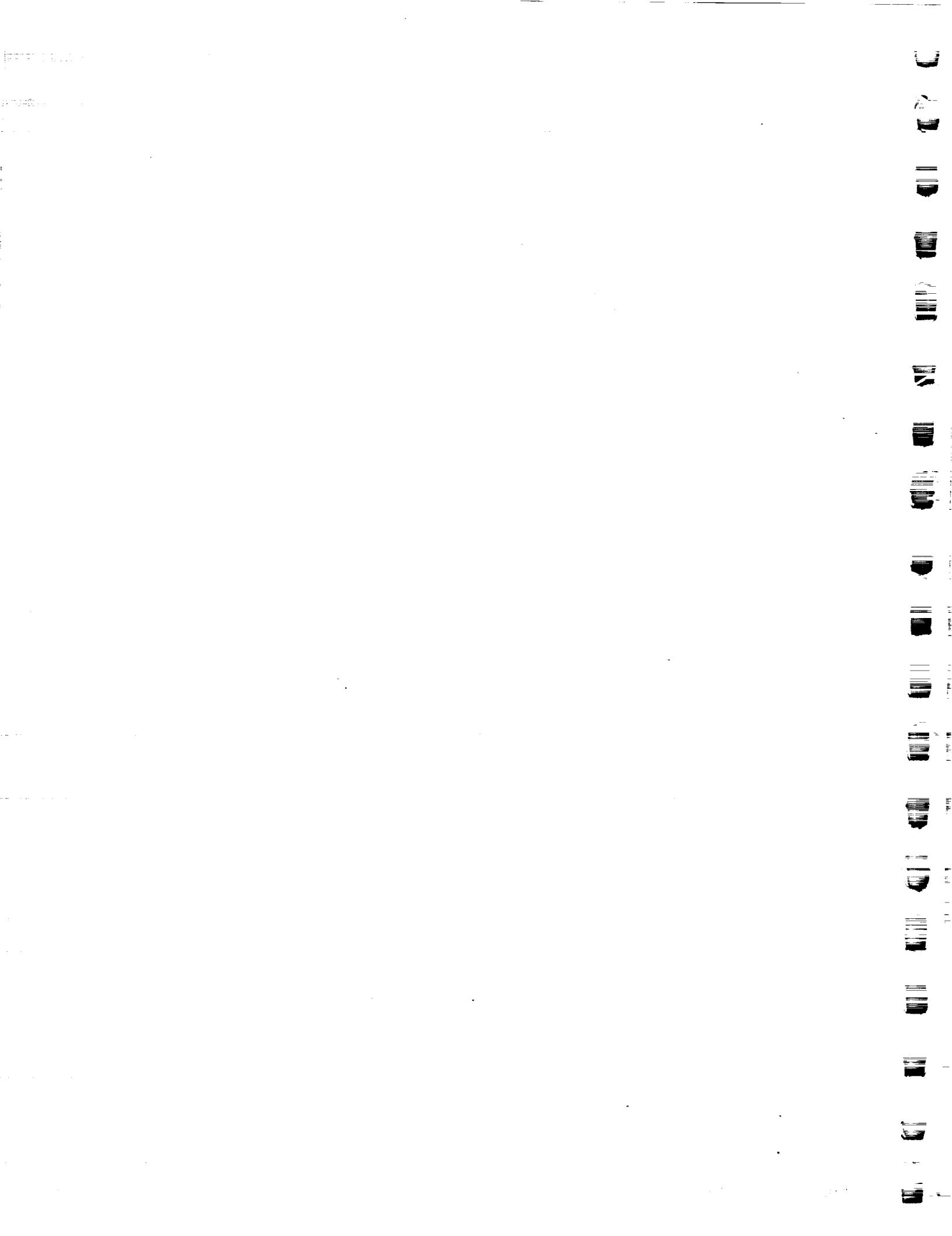
NUMBER		PAGE
1-1	Engine Configuration with Finned Modular Heat Exchangers . . . . .	1-2
1-2	Engine Configuration with Shell-and-Tube Modular Heat Exchangers. . . . .	1-3
1-3	Engine Configuration with Radial-Flow Heat Exchangers. . . . .	1-4
1-4	Conceptual Stirling Space Engine (CSSE) . . . . .	1-5
1-5	Multicylinder Free-Piston Stirling Engine Conceptual Design. . . . .	1-7
1-6	Magnetic Linear-to-Rotary Converter Configuration . . . . .	1-8
2-1	Layout of Annular Design . . . . .	2-3
2-2	Finned Heater Heat-Pipe Schematic . . . . .	2-4
2-3a	Pumped Loop Cooler Concept - Internal Coolant. . . . .	2-5
2-3b	Pumped Loop Cooler Concept - External Coolant . . . . .	2-6
2-4	Finned Module Performance versus Module Diameter and Power. . . . .	2-8
2-5	Finned Module Specific Mass versus Module Diameter and Power Level. . . . .	2-9
2-6	Finned Module Heater Wall Temperature Drop versus Module Diameter and Power Level . . . . .	2-10
2-7	Shell-and-Tube Module Performance versus Module Diameter and Power Level . . . .	2-11
2-8	Shell-and-Tube Module Specific Mass versus Module Diameter and Power Level . . .	2-12
2-9	Radial Engine Heat Exchanger Detail . . . . .	2-14
2-10	Power Module Efficiency and Specific Mass versus Net Power . . . . .	2-22
2-11	Branched Heat-Pipe Heater Arrangement in Radial Engine . . . . .	2-24
3-1	150-kW <sub>e</sub> Free-Piston Stirling Engine/Linear Alternator. . . . .	3-2
3-2	Materials for Space Power Free-Piston Stirling Engine Scaling Study. . . . .	3-3
3-3	Stress-Rupture Data Extrapolated from 1000-hr Data Using Larson-Miller Parameter .	3-4
3-4	Yield Strength - High-Temperature Alloy . . . . .	3-5
3-5	Bimetallic (Inco-625/Inco-718) Hot-End Pressure Vessel . . . . .	3-6
3-6	Inco-713 Hot-End Pressure Vessel with Lock Joint . . . . .	3-7
3-7	Typical Displacer Drive Design . . . . .	3-9
3-8	Coupling Detail for Hydrodynamic Gas Bearings . . . . .	3-10
3-9	Segmented Regenerator Wall Concept Schematic . . . . .	3-12
3-10	Ideal Heat Pipe Based on Engine Heater Requirements . . . . .	3-14
3-11	Compression-Creep Curves as Compared to Tension-Creep Curve for Udimet 700 . .	3-15
3-12	Radial Engine Cooler Coolant Flow Schematic . . . . .	3-17
4-1	150-kW <sub>e</sub> Radial Engine Indicated Efficiency versus Hot-to-Cold Volume Amplitude Ratio . . . . .	4-4
4-2	150-kW <sub>e</sub> Baseline Design. Indicated Efficiency versus Displacer-to-Piston Phase Angle. . . . .	4-5
4-3	150-kW <sub>e</sub> Baseline Design. Normalized Power versus Displacer-to-Piston Phase Angle. . . . .	4-6
4-4	Power Module Specific Mass and Efficiency versus Engine Mean Pressure . . . . .	4-8
4-5	Power Module Efficiency and Specific Mass versus Operating Frequency . . . . .	4-10
4-6	Diagram of an Arterial Heat Pipe with Sintered Powder Wick and Arteries . . . . .	4-11
4-7	Power Transport Limits of a 2.22-cm ID Sodium Heat Pipe as a Function of Heat Pipe Vapor Temperatures . . . . .	4-12
4-8	Heat-Pipe Performance Limits versus Heat-Pipe Diameter . . . . .	4-13
4-9	NaK Bulk Temperature Drop versus NaK Mass Flow . . . . .	4-15

## LIST OF FIGURES (Continued)

NUMBER		PAGE
4-10	NaK Film Temperature Drop versus NaK Mass Flow as a Function of Coolant Tube Diameter . . . . .	4-16
4-11	NaK Pump Head versus Flow Rate as a Function of Coolant Tube Diameter . . . . .	4-17
4-12	Total NaK Flow Loss Including Entrance/Exit and Manifolds versus NaK Mass Flow as a Function of Coolant Tube Diameter. . . . .	4-18
4-13	150-kW <sub>e</sub> Baseline Alternator . . . . .	4-23
4-14	Radial Flux Density in Gap versus Axial Position . . . . .	4-24
4-15	Radial Flux Density Outside of Coil versus Axial Position . . . . .	4-25
4-16	Axial Flux Density Across Segment No. 1 Center versus Radial Position . . . . .	4-26
4-17	Axial Flux Density Across Segment No. 2 Center versus Radial Position . . . . .	4-27
4-18	150-kW <sub>e</sub> Baseline Alternator . . . . .	4-28
4-19	Radial Flux Density in Gap versus Axial Position . . . . .	4-29
4-20	Radial Flux Density Outside of Coil versus Axial Position . . . . .	4-30
4-21	Axial Flux Density Across Segment No. 1 Center versus Radial Position . . . . .	4-32
4-22	Axial Flux Density Across Segment No. 2 Center versus Radial Position . . . . .	4-33
4-23	150-kW <sub>e</sub> Alternator . . . . .	4-34
4-24	Plunger at Position of Maximum Stator Flux Density - Radial Flux in Outer Stator versus Axial Location . . . . .	4-35
4-25	Dynamic Balancer Analytical Model and Governing Equation . . . . .	4-36
4-26	Power Module Casing Vibration versus Balancer Loss . . . . .	4-37
4-27	Balancer Total Specific Mass versus Required Casing Vibration Amplitude. . . . .	4-39
4-28	150-kW <sub>e</sub> Power Module Parametric Study Performance Map . . . . .	4-41
4-29	75-kW <sub>e</sub> Power Module Parametric Study Performance Map . . . . .	4-42
4-30	25-kW <sub>e</sub> Power Module Parametric Study Performance Map . . . . .	4-43
4-31	Power Module Relative Efficiency versus Net Power . . . . .	4-45
4-32	Power Module Specific Mass versus Net Power . . . . .	4-46
4-33	150-kW <sub>e</sub> Power Module (Temperature Ratio = 2.0) Optimized for Maximum Efficiency/Specific Mass. Performance and Specific Mass Summary . . . . .	4-47
4-34	75-kW <sub>e</sub> Power Module (Temperature Ratio = 2.0) for Maximum Efficiency. Performance and Specific Mass Summary . . . . .	4-48
4-35	25-kW <sub>e</sub> Power Module (Temperature Ratio = 2.0) Optimized for Maximum Efficiency. Performance and Specific Mass Summary. . . . .	4-49
4-36	150-kW <sub>e</sub> Power Module (Temperature Ratio = 2.0) Optimized for Minimum Specific Mass. Performance and Specific Mass Summary . . . . .	4-50
4-37	150-kW <sub>e</sub> Power Module (Temperature Ratio = 1.7) Optimized for Maximum Efficiency. Performance and Specific Mass Summary. . . . .	4-51
4-38	150-kW <sub>e</sub> Power Module (Temperature Ratio = 2.0) Optimized for Maximum Efficiency. Performance and Specific Mass Summary. . . . .	4-52
4-39	150-kW <sub>e</sub> Power Module (Temperature Ratio = 2.5) Optimized for Maximum Efficiency. Performance and Specific Mass Summary. . . . .	4-53
4-40	150-kW <sub>e</sub> Power Module (Temperature Ratio = 3.0) Optimized for Maximum Efficiency. Performance and Specific Mass Summary. . . . .	4-54
4-41	Power Module Relative Efficiency versus Net Power . . . . .	4-55
4-42	Power Module Specific Mass versus Net Power . . . . .	4-56
4-43	FPSE Scaling Study - Double-Ended Radial Engine with Straight Main Heat Pipes . . . . .	4-57

## LIST OF FIGURES (Continued)

NUMBER		PAGE
4-44	FPSE Scaling Study - Double-Ended Radial Engine with Bent Main Heat Pipes . . . . .	4-58
4-45	Two 150-kW <sub>e</sub> Opposed Power Modules . . . . .	4-60
4-46	Two 75-kW <sub>e</sub> Opposed Power Modules . . . . .	4-61
4-47	Two 25-kW <sub>e</sub> Opposed Power Modules . . . . .	4-62
5-1	Typical Renia Engine Configuration . . . . .	5-2
6-1	500-kW <sub>e</sub> FPSE/LA Layout . . . . .	6-2
6-2	Single-Cylinder Power Module Scaleup Specific Mass versus Power Level . . . . .	6-6
6-3	Single-Cylinder Power Module Scaleup Efficiency versus Power Level . . . . .	6-7

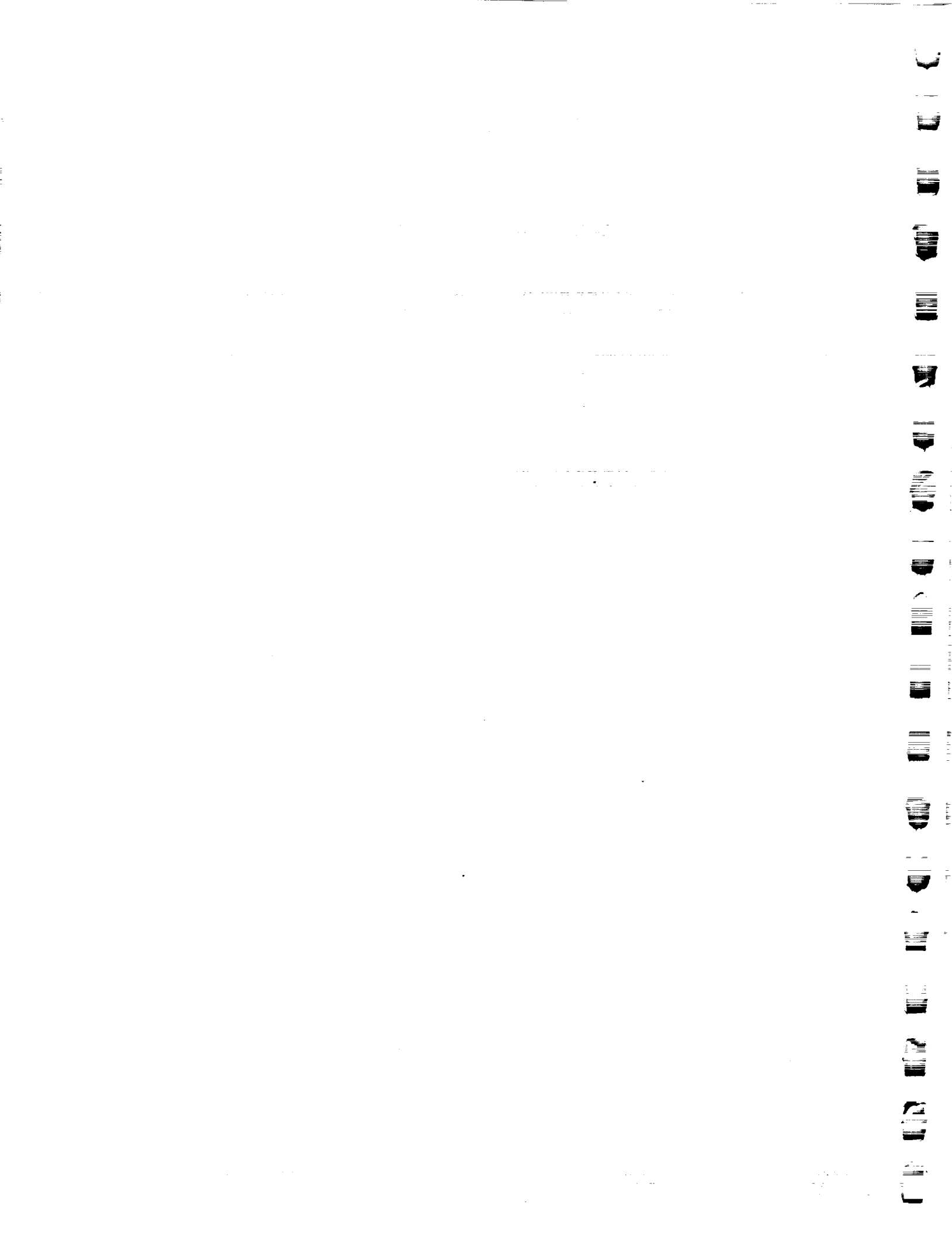




## LIST OF TABLES

NUMBER		PAGE
2-1	Preliminary Engine Geometric Parameters - Used in Concept Selection . . . . .	2-17
2-2	Preliminary Engine Performance Predictions - Used in Concept Selection . . . . .	2-18
2-3	Preliminary Specific Mass Summary - Used in Concept Selection . . . . .	2-19
4-1	Results of Second-Order Alternator Analysis Using LPMMA Computer Program . . . .	4-20
4-2	Results of Third-Order Alternator Analysis Using Flux Computer Program . . . . .	4-22
4-3	Dynamic Balance Unit - Performance and Mass Penalties . . . . .	4-38
4-4	Empirical Equation for Power Module Performance . . . . .	4-64
4-5	Empirical Equation Coefficients . . . . .	4-65
4-6	Empirical Equation and Coefficients for Power Module Performance Operating at Specified Power Levels . . . . .	4-66
5-1	Multicylinder FPSE/LA (Renia Configuration) Summary . . . . .	5-4
5-2	FPSE with Magnetic Coupling and Rotary Alternator - Summary . . . . .	5-6
6-1	500-kW <sub>e</sub> Power Module Operating Conditions and Geometry . . . . .	6-3
6-2	500-kW <sub>e</sub> Power Module Performance Summary . . . . .	6-4

PRECEDING PAGE BLANK NOT FILMED



## 1.0 INTRODUCTION

### 1.1 Introduction and Summary

This work was completed as part of the NASA CSTI High-Capacity Power Program on Conversion Systems for Nuclear Applications. The NASA effort is part of the overall SP-100 program, which is a combined DOD/DOE/NASA program to develop nuclear power for space. Stirling engines have been identified as a growth option for the SP-100 power system, offering increased power output and lower system mass and radiator area.

The free-piston Stirling engine (FPSE) is a candidate power conversion unit for space-power applications using either nuclear or solar heat sources. NASA-Lewis Research Center (NASA-LeRC) is funding design and development programs for 25 kW-electric (kW<sub>e</sub>) FPSEs, which represent the highest power output FPSE systems to date. The need for even higher output FPSEs exists for use in space-power systems requiring increasing amounts of electrical power. This space-power module scaling study had two main objectives. The first objective was to determine the design feasibility of a single-cylinder FPSE with a linear alternator (LA) producing 100 to 150 kW<sub>e</sub>. The second objective was to determine the parametric relationships between efficiency, specific mass, power output, and temperature ratio for a power output range of 25 to 150 kW<sub>e</sub> and a temperature ratio range of 1.7 to 3.0.

This introductory section of the report summarizes work done in the study, and presents the main conclusions. Recommendations are then made for future work needed to address key technology areas and for continued design work on high-power FPSE/LA power systems.

Three engine concepts were considered for the study: two designs with modular heat exchangers (as shown in Figures 1-1, 1-2), and a new design with radial-flow heat exchangers (depicted in Figure 1-3), which was ultimately selected.

All of the concepts use sodium heat-pipe heat transport to the heater, and NaK (sodium-potassium eutectic mixture) pumped loop heat rejection from the cooler. The modular heat exchanger engine concepts were derivative of the conceptual Stirling Space Engine (CSSE) 25-kW<sub>e</sub> power module design [1]\* (see Figure 1-4). The CSSE design featured modular heat exchangers connected to the engine expansion and compression spaces via ducts. The heater heat pipes are externally finned with the engine gas flowing between fins, parallel to the heat pipe axis. The regenerator is a full disk, and the cooler is similar to the heater, but with NaK flowing over the outside of the module.

The first concept considered in this study (see Figure 1-1) is similar to the CSSE design, but is modified by using separate ducts to the modules to reduce thermal stresses. The second modular heat exchanger concept (see Figure 1-2) improved thermodynamic performance by using a shell-and-tube-type heater and cooler. The heater heat pipe uses condensing sodium on the shell side of the heater tubes, with wicks on each tube connected with a "wick-bridge" to carry the condensate back to the heat-pipe evaporator. The cooler is a NaK pumped loop on the shell side, but can also use a heat-pipe arrangement similar to the heater.

The radial-flow heat exchangers of the third engine concept, as shown in Figure 1-3, are constructed with stacks of thin metal plates to form rectangular channels through which the engine working fluid flows. The plates act as fins to conduct heat between the heat source or sink and the engine working fluid. This design features large heat exchanger frontal area and a relatively small hot-end pressure vessel. It can be scaled up to 150-kW<sub>e</sub> power output by radial and axial extension of the heat exchangers, along with an

---

\*Numbers in brackets indicate references listed in Section 7.0.

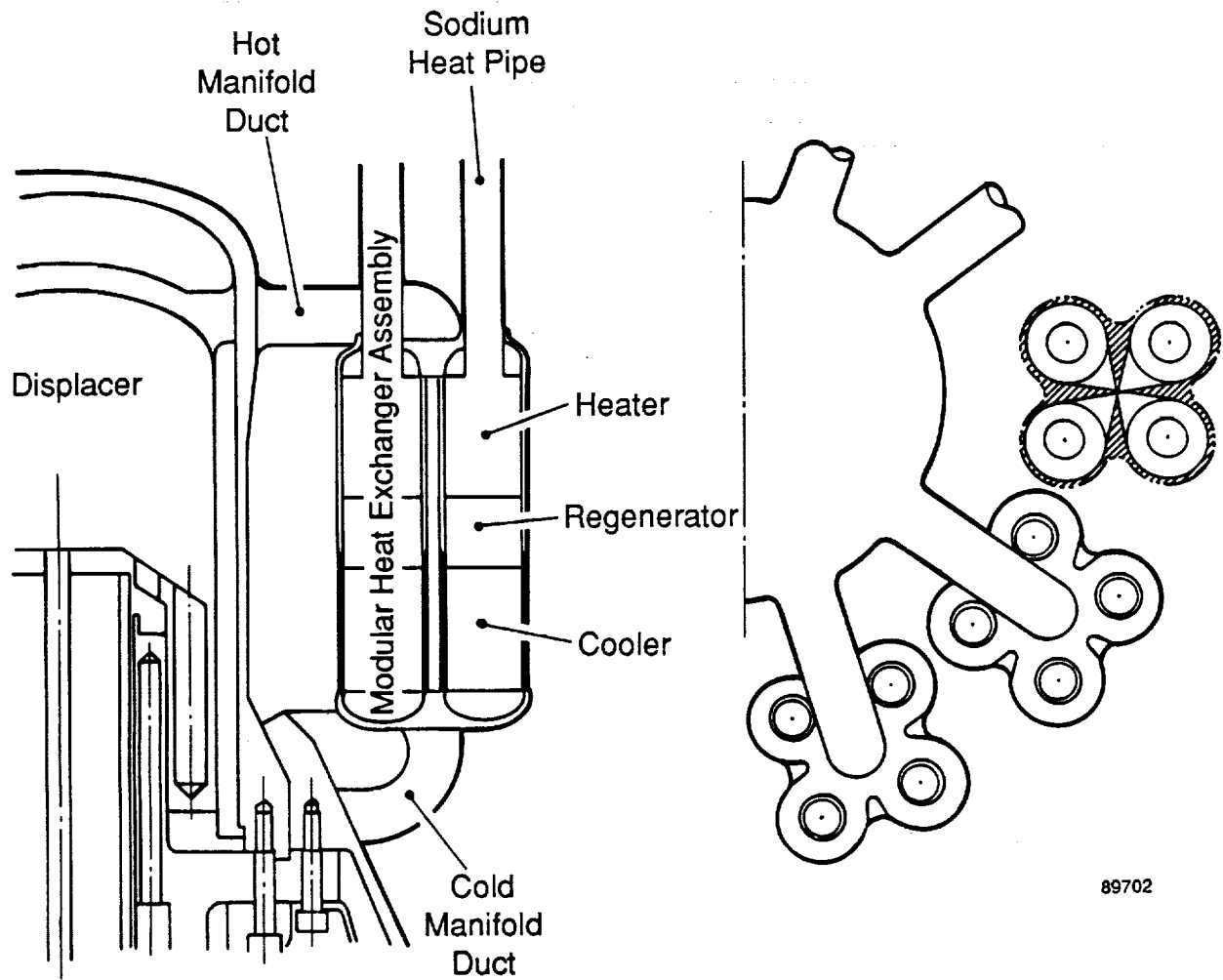
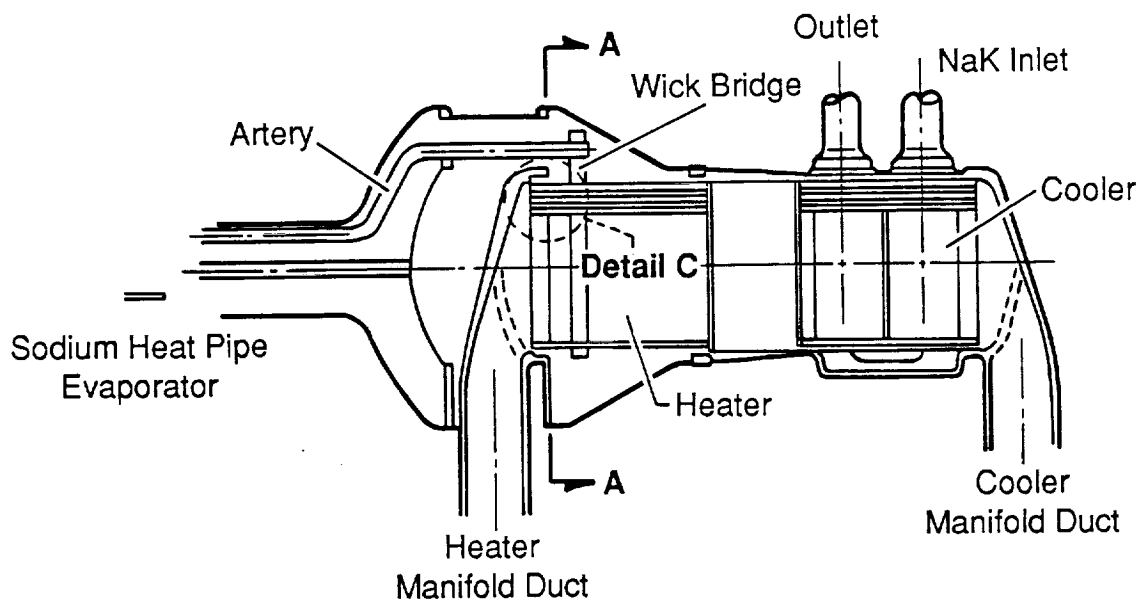
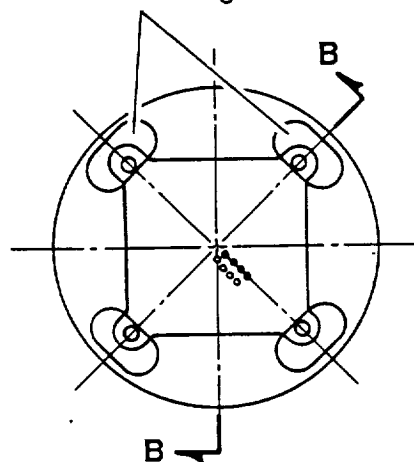


Figure 1-1. Engine Configuration with Finned Modular Heat Exchangers

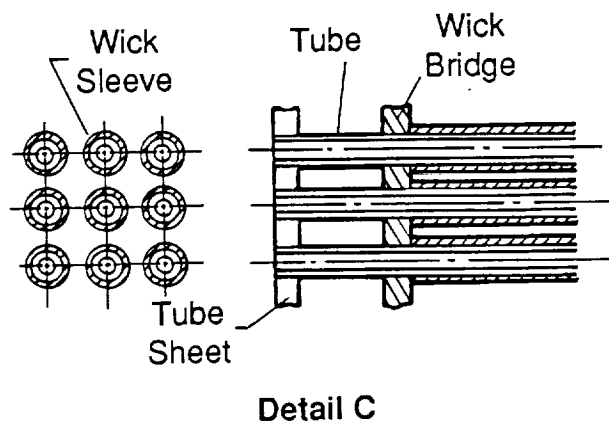


Section B-B

Sodium Passages



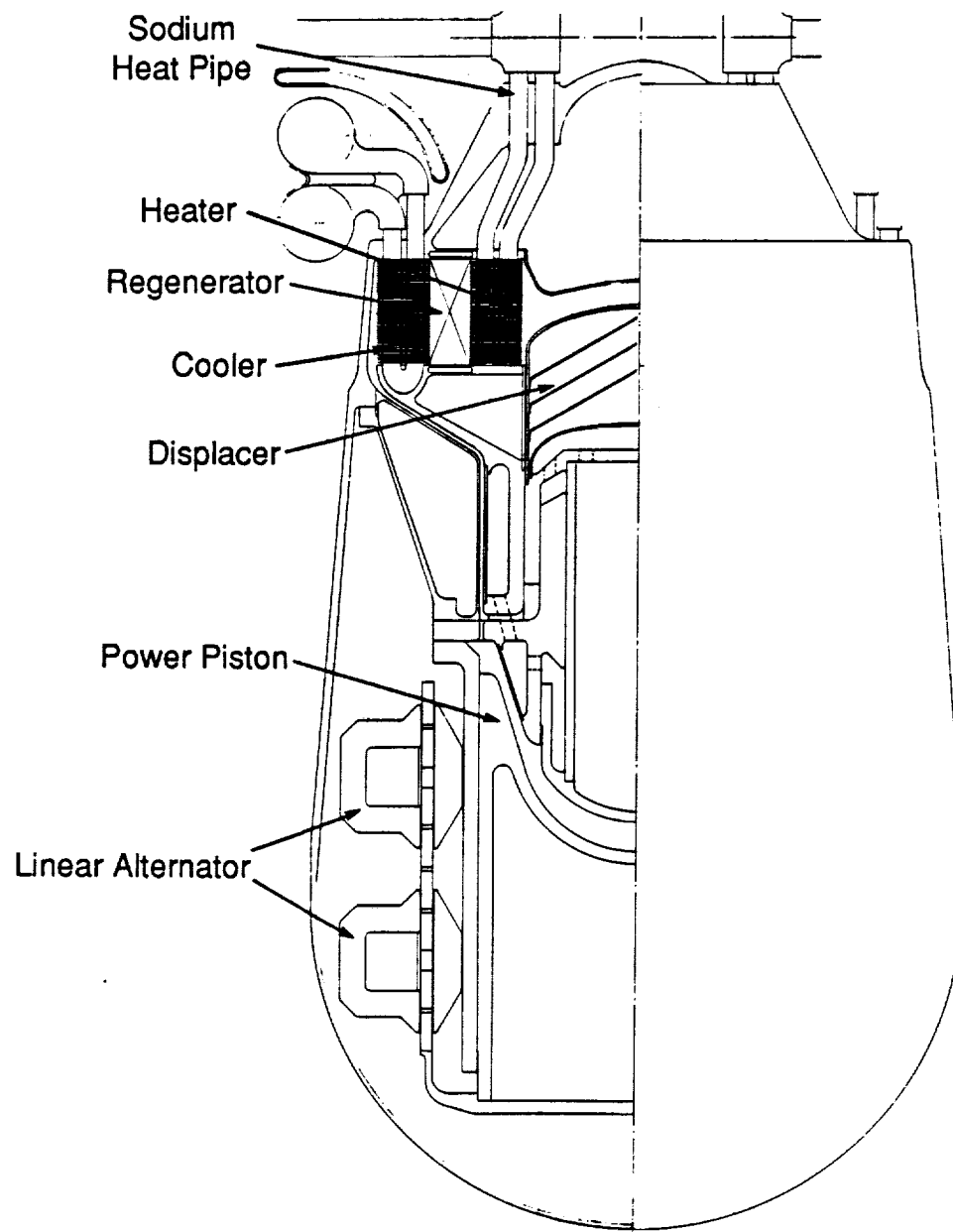
Section A-A



Detail C

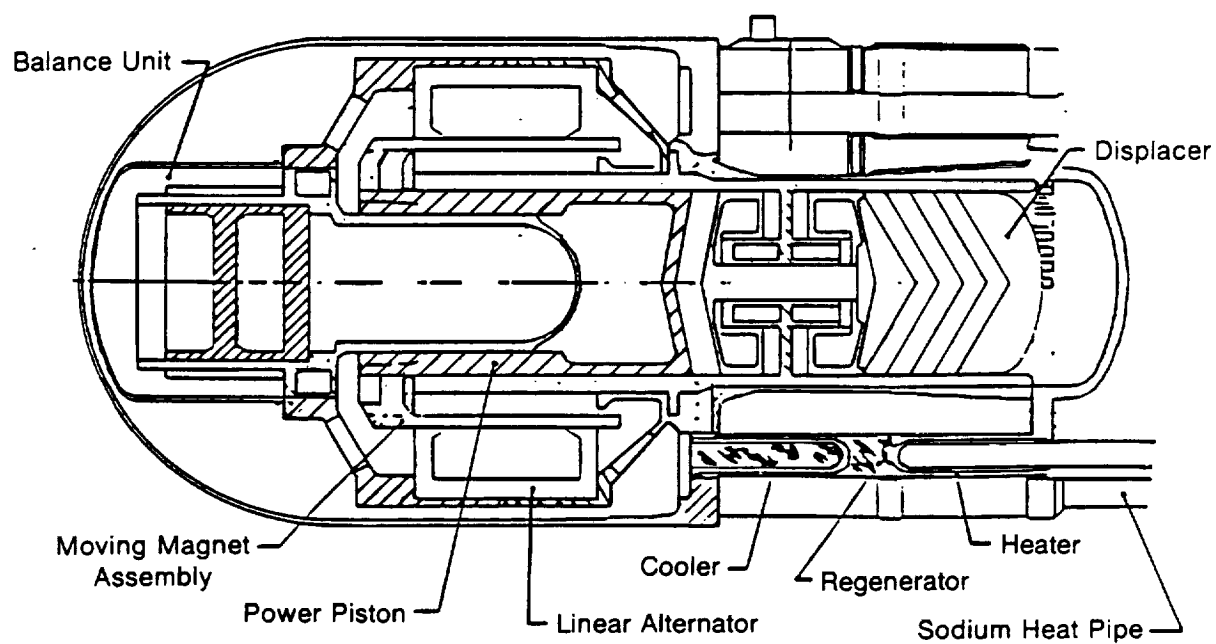
89767

Figure 1-2. Engine Configuration with Shell-and-Tube Modular Heat Exchangers



881173

Figure 1-3. Engine Configuration with Radial-Flow Heat Exchangers



881246

Figure 1-4. Conceptual Stirling Space Engine (CSSE)

increase in displacer, power piston, and alternator diameters. Consistent performance and specific mass are attained over a power range of 25 to 150 kW<sub>e</sub>.

A detailed description of these concepts and a comparison of predicted performance is provided in Section 2.0. All of the concepts were able to meet design requirements at power levels up to 150 kW<sub>e</sub> at a heat exchanger temperature ratio of 2.0. The radial design presented the most favorable trends of efficiency and specific mass with increasing power level, displaying moderate material and fabrication risks.

Details of the radial-flow engine design are provided in Section 3.0, which contains descriptions of the heat exchangers and heat transport systems, mechanical drive systems, linear alternator, dynamic balancer, and pressure vessel.

The parametric study forms the core of the scaling study, with 36 power module optimizations performed over a power output range from 25 to 150 kW<sub>e</sub> at heat exchanger temperature ratios from 1.7 to 3.0. Section 4.0 discusses the power module analyses performed in support of the study. The parametric study results are presented in the form of power module thermal efficiency versus power module specific mass, with power output and heat exchanger temperature ratio as parameters. The results of the study are fit by an empirical equation to be used as an input in future system studies.

To conclude the technical study of FPSE power modules capable of delivering 150 kW<sub>e</sub>, alternative configurations to the single-cylinder, direct-coupled linear alternator approach were evaluated and compared to the baseline concept. The results of this work are covered in Section 5.0. Based on the scope of the program, this task was limited to brief evaluation of only two configurations: a multicylinder Renia configuration FPSE, depicted in Figure 1-5, and a rotary alternator connected to the baseline 150-kW<sub>e</sub> FPSE engine through a magnetic coupling (see Figure 1-6). The multicylinder arrangement showed potential for lower specific mass than the baseline single-cylinder configuration, but the requirement for a low-loss appendix gap seal increases the design complexity. The indirect-connected configuration does not offer significant performance or weight improvements, and requires a linear displacer motor for power module stability.

The single-cylinder FPSE/LA is considered the best design approach. Further potential performance improvements may be achieved through use of a balanced opposed engine configuration to eliminate the penalties associated with the dynamic balance unit.

The parametric study results indicate that single-cylinder power modules meeting the design requirements can be designed for power levels greater than 150 kW<sub>e</sub>. To determine the maximum feasible power output, NASA elected to perform an optional task in the contract. The results of this work, reported in Section 6.0, show that a single-cylinder power module operating at a temperature ratio of 2.0 can be scaled in size from 150 kW<sub>e</sub> up to 500 kW<sub>e</sub>, but with declining efficiency and increasing specific mass.

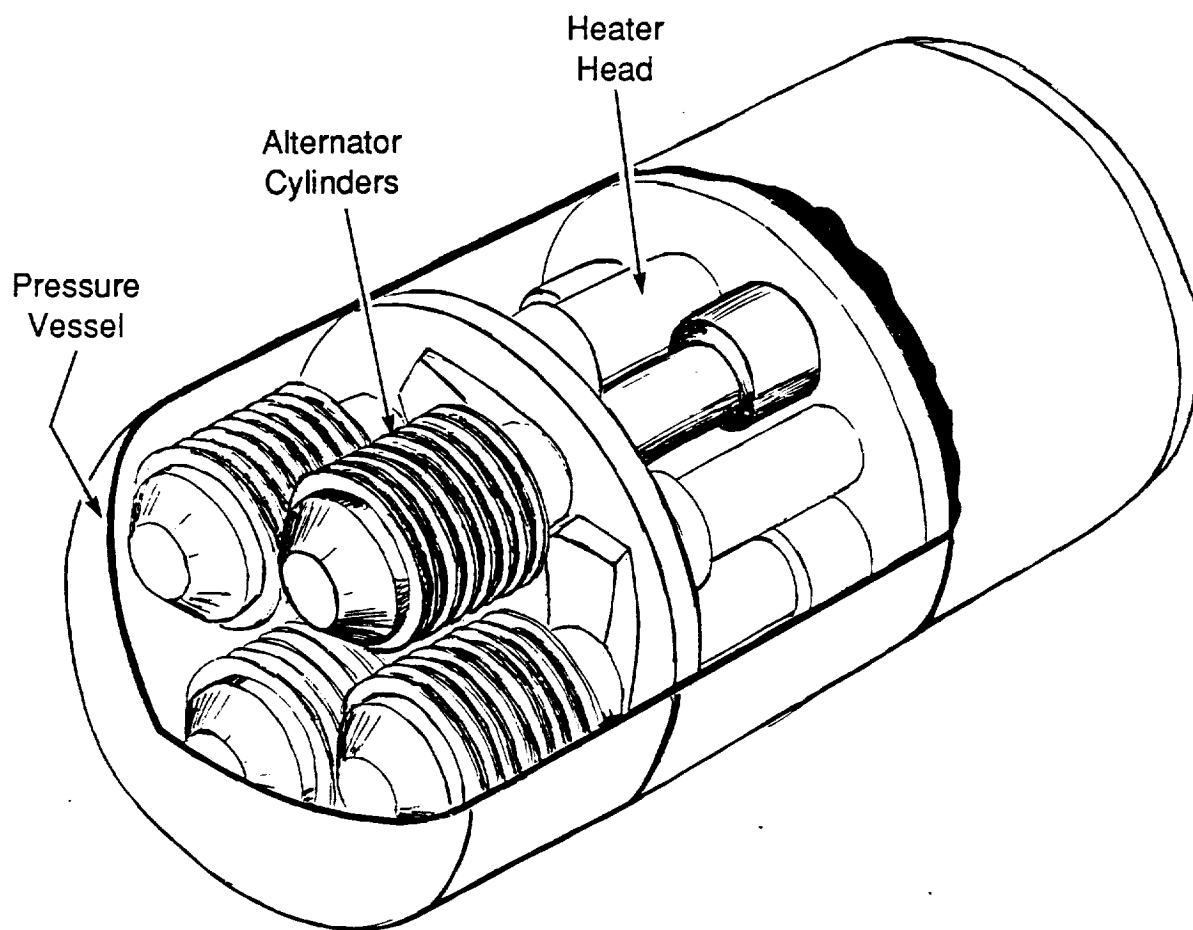
## 1.2 Conclusions

The performance and specific mass values generated by this study are based on conceptual designs, but considerable effort was made to analyze the power module in sufficient detail to reduce uncertainties in mass calculations to a 5 to 10% level. Engine performance calculations have a 10% uncertainty due to the differences between the actual three-dimensional flow in Stirling engine heat exchangers and the one-dimensional analysis used for the thermodynamic model of the engine.

The main conclusions drawn from the design work and results of the scaling study are summarized below:

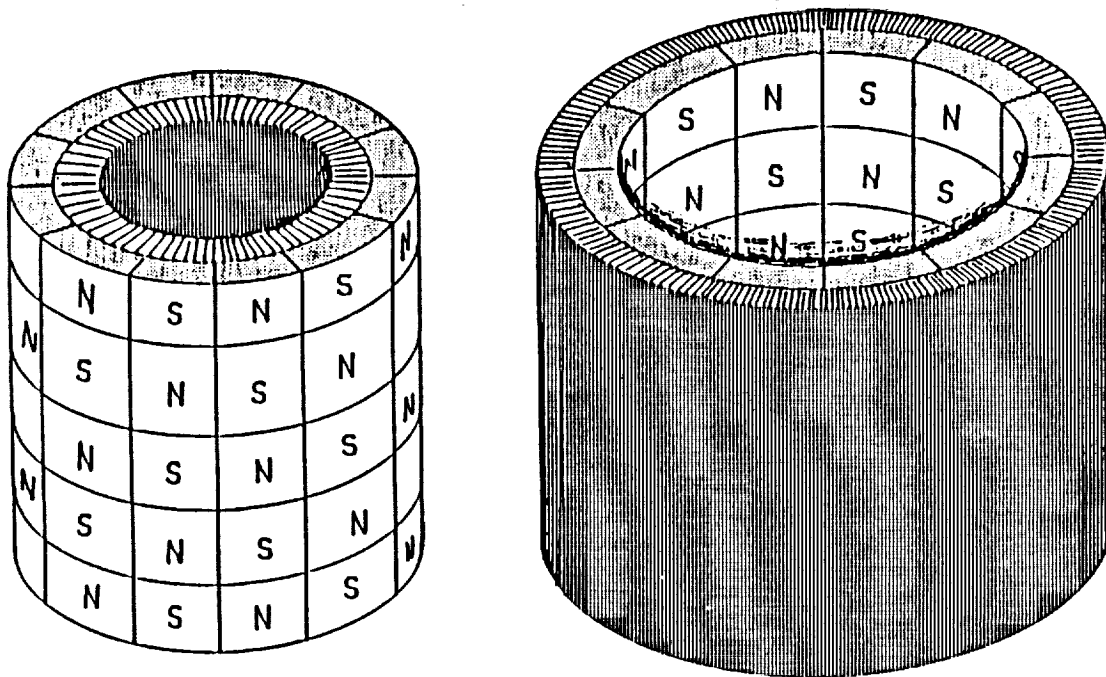
- A single-cylinder FPSE/LA generating 150 kW<sub>e</sub> and meeting program goals is feasible based on this conceptual design study.





89745

Figure 1-5. Multicylinder Free-Piston Stirling Engine Conceptual Design



89735

Figure 1-6. Magnetic Linear-to-Rotary Converter Configuration

- The radial-flow heat exchanger engine concept has better performance and weight characteristics with increasing power level than the modular CSSE-type engine concepts. Each of the three heat exchanger concepts considered allows power module scaling to the 150-kW<sub>e</sub> power level with acceptable specific mass and efficiency.
- Power module efficiency increases with power level from 25 to 150 kW<sub>e</sub>, but specific mass increases as well.
- Relative efficiency (fraction of Carnot efficiency) increases and specific mass decreases with increasing heat exchanger temperature ratio.
- Selection of the "best" power module design point cannot be made without information on the overall system trade-offs between power module mass and efficiency. Power module efficiency can be increased at the expense of increased specific mass.
- Alternator tuning capacitors do not have a major impact on power module specific mass over the power range of the study.
- The dynamic balancer (including both moving mass and structure) increases power module specific mass by 20 to 30% (relative to an unbalanced single-cylinder power module). An adaptive pressure control system is required for the balancer to adjust for changes in balancer dynamic tuning.
- Items that require further attention include fabrication of branched heat pipes, material compatibility with liquid metals, material welding, flow distribution in the heat exchangers, control of the close clearances of bearings and seals (tolerance stackups, thermal distortion), alternator plunger length and stiffness, high-temperature alternator materials, and the hydrodynamic bearing spin motor and coupling designs.
- The alternative configurations considered in this study (multicylinder FPSE/LA, FPSE coupled to rotary alternator) have technical drawbacks that require additional design work. The probability of performance improvements over the single-cylinder FPSE/LA approach is considered low.
- Joining the single-cylinder engines in an in-line, opposed configuration provides a dynamically balanced module without the balancer mass and efficiency penalties. The structure required to join the engines adds approximately 0.2 kg/kW<sub>e</sub> to the basic power module specific mass.
- The radial engine design can be scaled up to 500 kW<sub>e</sub> at a temperature ratio of 2.0, at which point the power module specific mass exceeds 10 kg/kW<sub>e</sub>.

### 1.3 Recommendations

Recommendations for future work related to high-power FPSE/LA power systems are summarized below. Included are key technology areas that require further design or evaluation.

- Perform detailed design and analysis of branched heat pipes. Fabricate and test branched sodium heat pipes at 1050 K.
- Study sodium compatibility with potential heat pipe materials.
- Fabricate and test radial-flow heat exchangers in an engine test rig.
- Perform characterization tests of alternator materials (magnets, laminations, and insulation) at 250 to 300°C operating temperature.
- Perform a detailed design study of a spin motor and coupling.
- Perform a preliminary design of a single-cylinder, 150-kW<sub>e</sub> FPSE/LA.



## 2.0 ENGINE CONCEPT EVALUATION AND SELECTION

The primary objective of this study was to evaluate the feasibility of increasing the power output of a single-cylinder (single piston, single displacer) FPSE/LA from the 25-kW<sub>e</sub> level of current SSE design activity up to 150 kW<sub>e</sub>. This required answers to the following questions:

- How do FPSEs scale with power? What mechanical and/or performance limitations determine the maximum feasible power level?
- How do linear alternators scale?
- How do heat transport systems scale?
- How does the dynamic balancer scale?
- What engine design concept provides good performance, low specific mass, acceptable level of risk, and can be scaled to increased power level in a straightforward manner?

In the course of answering these questions, several concepts were evaluated. The 25-kW<sub>e</sub> CSSE design with modular heat exchangers, shown in Figure 1-4, provided the starting point, but initial work revealed both mechanical and thermodynamic shortcomings in the design. Design modifications led to the separate duct concept and two modular designs: finned heat exchangers (depicted in Figure 1-1) and shell-and-tube heat exchangers (depicted in Figure 1-2). These were followed by a new engine concept with radial-flow heat exchangers (see Figure 1-3), which eliminated the fabrication risks associated with Inco-713 used in the hot end of the modular designs. A detailed discussion of the engine concepts is provided in Section 2.2.

### 2.1 Design Requirements

The design requirements specified in the work statement were as follows:

- Configuration: Single-cylinder FPSE (single piston, single displacer) with linear alternator and tuning capacitors if required
- Power module thermal efficiency (net electrical output power/heat input):  $\geq 20\%$
- Power module specific mass: 5 to 8 kg/kW<sub>e</sub>
- Heater gas-side metal wall temperature: 1050 K
- Cooler gas-side metal wall temperature: 525 K
- Hot-end material: superalloy
- Design life: 7 years (60,000 hr)
- Engine working fluid: helium
- Alternator output voltage:  $\geq 100$  V
- Maximum power module vibration amplitude: 0.0038 cm
- Hot-end heat transport system: heat pipe with sodium working fluid
- Cold-end heat rejection system: pumped loop with NaK working fluid.

### 2.2 Engine Concepts

The selection of an engine concept capable of scaling over a wide range of power levels involves both mechanical and thermodynamic considerations. The principal focus of this study is on displacer-type FPSEs, and all of the concepts considered have a similar displacer drive assembly. The main differences between concepts are in the configurations of the heat exchangers and the pressure vessel.

The annular heat exchanger design used for the Space Power Demonstrator Engine (SPDE) power module is not expected to scale well up to the 150-kW<sub>e</sub> size due to performance and weight penalties with increasing power level. (Figure 2-1 shows the heat-pipe version of the SPDE.) This results from the structural constraint imposed by the regenerator wall (regenerator length must increase with diameter to maintain an acceptable thermal stress level). Annular heat exchangers were not considered for this study.

The modular heat exchanger approach selected for the 25-kW<sub>e</sub> CSSE conceptual design reduces a single, large diameter regenerator to a number of relatively small-diameter regenerators, thereby reducing the thermal stresses in the regenerator wall. Provided that a common heat exchanger module suitable for use in both low and moderate power engines is designed, the job of engine scaling reduces to selecting the correct number of modules and connecting them to the proper size displacer drive and alternator subassembly. Because of this scaling potential and the background of modular heat exchanger use for the CSSE design, the modular design was the initial choice for the scaling study.

### 2.2.1 Modular Heat Exchangers

Evaluation of the CSSE concept for this study indicated the need for further analysis in both the structural and thermodynamic areas. The structural problems occur in the heat exchanger modules and flanges connecting them to the engine vessel. High thermal stresses in the modules result from radial expansion of the hot flange relative to the cold flange during heating at startup. Due to the stiffness of the flanges, the module ends are constrained from rotating, with large resultant bending moments. Analysis showed that for module diameters greater than 25 mm, the stress in the module wall would exceed the material yield strength. To avoid this situation, the continuous flanges were replaced by separate ducts (shown in Figure 1-1), thereby introducing sufficient flexibility to accommodate the differential thermal expansion. The stresses in the ducts and modules are a function of the length and diameter of both the modules and the ducts. For typical component sizes in modular engines of 25 kW<sub>e</sub> and larger, structural constraints on duct dimensions do not penalize the engine thermodynamics.

Both finned and shell-and-tube-type heat exchangers were considered for the heater and cooler in the modular heat exchanger evaluation. The finned heat exchangers, shown in Figure 2-2, are similar to the CSSE conceptual design. The condenser end of the heat pipe has radial fins on the outside surface extending along its length. The engine working fluid flows in the channels formed by the heat pipe fins and an outside cylinder into which the finned heat pipe is inserted and joined. The cooler follows a similar finned channel arrangement, and can use either a heat pipe or a pumped loop. In the pumped loop configuration, the heat pipe would be replaced by an inner pipe assembly for internal coolant flow (see Figure 2-3a), or by a low-density stuffer for external coolant flow (see Figure 2-3b). The internal coolant approach is more compact, and was the approach assumed for performance calculations. The external coolant scheme has the coolant flowing around the outside of the module, adjacent to the cooler. This requires an annular shell around all the modules to provide a flow path for the coolant. More surface area at the cooler-coolant interface is available compared to the internal coolant case. However, with the outside coolant assembly, the outer shell increases the effective maximum diameter of the modules, and the duct lengths must increase to span from the modules to the displacer vessel.

In the shell-and-tube heat exchangers, the finned gas channels are replaced by a number of small circular tubes (shown in Figure 1-2), similar to the heater and cooler of the SPDE. To mate with the sodium heat-pipe heat transport system, the heater tubes are covered with a thin wick layer, which is connected back to the main heat-pipe adiabatic section via a "wick bridge." The sodium vapor flows into the heater shell enclosure, condenses on the heater tubes, and the liquid sodium is wicked back to the main pipe for return to the evaporator. The cooler can be configured for either a pumped loop or heat-pipe heat transport system. For the latter case, the cooler follows the heater design, except that it serves as the heat pipe

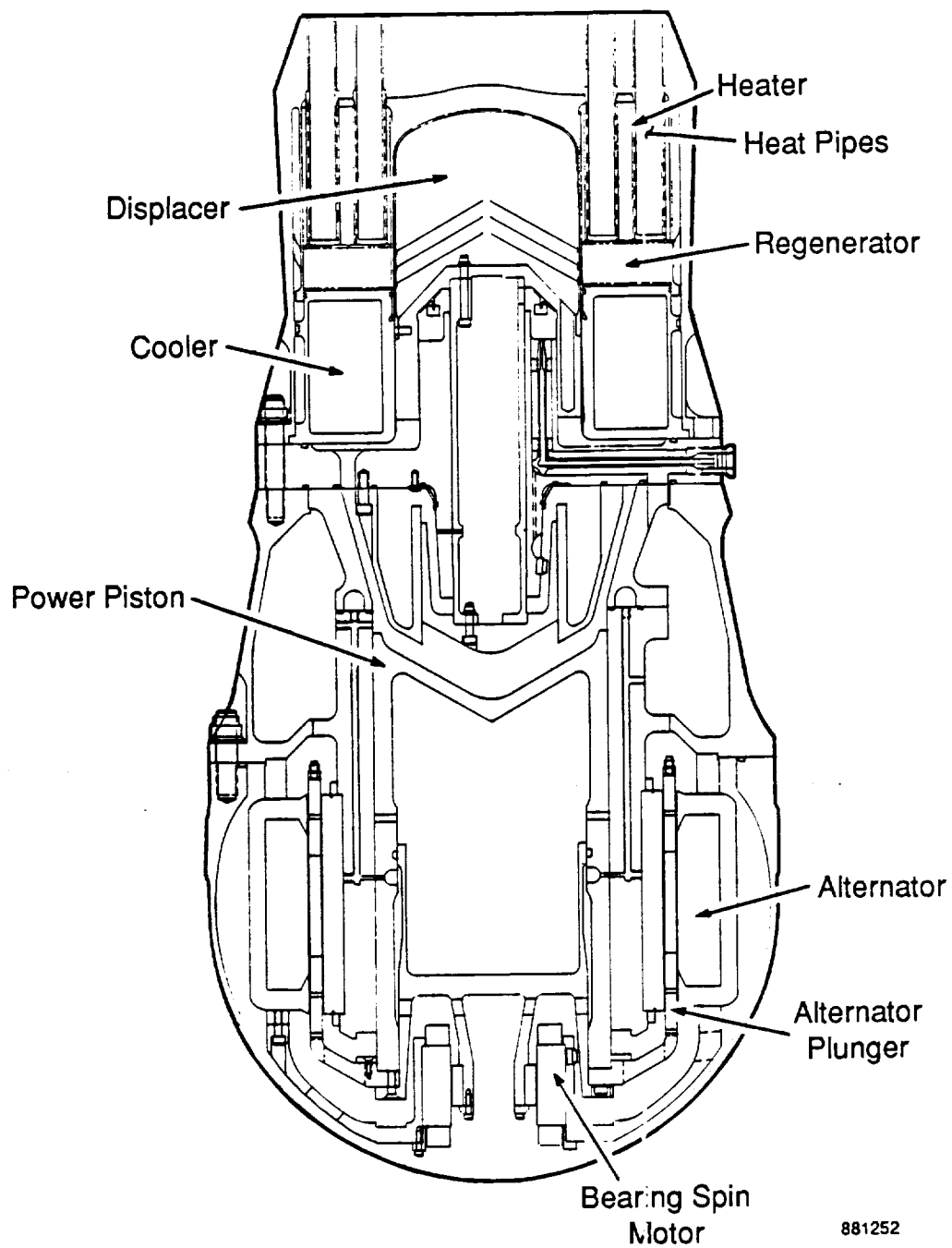
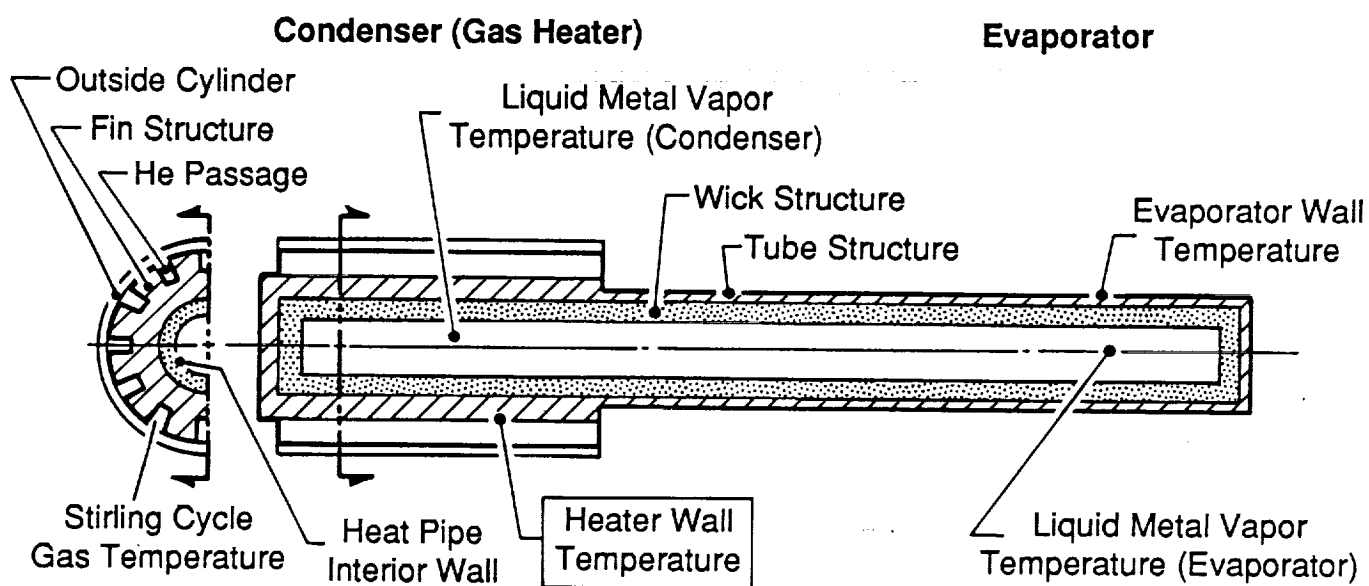


Figure 2-1. Layout of Annular Design



89703

Figure 2-2. Finned Heater Heat-Pipe Schematic



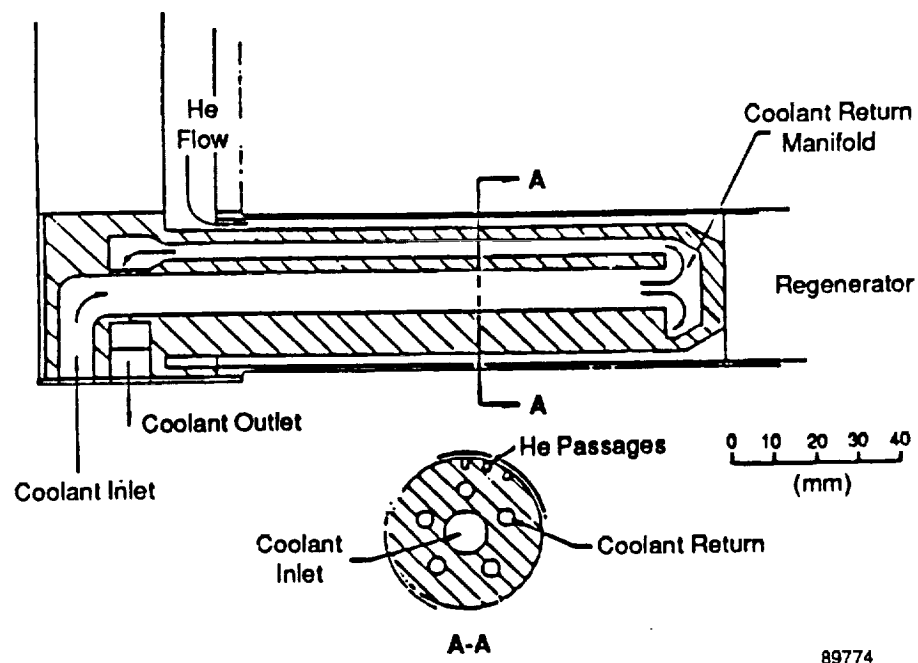


Figure 2-3a. Pumped Loop Cooler Concept - Internal Coolant

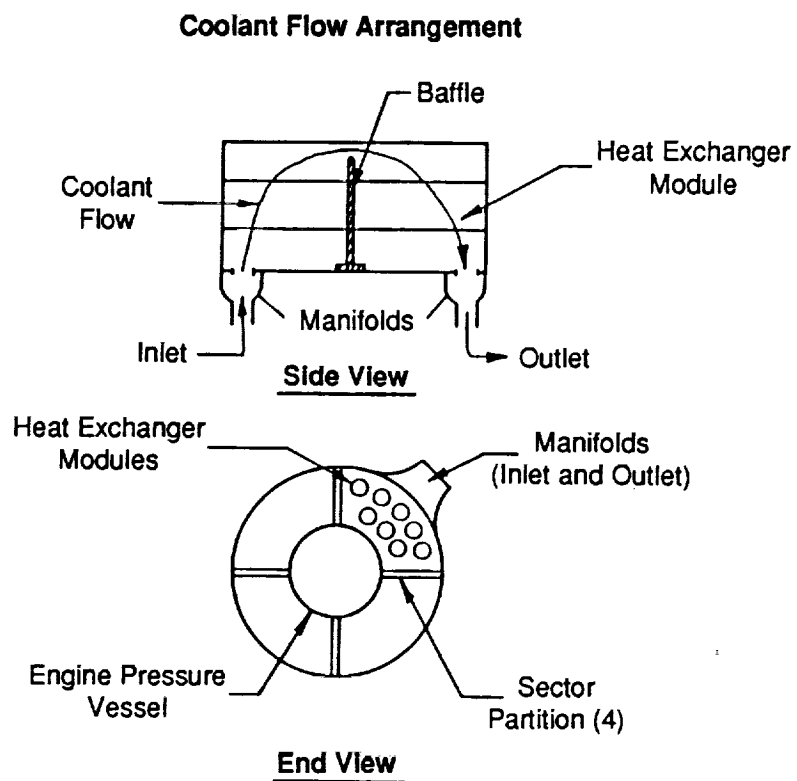
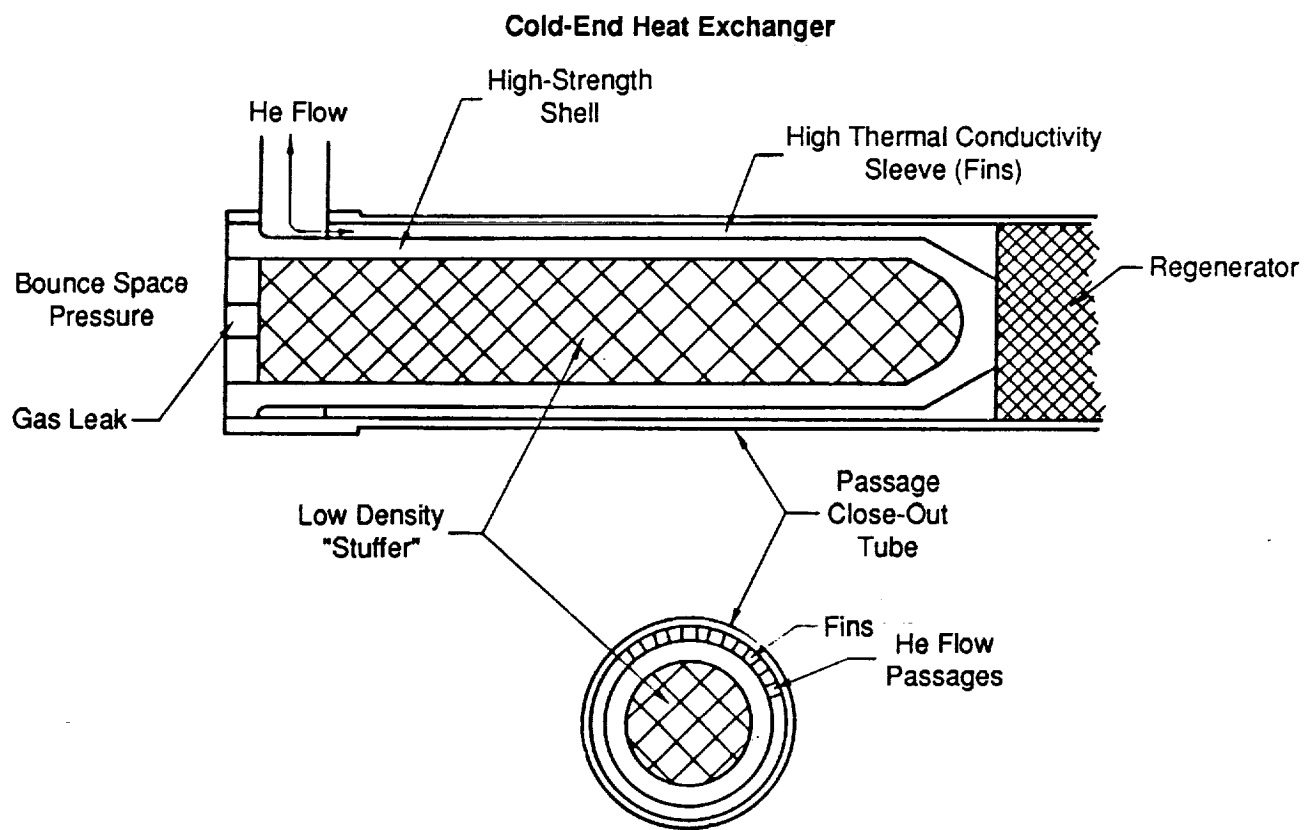


Figure 2-3b. Pumped Loop Cooler Concept - External Coolant

89765

evaporator, rather than condenser. Boiling limits in the heat pipe evaporation may force the cooler to longer-than-optimal length, but this is not expected to eliminate the cooler heat-pipe concept from consideration. For the pumped loop case considered in this study, liquid NaK would flow transverse to the tubes on the shell side.

For both modular configurations, the regenerator is a full cylindrical disk between the heater and cooler assemblies. In order to provide a straight load path in the module outside pressure vessel wall, the heater and cooler outside diameters are approximately equal to the regenerator outside diameter.

Thermodynamic performance of a 25-kW<sub>e</sub> engine using the finned modules of the CSSE design was approximately 30% below requirements, as determined by analysis using MTT's harmonic code. Module optimization and characterization were required to improve performance and to facilitate the scaling of the engine power output from 25 to 150 kW<sub>e</sub>. This allowed selection of the best module size and heat exchanger geometry to meet the design requirements over a range of power levels. The modules were optimized for maximum indicated engine efficiency. For the finned heat exchangers, the channel width, height, and fin thickness were optimized; for the shell-and-tube configuration, the number of heater and cooler tubes and tube inside diameters were optimized. For both cases the heater and cooler lengths were fixed at 60 mm based on previous experience, which shows improved performance with shorter heat exchangers. The 60-mm length was selected as a practical minimum due to heat pipe performance limits and pressure drop limits in the coolant pumped loop. The screen regenerator wire diameter was fixed at 25.4  $\mu\text{m}$ . The regenerator porosity and length-to-diameter ratio (L/D) were optimized for all cases.

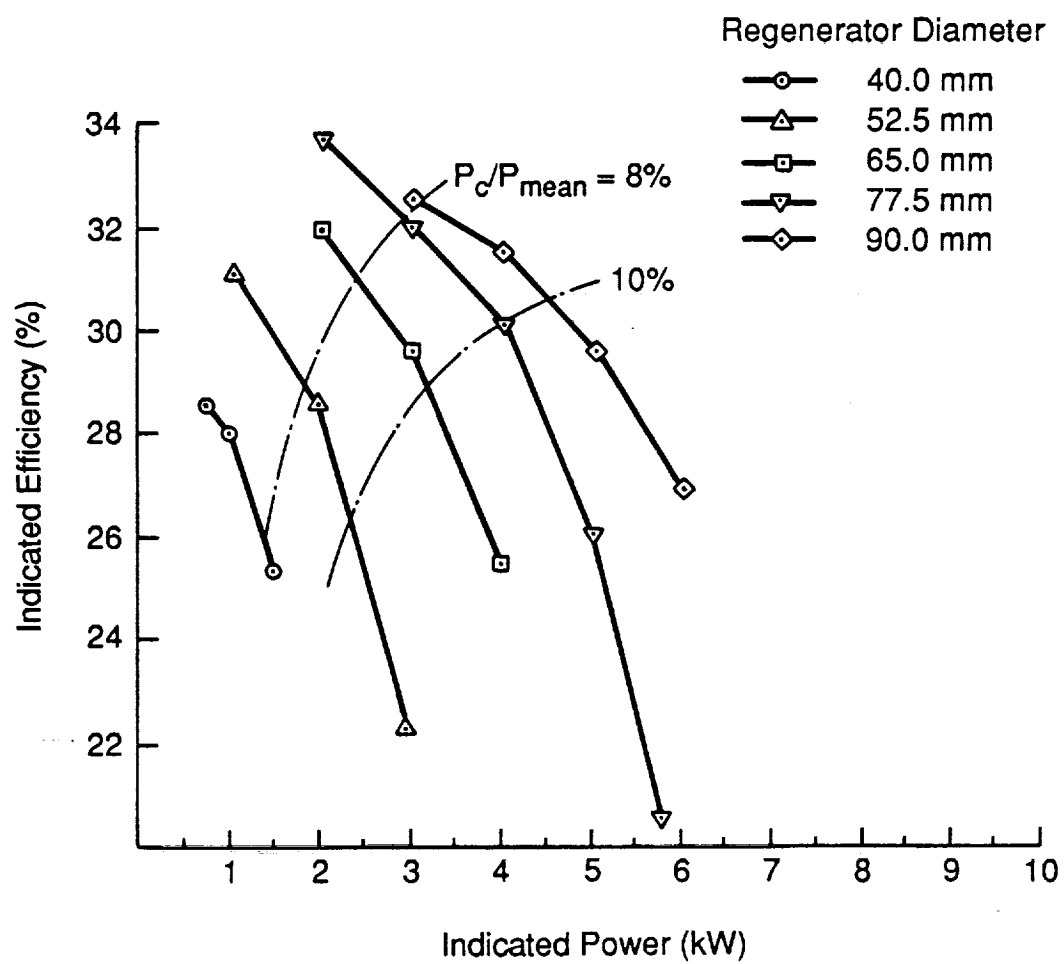
The optimization results, presented in Figures 2-4 through 2-8, led to the selection of 90-mm diameter modules driven at 9% pressure amplitude as the best choice for both module types. As seen in the figures, indicated engine efficiency increases with increasing regenerator diameter, but at the expense of increased module specific mass. For a regenerator diameter greater than 90 mm, there is a diminishing efficiency gain due to an increased pumping loss fraction (pumping loss per net thermodynamic power generated). The pumping loss increases because of the increasing regenerator length (due to the structural constraint of regenerator wall L/D ratio). Figures 2-4 through 2-6 show the indicated engine efficiency, specific mass, and heat-pipe wall temperature drop for the finned heat exchanger module as a function of power level and module diameter. Figures 2-7 and 2-8 show similar results for the shell-and-tube module (tube wall  $\Delta T$  is very low and is not shown). In selecting the best module size for each configuration, the trade between module power level and efficiency as a function of pressure amplitude was evaluated. In view of the design goal of 150 kW<sub>e</sub> per engine, the higher power modules are preferred since the manifolding and packaging of fewer modules is easier.

The indicated power of the 90-mm diameter finned module is 3.8 kW, compared to 5 kW for the shell-and-tube configuration module. Therefore, the finned module engine requires one third more modules than the shell-and-tube module engine for the same engine power output. A single shell-and-tube module has about the same mass as a single finned module.

Performance details of the modular configurations are provided in Section 2.4.

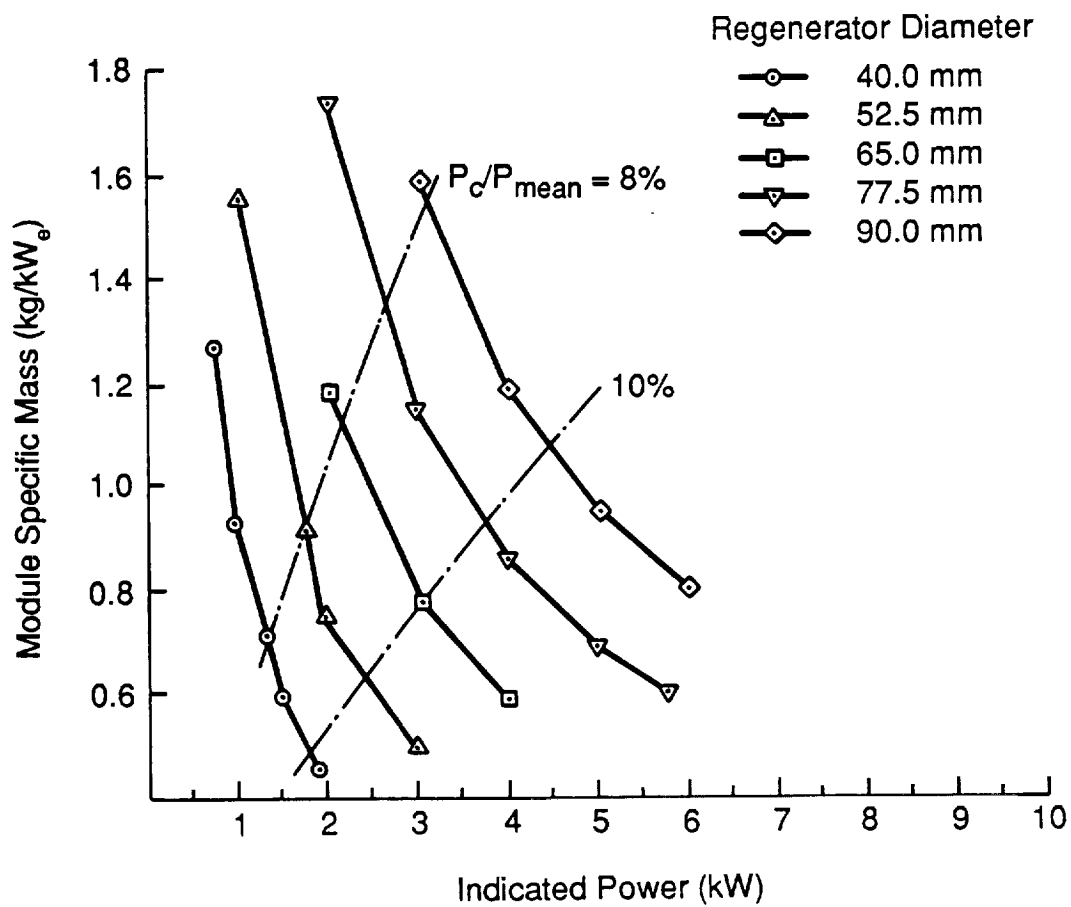
### 2.2.2 Radial-Flow Heat Exchangers

The modular engine designs described above require a very high-strength, high-temperature superalloy such as Inco-713 for the hot pressure vessel in order to achieve acceptable engine specific mass. The hot pressure vessel includes the displacer pressure vessel, the module vessels, and the hot connecting ducts. The welding of Inco-713 has not been demonstrated for components of these shapes and poses a design risk.



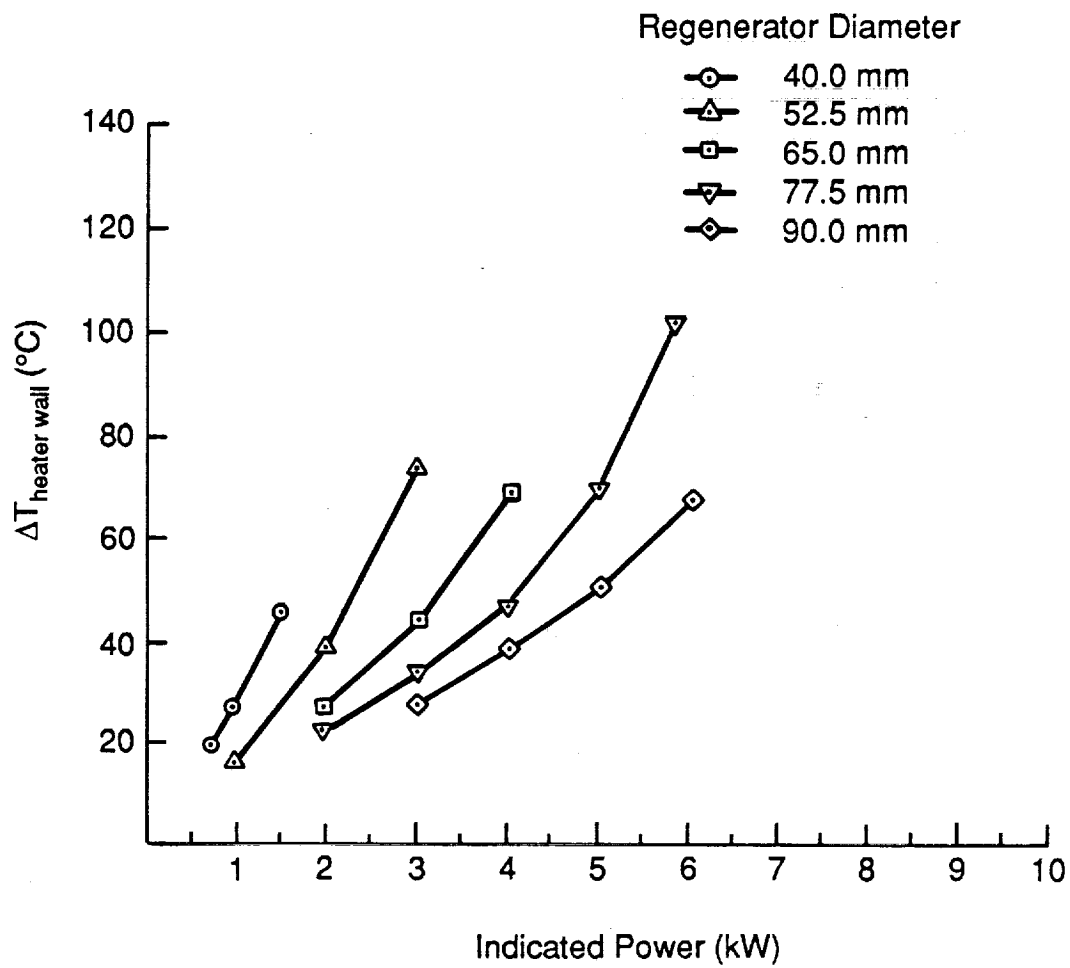
89705

Figure 2-4. Finned Module Performance versus Module Diameter and Power



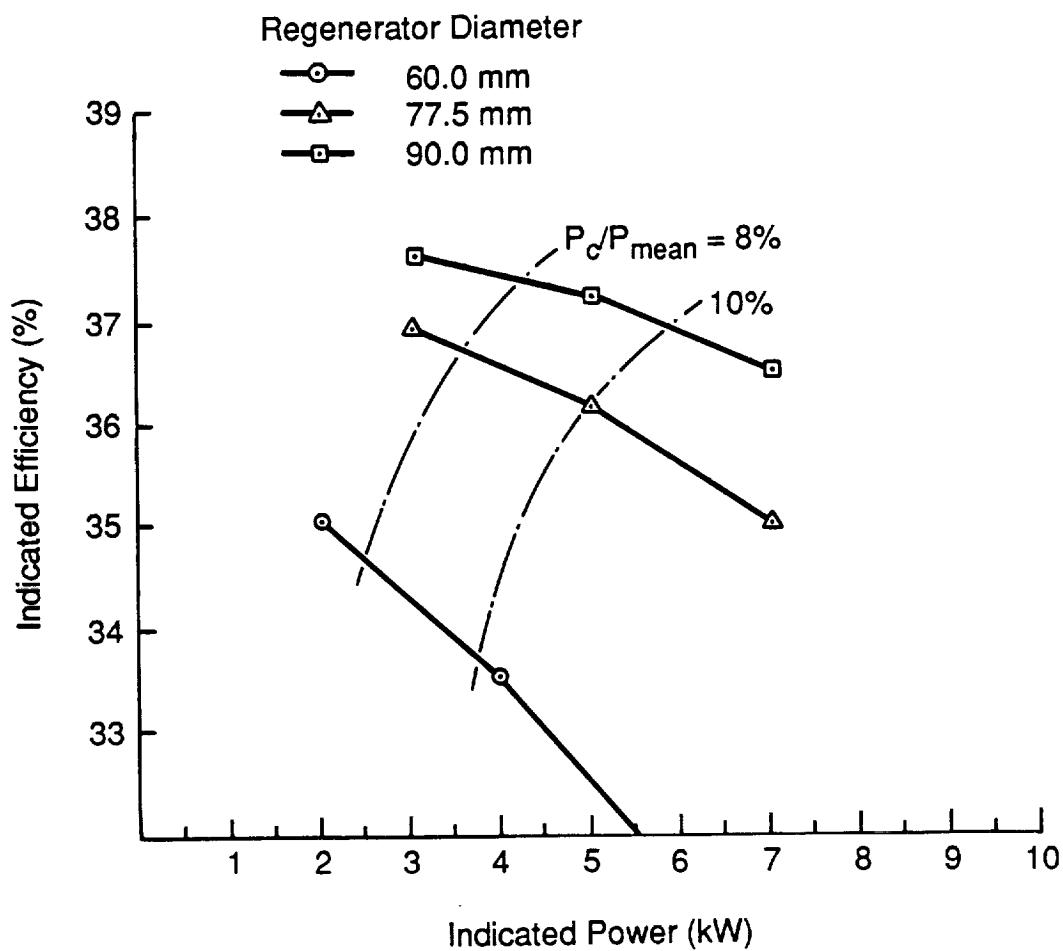
89706

Figure 2-5. Finned Module Specific Mass versus Module Diameter and Power Level



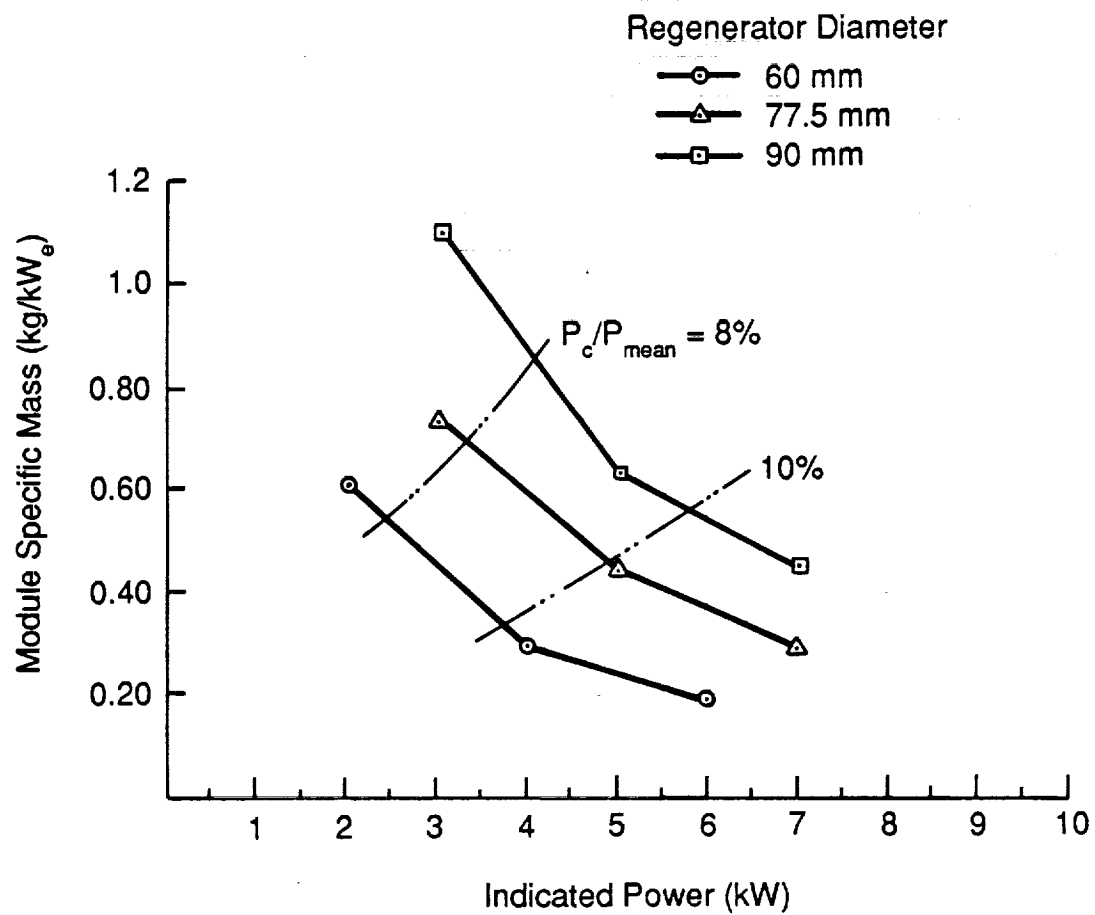
89707

Figure 2-6. Finned Module Heater Wall Temperature Drop versus Module Diameter and Power Level



89708

Figure 2-7. Shell-and Tube Module Performance versus Module Diameter and Power Level



89749

Figure 2-8. Shell-and-Tube Module Specific Mass versus Module Diameter and Power Level



To avoid the use of Inco-713, the radial-flow engine (shown in Figure 1-3) was designed with a relatively small section of pressure vessel operating at the full heater temperature. By restricting the heater heat pipes to a small diameter at the penetration through the pressure vessel, the mass of the hot pressure vessel does not dominate the overall engine specific mass. Lower strength superalloys such as Inco-625, which has good weldability, can then be used.

The primary difference between the configurations of the modular and radial engines is the arrangement and location of the heat exchangers. The modular heat exchangers are located outside of the displacer pressure vessel, and the gas flows parallel with the displacer axis. The radial engine heat exchangers are positioned within the pressure vessel, close to the expansion space, with the working fluid flowing radially with respect to the displacer. By locating the heat exchangers within the main pressure vessel, the heat exchanger walls are loaded only by the alternating pressure of the engine cycle, instead of the full engine pressure (mean plus alternating), which the modular walls see. This design feature results in significant mass reduction for the radial engine.

Details of the radial engine heat exchanger construction are shown in Figure 2-9. In the heater and cooler, the gas flows in rectangular passages formed by an assembly of thin metal plates. Full annular plates are alternately stacked with smaller plate sections that are evenly spaced, circumferentially, to form the gas channels. Continuous end plates are used to enclose the heater, regenerator, and cooler, and form a boundary between the working spaces and the surrounding mean pressure regions. The regenerator wall incorporates a bellows type of construction to reduce thermal stresses. All of the heat exchanger plates are punched with holes to accept the heat pipes and coolant pipes, and the assembly is furnace-brazed to seal the spaces between plates and provide a good thermal connection between plates and pipes.

As shown in Figure 2-9, the heat pipes are arranged in groups of three, although this can vary depending on whether the design criteria is for maximum efficiency or minimum specific mass (see Section 4.0). The regenerator in the radial engine is an annulus with the same axial length as both the heater and cooler. This provides an easy means of increasing the heat exchanger frontal area by increasing the heat exchanger axial dimension. Further details of the radial engine heat exchangers are provided in Section 3.3.

## 2.3 Scaling Considerations

As mentioned in the introduction, power module scaling from 25 to 150 kW<sub>e</sub> requires consideration of how each of the power module subassemblies scale. This includes structural, thermodynamic, dynamic, and electromagnetic aspects of the system.

### 2.3.1 Structural Aspects

For the modular heat exchanger engines, the assembly of modules into a full engine requires consideration of module spacing and ducting. Since displacer diameter varies with the square root of engine power, and engine power increases in direct proportion to the number of modules, the displacer perimeter available per module varies inversely with the square root of power. For a 25-kW<sub>e</sub> engine, 8 of the finned modules, or 6 of the shell-and-tube modules, are required. Assuming a 160-mm diameter displacer, there are 63 mm of perimeter per module for the finned module, and 84 mm per module for the shell-and-tube module. These perimeters allow sufficient space to easily accommodate ducts, both structurally and thermodynamically. However, when scaled to 150 kW<sub>e</sub>, the available perimeter for the finned module drops by  $1/\sqrt{6}$  to 26 mm, which is insufficient to allow adequate duct size with good remaining structural material between ducts. The same is true with the shell-and-tube module, which has just 34 mm of available circumference per module.

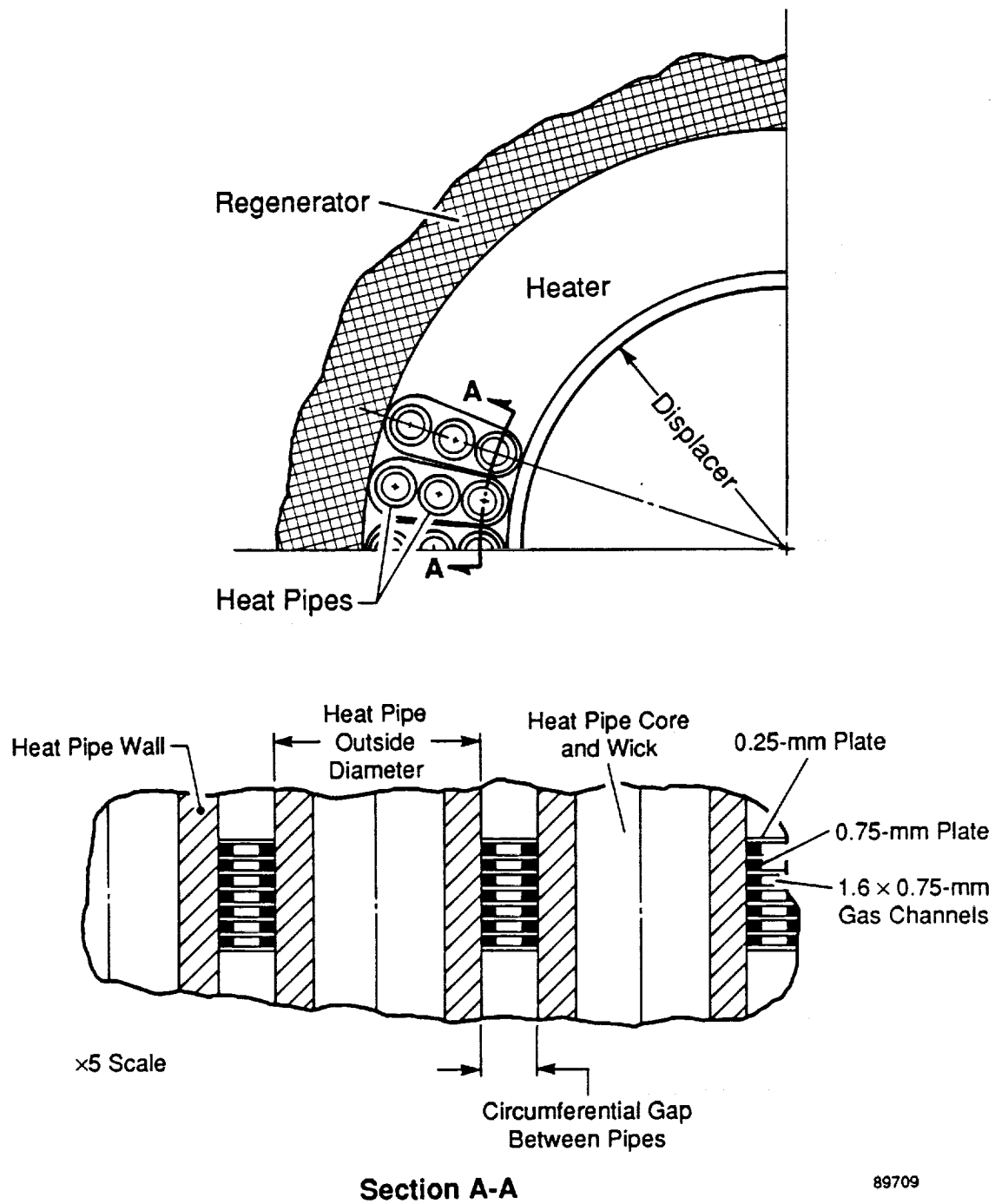


Figure 2-9. Radial Engine Heat Exchanger Detail

A solution to this problem is to gang the modules together in groups of two to four, with single ducts connecting each group to the working spaces (see Figure 1-1). Sufficient displacer perimeter is then available per duct, even though the duct diameter increases. Depending on the size and number of groups, they can be arranged on a single circle or staggered into an inner and outer circle.

Scaling of the radial heat exchanger engine requires that the heater heat-pipe penetrations through the pressure vessel be maintained on a sufficiently small diameter to keep the mass of the hot structure acceptably small.

### **2.3.2 Thermodynamic Aspects**

Since the geometry of the modular engine heat exchangers is not varied with power level (only the number of modules is varied), the modular heat exchanger thermodynamics do not change with power level for constant volume amplitudes at the module faces. However, there is a thermodynamic penalty with larger power levels due to the increased duct volume required to connect the modules to the engine pressure vessel.

For the radial engine, the heat exchangers are scaled to achieve the optimization objectives at a given power level, and there are no fundamental heat exchanger scaling penalties.

As detailed in Section 2.4.1, seal clearances increase with increased engine size. Since, for constant stroke, the engine power varies with piston diameter squared, and piston seal leakage loss varies with piston seal clearance cubed, the leakage loss increases proportional with [engine power]<sup>3/2</sup> (for constant seal L/D). Thus, seal leakage has a tendency to limit the engine pressure amplitude at higher power levels to avoid major performance penalties.

### **2.3.3 Heat Pipes**

Heat pipe performance limits, as discussed in Section 4.2, set the heat-pipe diameter and length. For increased power level, the number of heat pipes scale directly, therefore heat-pipe specific mass is constant.

### **2.3.4 Alternator**

From first-order alternator analysis, magnet mass increases linearly proportional with power. Coil area is independent of power, depending only on efficiency. Based on these trends, alternator specific mass decreases slightly with increasing power level (magnet specific mass is constant, copper and iron specific masses decrease).

### **2.3.5 Dynamic Balancer**

Dynamic balancer size is set by the engine unbalanced force, which is due primarily to the power piston and alternator plunger. To the first-order, for constant power piston and alternator plunger (magnet) specific mass, the balance specific mass is constant. Actual required balance mass depends on balancer losses, as discussed in Section 4.2.4.

## **2.4 Concept Comparisons**

Following preliminary performance analyses of the finned module engine, shell-and-tube module engine, and radial engine, a detailed comparison of the geometry, performance, and specific mass breakdowns of

the configurations at the 25- and 150-kW<sub>e</sub> power levels was made and presented to NASA-LeRC. Tables 2-1 through 2-3 summarize the results. Note that the radial engine geometries given in Table 2-1 are from the preliminary analysis performed at that stage of the program. The optimized radial engine designs developed later in the program do not exactly match these early designs.

All numbers were based on conceptual designs without detailed engine performance optimization, allowing general comparisons to be made based on basic design features. All three engine concepts were evaluated with identical displacer and piston diameters (160-mm diameter at 25 kW; 392-mm diameter at 150 kW), with a displacer-to-piston stroke ratio of 0.7. No attempt was made at the time to select the optimum combination of piston area and stroke.

For comparison purposes, the concepts were evaluated at the same indicated power levels (30 and 180 kW<sub>i</sub>). Since the calculated mechanical efficiencies of the engines varied slightly, the listed electrical powers do not exactly match the 25- or 150-kW<sub>e</sub> goals. The efficiency and specific mass values in Tables 2-2 and 2-3 do not include the effects of the dynamic balancer assembly.

A discussion of the information presented in the tables is given below. The comparison of engine geometries is covered first, followed by thermodynamic and mechanical efficiencies, engine losses, thermal characteristics, and specific masses.

#### 2.4.1 Engine Geometry

The comparisons of the geometries of the three designs are concentrated on those areas where significant differences occur, primarily in the heat exchangers. Since all of the engine concepts have a similar displacer assembly and alternator assembly, these areas are not compared. The displacer and power piston seal clearances are set to 12.7- $\mu$ m radial clearance for piston diameters up to 152 mm, and increase linearly with diameter for sizes greater than 152 mm. Thus, for the 392-mm piston diameters used for the 150-kW<sub>e</sub> engines, the seal clearance is  $(392/152 \times 12.7 = 32.8 \mu\text{m})$ . For concentric seals, as in the displacer drive, the outer seal clearance is increased by 30% to allow for tolerance stackups.

**2.4.1.1 Heat Exchangers.** Since the radial engine heat exchanger geometry is not strongly coupled to the engine structural requirements, large frontal areas for all heat exchangers (heater, cooler, and regenerator) are possible without excessive structural weight penalty. The heat exchanger surface areas are also high, and relatively short heat exchangers (in the direction of flow) can be used. As shown in Table 2-1, for a given power output the frontal and surface areas of the radial engine heat exchangers exceed those of both the modular engines.

The shell-and-tube module has less actual heat exchanger surface area than the finned module, but lower heater fin effectiveness gives the finned module the lowest effective heater surface area. In the cooler, the finned module uses copper fins and the effective surface area exceeds that of the shell-and-tube module.

**2.4.1.2 Manifold/Ducts.** The radial engine has no hot ducts\*, and its long cold duct has a similar volume to the manifold volumes in the modular engines. The finned module engine has more manifold volume than the shell-and-tube module engine because of the greater number of modules used. When scaled up to 150 kW<sub>e</sub>, the finned module manifolds become longer than the shell-and-tube's because of the greater circle diameter needed for 48 modules, compared to 36 modules.

---

\*The expansion space is connected to the heater via formed sheet metal which, depending on the location of the heat exchangers relative to the displacer, can add significant hot volume.

Table 2-1. Preliminary Engine Geometric Parameters - Used in Concept Selection

Engine Configuration	Radial		Finned Modules		Tube/Shell Modules	
Engine Size (kW <sub>e</sub> )	25.0	150.0	25.0	150.0	25.0	150.0
Engine Temperature Ratio (-)	2	2	2	2	2	2
Engine Mean Pressure (MPa)	15.0	15.0	15.0	15.0	15.0	15.0
Operating Frequency (Hz)	90.0	90.0	90.0	90.0	90.0	90.0
Number of Modules	--	--	8	48	6	36
Displacer Diameter (mm)	160.0	392.0	160.0	392.0	160.0	392.0
Piston Diameter (mm)	160.0	392.0	160.0	392.0	160.0	392.0
Displacer Amplitude (mm)	8.4	9.1	9.4	9.9	8.3	8.8
Piston Amplitude (mm)	12.1	13.0	13.5	14.2	11.9	12.6
Displacer/Piston Phase (°)	65.0	65.0	65.0	65.0	65.0	65.0
Regenerator						
Frontal Area (cm <sup>2</sup> )	590.0	3350.0	509.0	3054.0	382.0	2290.0
Wire Diameter (μm)	25.4	25.4	25.4	25.4	25.4	25.4
Porosity (%)	80.0	80.0	79.0	79.0	79.0	79.0
Length (mm)	26.0	26.0	36.0	36.0	37.8	37.8
Heater						
Hydraulic Diameter (mm)	1.02	1.02	0.80	0.80	1.25	1.25
Number of Passages (-)	2,700	18,000	2,144	12,864	1,488	8,928
Frontal Area (cm <sup>2</sup> )	32.4	216.0	19.4	116.7	18.3	109.8
Surface Area (m <sup>2</sup> )	0.711	4.740	0.587	3.524	0.351	2.104
Effectiveness (%)	85.0	85.0	45.0	44.0	100.0	100.0
Effective Surface Area (m <sup>2</sup> )	0.604	4.030	0.264	1.551	0.351	2.104
Length (mm)	56.0	56.0	60.0	60.0	60.0	60.0
Cooler						
Hydraulic Diameter (mm)	1.10	1.10	0.78	0.78	1.00	1.00
Number of Passages (-)	3,645	24,300	2,168	13,008	2,544	15,264
Frontal Area (cm <sup>2</sup> )	54.7	264.5	18.5	111.2	19.9	119.4
Surface Area (m <sup>2</sup> )	0.722	4.811	0.573	3.440	0.480	2.827
Effectiveness (%)	91.0	91.0	89.0	88.0	100.0	100.0
Effective Surface Area (m <sup>2</sup> )	0.657	4.378	0.510	3.028	0.480	2.827
Length (mm)	36.0	36.0	60.0	60.0	60.0	60.0
Manifolds/Ducts						
Hot Volume (cm <sup>3</sup> )	0.0	0.0	607.0	4,655.0	493.0	3,821.0
Cold Volume (cm <sup>3</sup> )	967.0	9,040.0	1,211.0	8,758.0	868.0	6,693.0

Table 2-2. Preliminary Engine Performance Predictions - Used in Concept Selection

Engine Configuration	Radial		Finned Modules		Tube/Shell Modules	
Indicated Power (kW)	30.0	180.0	30.0	180.0	30.0	180.0
Electrical Power (kW)	25.4	147.9	24.9	143.2	25.4	147.9
Indicated Efficiency (%)	34.0	34.0	33.0	32.0	36.0	34.0
Displacer Mechanical Efficiency (%)	95.0	94.0	95.0	94.0	95.0	94.0
Piston Mechanical Efficiency (%)	97.0	95.0	95.0	92.0	97.0	95.0
Alternator Efficiency (%)	92.0	92.0	92.0	92.0	92.0	92.0
Power Module Efficiency (Including Linear Alternator) (%)	29.0	28.0	27.0	25.0	31.0	28.0
Engine Pressure Swing $P_{\text{amplitude}}/P_{\text{mean}}$ (%)	9.1	8.7	8.6	8.5	9.1	8.8
Heater						
Heat Flux Per Channel (W)	27.0	25.0	42.0	43.0	57.0	59.0
$\Delta T_{\text{gas-wall}}$ (°C)	25.0	23.0	39.0	39.0	31.0	31.0
$\Delta T_{\text{wall}}$ (°C)	52.0	52.0	33.0	34.0	5.0	5.0
Cooler						
Heat Flux Per Channel (W)	12.0	11.0	28.0	28.0	23.0	23.0
$\Delta T_{\text{gas-wall}}$ (°C)	16.0	15.0	10.0	10.0	12.0	12.0
$\Delta T_{\text{wall}}$ (°C)	17.0	17.0	59.0	60.0	2.0	3.0
$(T_H/T_C)_{\text{regenerator}}$ (-)	1.76	1.75	1.84	1.84	1.84	1.84

Note: Performance predictions are based on unoptimized conceptual designs. Efficiencies for new engines have an uncertainty of 15%.

Table 2-3. Preliminary Specific Mass Summary - Used in Concept Selection

Engine Configuration Engine Size (kW <sub>e</sub> )	Radial		Finned Modules		Tube/Shell Modules	
	25	150	25	150	25	150
Specific Mass (kg/kW <sub>e</sub> )						
Component						
Heater	0.76	0.79	0.60	0.60	0.39	0.39
Regenerator	0.15	0.11	0.21	0.21	0.16	0.16
Cooler	0.31	0.25	0.35	0.35	0.34	0.34
Manifolds	--*	--*	0.15	0.19	0.13	0.15
Displacer Pressure Vessel	1.20	1.00	0.72	1.11	0.72	1.11
Cold Pressure Vessel	0.99	0.85	0.62	0.68	0.62	0.68
Displacer Assembly	0.36	0.56	0.36	0.56	0.36	0.56
Piston Assembly	0.37	0.55	0.37	0.55	0.37	0.55
Alternator Assembly	1.47	1.34	1.47	1.34	1.47	1.34
Miscellaneous Structure	0.50	0.50	0.50	0.50	0.50	0.50
Total Specific Mass	6.11	5.95	5.35	6.09	5.06	5.78

\*The manifold between the cooler and compression space in the radial engine is integral with the internal engine structure and is included with the displacer assembly mass.

Note: Component masses are calculated from conceptual designs. Specific masses have an uncertainty of 20%.

**2.4.1.3 Engine Dead Volume.** The radial engine and shell-and-tube module engine have similar dead volumes. The finned module engine has more dead volume, due to the greater number of modules and ducts. Increased engine dead volume requires a larger engine displacement to produce the same engine power.

## **2.4.2 Performance**

**2.4.2.1 Indicated Engine Efficiency.** The radial and modular engines have similar indicated efficiencies. At the 25-kW<sub>e</sub> engine size, the shell-and-tube module engine holds a two-point efficiency advantage over the radial engine (due primarily to a higher regenerator temperature ratio), and a three-point advantage over the finned module engine (due to lower pumping and hysteresis losses).

The indicated efficiency of the modular engines decreases with increased engine size due to percentage increases in both pumping and leakage losses. The radial engine indicated efficiency remains nearly constant with increased size because the small pumping loss percentage increase is offset by a decrease in the wall conduction losses as a fraction of engine heat input.

**2.4.2.2 Mechanical Efficiency.** The displacer and piston mechanical efficiencies represent the gas spring (hysteresis and seal leakage) and porting losses. The finned module engine has lower mechanical efficiency due to its higher engine displacement. Increased engine displacement results in higher gas spring and/or leakage losses and reduced mechanical efficiency.

When the engines are scaled to larger sizes, the gas spring seal clearances increase proportional with piston diameter, as discussed above, and the gas spring losses increase.

**2.4.2.3 Engine Losses.** The pumping loss is much lower in the radial engine than in the engines with modules due to the large heat exchanger flow areas in the radial engine. The pumping loss as a fraction of engine power increases slightly with increased engine size because of increases in engine dead volume. This dead volume must be overcome with increased displacement, thereby increasing the heat exchanger mass flow rate per power generated.

The compression space seal leakage is similar for all the engine configurations, showing a large increase between the 25- and 150-kW<sub>e</sub> engines because of the increased seal clearances.

The conduction losses in the radial engine regenerator matrix are higher than in the modular engines because of the increased regenerator frontal area and shorter regenerator length. However, the regenerator wall in the radial design carries the pressure amplitude only, and wall thickness does not increase with engine size as in the modular engines. Therefore, wall conduction is much less in the radial engine, particularly at high power levels.

**2.4.2.4 Wall Temperature Drop.** Temperature drops through the heat exchanger walls are lowest in the shell-and-tube engine because of the relatively thin walls of the tubes, but are not prohibitively high for any of the designs.

For this initial concept comparison, Inco-625 was assumed for the pressure structure surrounding the heat pipes in the radial engine. The 52°C wall drop for the radial heater includes 10°C through the nickel block between the heat pipe and gas channel.

The cooler in the finned module consists of an Inco-718 inner pressure wall with a finned copper sleeve around it. The outer module wall is continued down from the regenerator. The coolant pipe or heat pipe



is assumed to be on the inside of the inner wall. The relatively large temperature drop through the wall is due to its poor thermal conductivity and low surface area.

**2.4.2.5 Gas-Wall  $\Delta T$ .** In the heater, the finned module has the largest film temperature drop because of the small effective surface area. In the cooler, copper fins were assumed for the finned module engines, and aluminum fins were assumed for the radial engine, resulting in high surface effectiveness for both. Despite the fact that the radial engine has the largest effective cooler surface area, it has the largest  $\Delta T_{\text{gas-wall}}$  because of a low heat transfer coefficient (large frontal area results in low flow velocity and reduced heat transfer coefficient).

### 2.4.3 Specific Mass

The three engine configurations have similar total specific mass, as shown in Table 2-3\*. The radial engine heater is heavier than the modular engine heaters because of the large heat exchanger volume.

The displacer pressure vessel mass for the radial engine includes the cylinder around the displacer, the structure that forms the duct between the cooler and displacer flange, and the outer pressure vessel from the bottom of the cooler to the hot end. For the modular engines, the displacer pressure vessel mass includes the main pressure vessel around the displacer and the displacer flange. The radial engine uses Inco-625 for the hot section of the head, and therefore pays a mass penalty compared to the modular engines, which use the stronger Inco-713 for the hot structure. However, the risks of joining Inco-713 are avoided.

The radial engine specific mass as calculated for the concept selection decreases with engine size. This occurs mainly because the hot portion of the displacer pressure vessel does not scale up proportionally with the engine since it is restricted to a relatively small portion of the vessel. The more detailed radial engine designs performed later in the parametric study portion of the program show a slight increase in power module specific mass with power level.

The modular engine's specific mass increases with engine size because of the increase in pressure vessel specific mass.

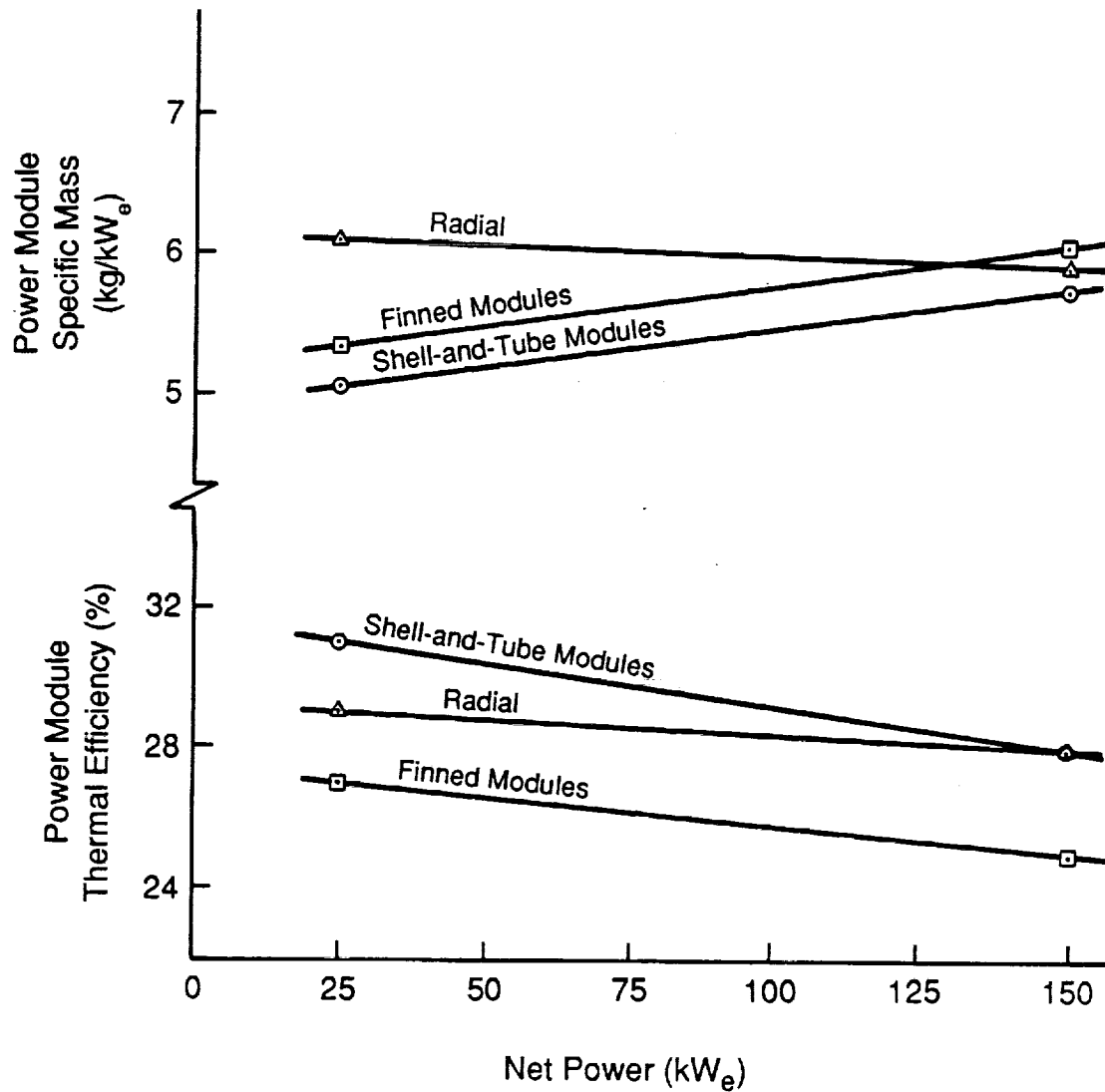
The shell-and-tube module heat exchangers have a lower specific mass than the finned module heat exchangers because more power is generated per shell-and-tube module. Thus, fewer shell-and-tube modules are necessary.

### 2.4.4 Scalability

The change in power module efficiency and specific mass (excluding balancer) with power level for the three concepts is shown in Figure 2-10. The radial engine shows good relationships of performance and specific mass with increasing power output. The modular engines both show decreasing efficiency and increasing specific mass at higher power levels. Based on these preliminary scaled predictions, all three concepts can achieve the design requirements at 150-kW<sub>e</sub> power output. The radial engine is most attractive for higher power requirements because of its excellent and nearly constant efficiency and specific mass.

---

\*Table 2-3 specific mass totals do not include the balancer assembly mass.



89710

Figure 2-10. Power Module Efficiency and Specific Mass\* versus Net Power

\*Does not include balancer assembly specific mass.

## 2.4.5 Risk

All of the engine concepts introduce risk because of the departure from past FPSE designs. This study is directed to incorporate technology expected to be available in the early 1990s. Particular risks associated with specific design features are listed below.

**2.4.5.1 Materials and Joining.** The modular engines use Inco-713 for the hot sections of the engine (displacer pressure vessel, hot duct, heater, and regenerator wall) in order to achieve acceptable specific mass. The welding of Inco-713 is considered very difficult and has not been demonstrated on similar hardware. This is considered a design risk, pending successful demonstration of the welding technique.

On the radial engine, the Inco-713 material risk on the pressure vessel is avoided by using Inco-625 and Inco-718, but there are risks associated with the heat pipe material (HS-31), which does not weld well.

Finally, an all-welded version of the shell-and-tube module would have to be demonstrated. It is felt that you cannot braze the many small tubes and have these joints remain leakproof in a 1050 K liquid sodium environment for seven-year lifetimes.

**2.4.5.2 Heat Pipes.** The use of externally wicked tubes for the shell-and-tube module heater requires a development program before committing to a design. Although Thermacore\* believes such a heat pipe is feasible, it must be considered a risk.

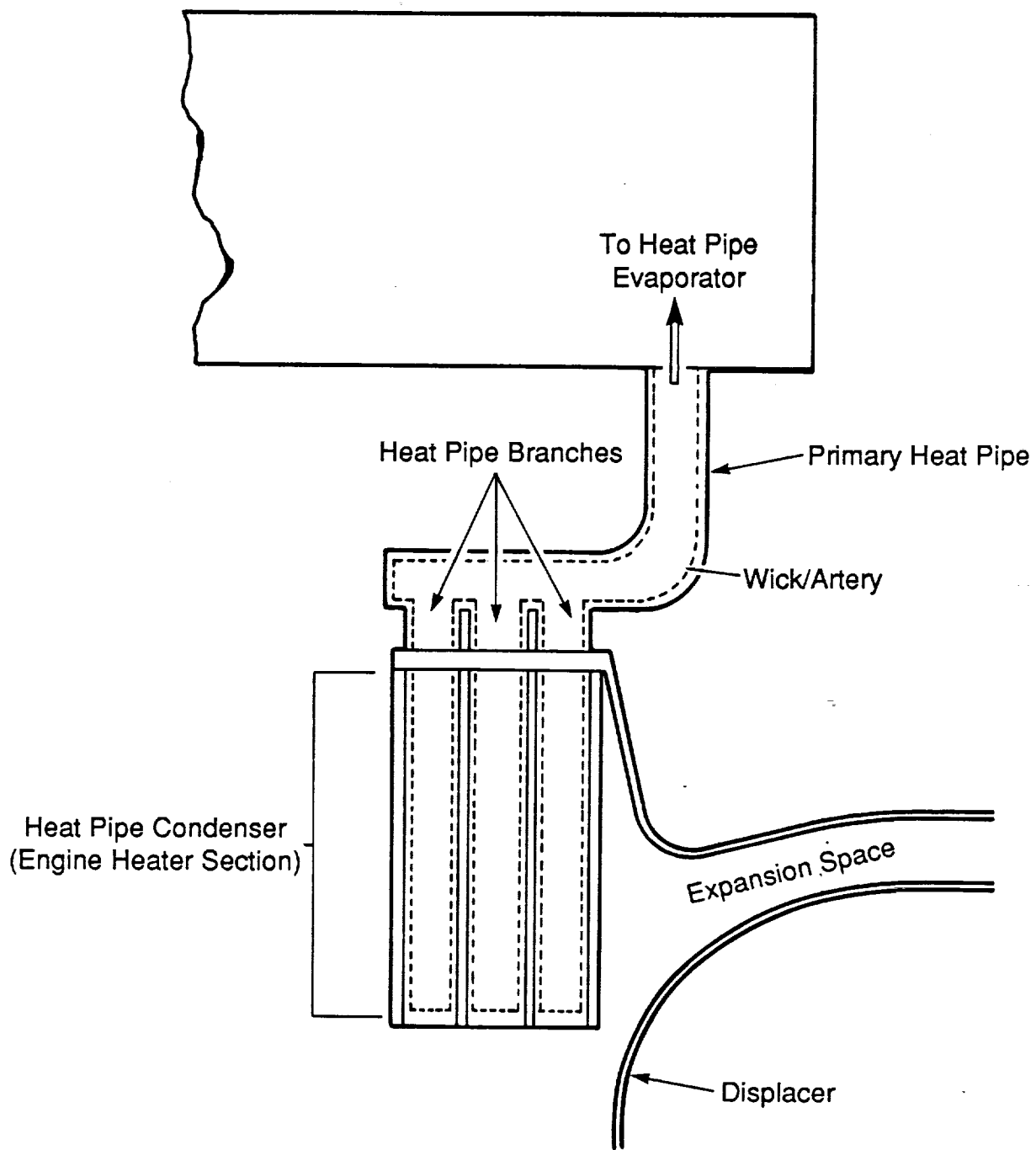
The radial engine uses a branched heat pipe in the heater (see Figure 2-11). Branched heat pipes for this application will require development. Liquid metal compatibility with each of these three concepts must also be addressed.

## 2.5 Concept Selection

Based on the comparison of the finned module engine, the shell-and-tube module engine, and the radial engine, the best overall characteristics over a range of powers are achieved with the radial engine design. It provides the best compromise between good performance and moderate complexity, and offers the most flexibility in scaling. It also offers the possibility of achieving power levels in excess of 150 kW<sub>e</sub> at acceptable values of specific mass and efficiency. The risks associated with the design can be diminished by performing heat pipe development work prior to executing a detailed design. The radial-flow engine design forms the basis for the parametric section of the study. The details of the 150-KW<sub>e</sub> radial engine designs are presented in Section 3.0, followed by details of the parametric study in Section 4.0.

---

\*Thermacore, of Lancaster, PA, performed preliminary heat pipe design work for MTI on the Space Power Research Engine (SPRE) program.



89764

Figure 2-11. Branched Heat-Pipe Heater Arrangement in Radial Engine

### 3.0 DESIGN FEASIBILITY OF 150-kW<sub>e</sub> FPSE/LA RADIAL-FLOW ENGINE DESIGN

After selection of the radial engine concept, power module optimizations and design layouts were performed for both minimum specific mass and maximum efficiency configurations for 150-kW<sub>e</sub> output and a temperature ratio equaling 2.0.

The design objectives (power module thermal efficiency greater than 20% with specific mass less than 8 kg/kW<sub>e</sub>) were demonstrated at 150 kW<sub>e</sub>. The minimum specific mass design had a net efficiency of 26% and a specific mass of 5.5 kg/kW<sub>e</sub>. The maximum efficiency design achieved 34% net efficiency, but at the expense of increased mass, with a specific mass of 9.2 kg/kW<sub>e</sub>.

The maximum efficiency design is shown in Figure 3-1. Note that this design is significantly different from the initial scaled design listed in Table 2-1. Figure 3-2 shows the materials selected for the principal power module components. Details of the general radial engine design are given in the following sections, broken down into the pressure vessel, displacer drive, heat exchanger, alternator, and balancer assemblies.

#### 3.1 Pressure Vessel Assembly

All of the subassemblies are contained within the pressure vessel assembly, which consists of the hot-end and cold-end vessels. The structural criteria for the pressure vessel design require that the membrane stresses in the wall due to pressure do not exceed 2/3 yield or 1/2 ultimate stress at the cold end, and 2/3 rupture stress at the hot end.

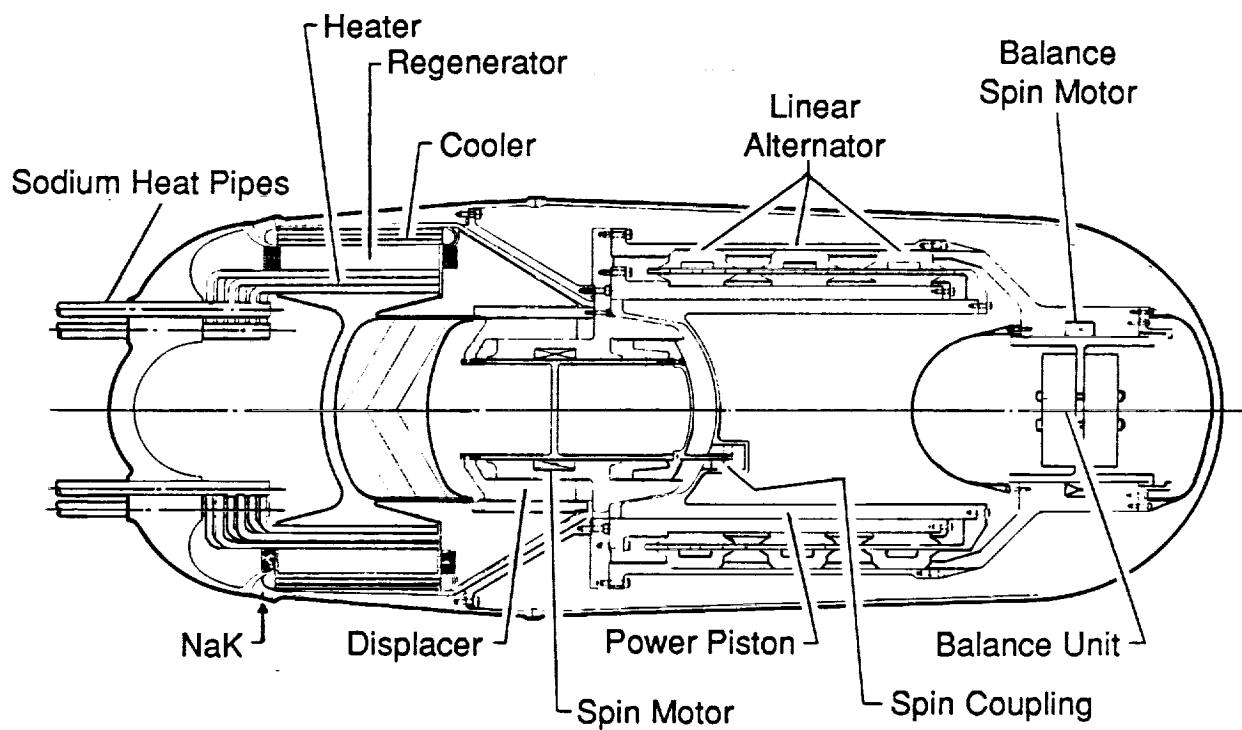
Design studies of the hot-end pressure vessel were made considering both cast and wrought superalloys. The cast Inco-713 material has one of the highest 60,000-hr creep rupture strengths\* of the superalloys at the 1050 K design temperature, but is difficult to weld. The wrought Inco-625 material is easily weldable, but has only moderate rupture strength and low yield strength (which is important in the cold section of the vessel). The wrought Inco-718 material also has good weldability and very high yield strength, but has low rupture strength. These material properties are summarized in Figures 3-3 and 3-4.

Due to the Inco-713 joining difficulties, the use of wrought alloys was desired for the hot-end vessel. To minimize weight, a bimetallic head was designed with a low-ratio (1.25:1) ellipsoid shape, using a hemispherical section between heat-pipe penetration (see Figure 3-5). The hot portion is made from Inco-625 welded to an Inco-718 outer section. The weld joint is located in the vessel midway between the heat-pipe penetration zone and the cooler outside diameter. Although the hot section is heavy, use of the high yield strength Inco-718 for the larger diameter cold section results in considerable weight savings. The calculated mass of the 625/718 head for the preliminary 150-kW<sub>e</sub> design was 171 kg at a mean pressure of 15 MPa.

To determine if weight could be significantly reduced by using Inco-713 for the hot-end vessel, an alternate head was designed, as shown in Figure 3-6. A 2:1 ellipsoid shape gave the minimum mass for the head, calculated to be 92 kg at a mean pressure of 15 MPa. To avoid the welding problem, a tapered, self-locking joint was designed to carry the axial pressure blow-off loads, with a braze joint between the Inco-713 and Inco-718 serving mainly to seal the vessel. Despite a significantly lighter vessel, the lock joint ring adds considerable mass (estimated to be 70 kg). The total weight (including lock ring) of 162 kg is only slightly less than that of the 625/718 head. Welding Inco-713 would allow considerable weight savings by eliminating the lock ring. Friction welding of Inco-713 has been demonstrated with

---

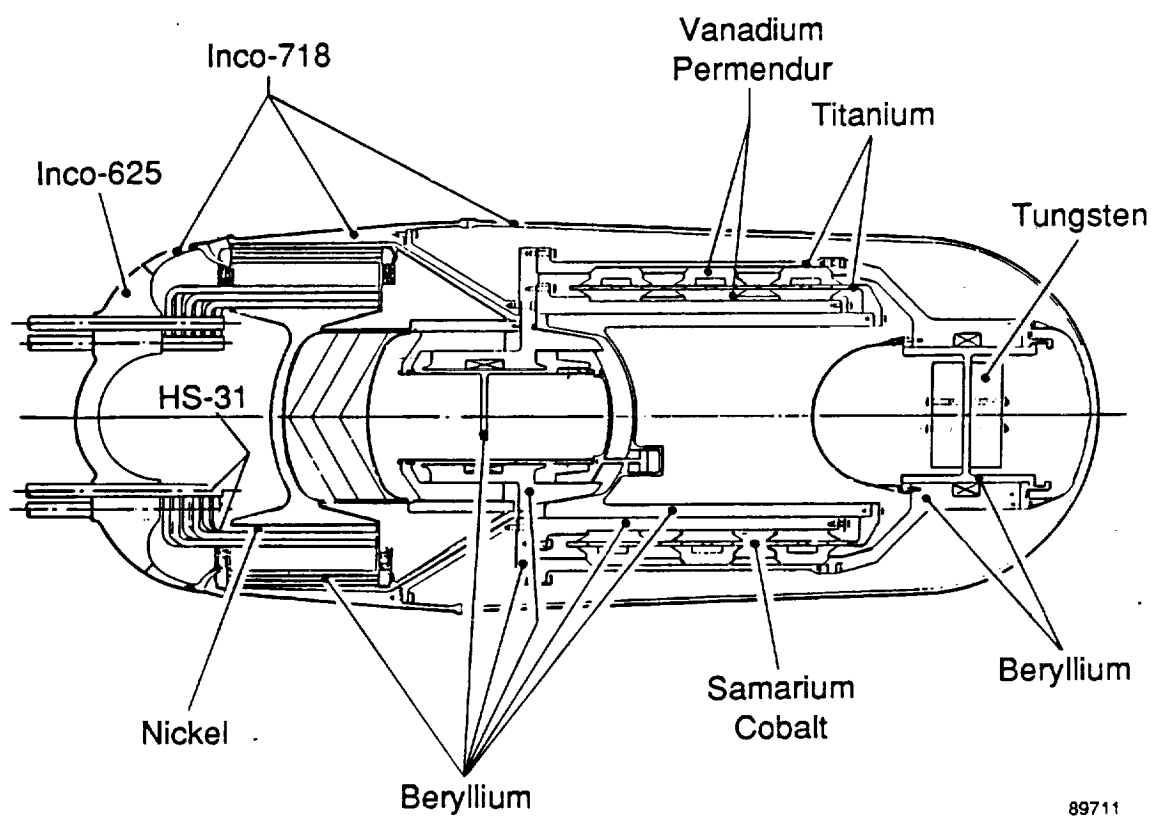
\*Estimated from limited data based on the Larson-Miller time-temperature parameter.



Overall Size: Diameter = 69 cm  
Length = 172 cm

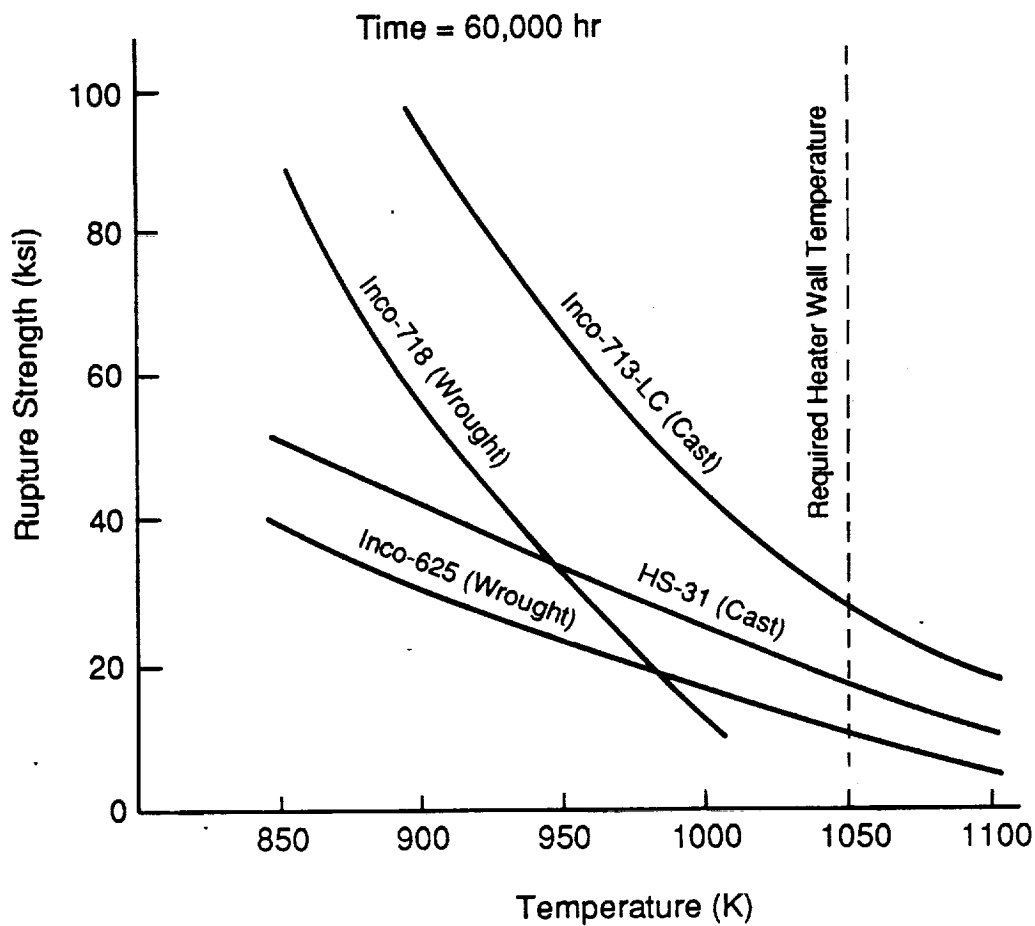
Figure 3-1. 150-kW<sub>e</sub> Free-Piston Stirling Engine/Linear Alternator

89766



89711

Figure 3-2. Materials for Space Power Free-Piston Stirling Engine Scaling Study



89712

Figure 3-3. Stress-Rupture Data Extrapolated from 1000-hr Data Using Larson-Miller Parameter



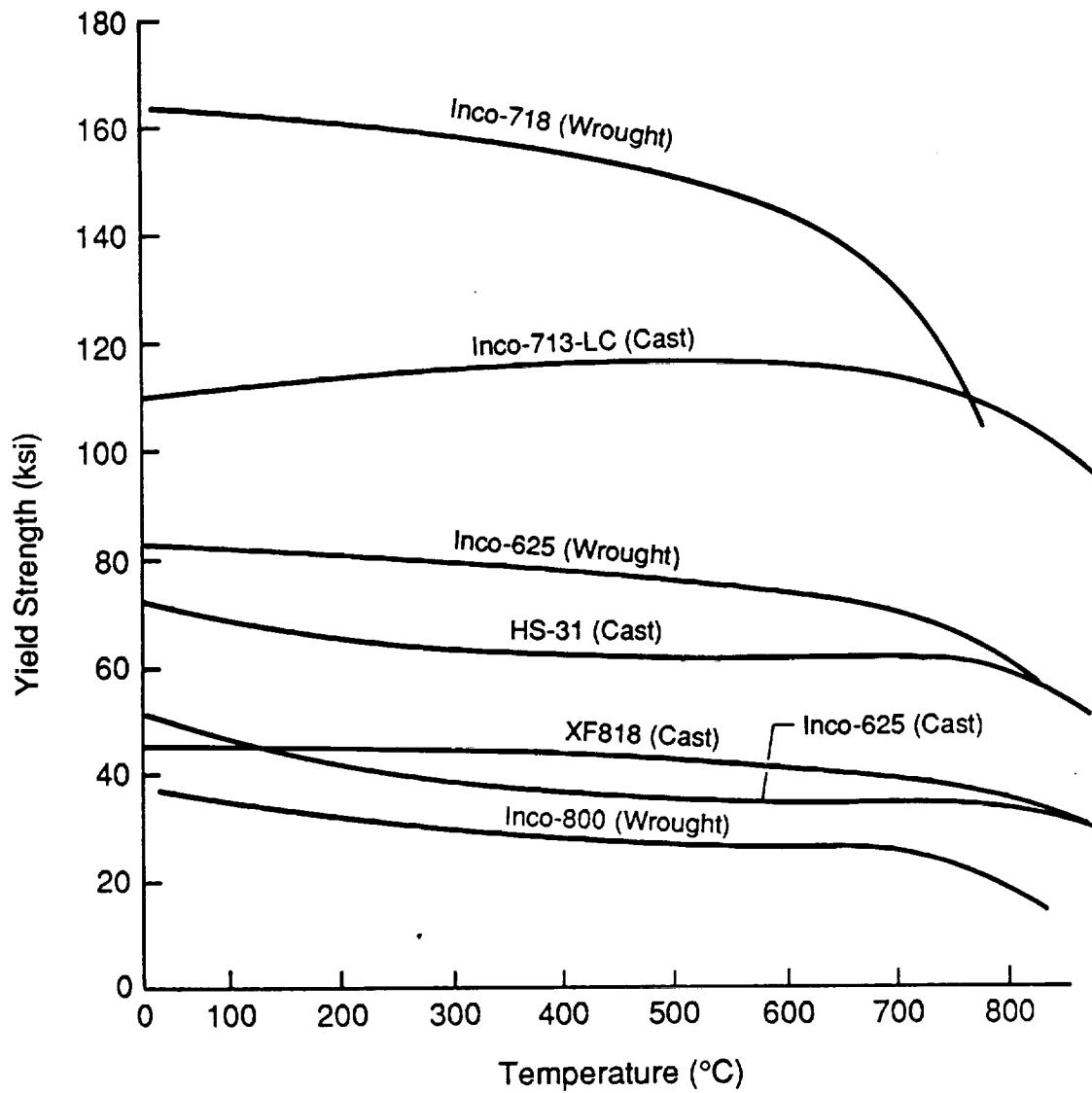
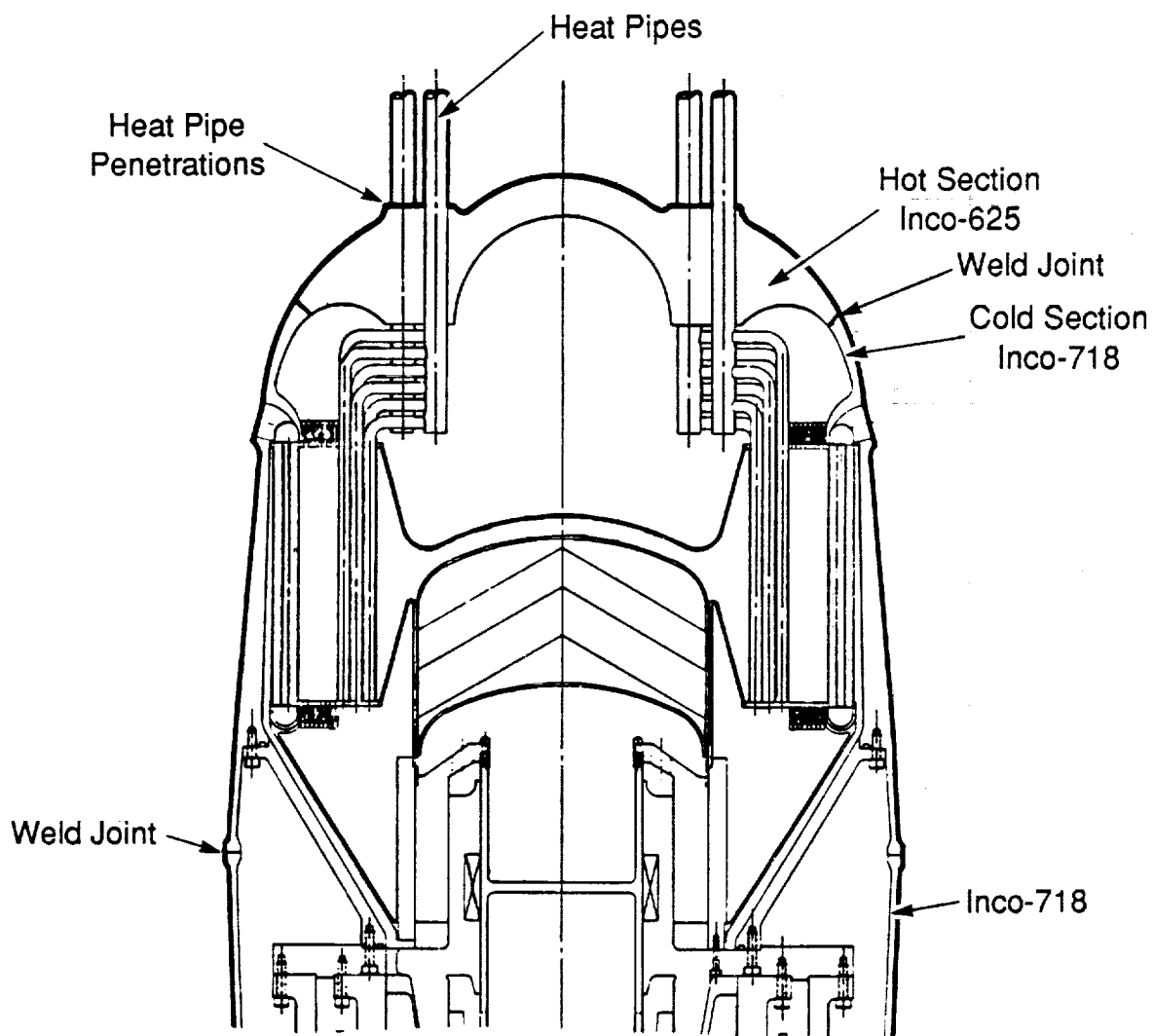


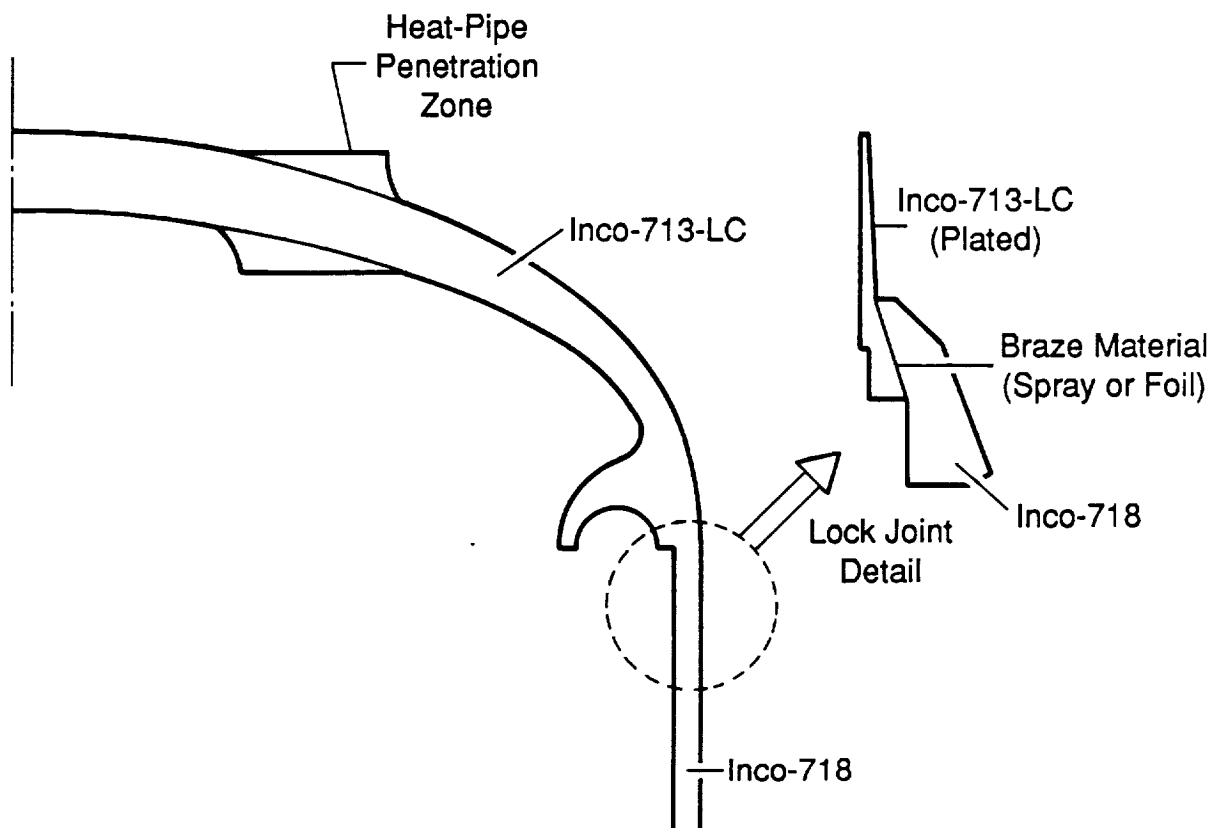
Figure 3-4. Yield Strength - High-Temperature Alloy

89713



89763

Figure 3-5. Bimetallic (Inco-625/Inco-718) Hot-End Pressure Vessel



89715

Figure 3-6. Inco-713-LC Hot-End Pressure Vessel with Lock Joint

turbine wheels, but development would be required to establish the welding procedure for a large-diameter pressure vessel. Based on the reduced risk with the wrought alloys, the bimetallic head was selected.

The bottom pressure vessel, which surrounds the displacer drive, alternator assembly, and balancer, is made from Inco-718, selected for its high strength and nonmagnetic characteristics. The end section is hemispherical, thereby allowing half the thickness as the cylindrical middle section. The vessel is welded to the Inco-718 section of the hot-end vessel at the maximum diameter location, adjacent to the middle of the displacer post.

### 3.2 Displacer Drive Assembly

The displacer drive assembly, shown in Figure 3-7, is similar to the posted displacer drives used on the SPDE and the earlier engineering model engine at MTI. The moving part of the assembly includes the dome at the hot end, which is welded to the support cone and skirt. The cone is bolted to one end of the rod, and the gas spring piston is bolted to the other end. The rod moves within the bore of the stationary post and flange member, to which the gas spring cylinder is attached.

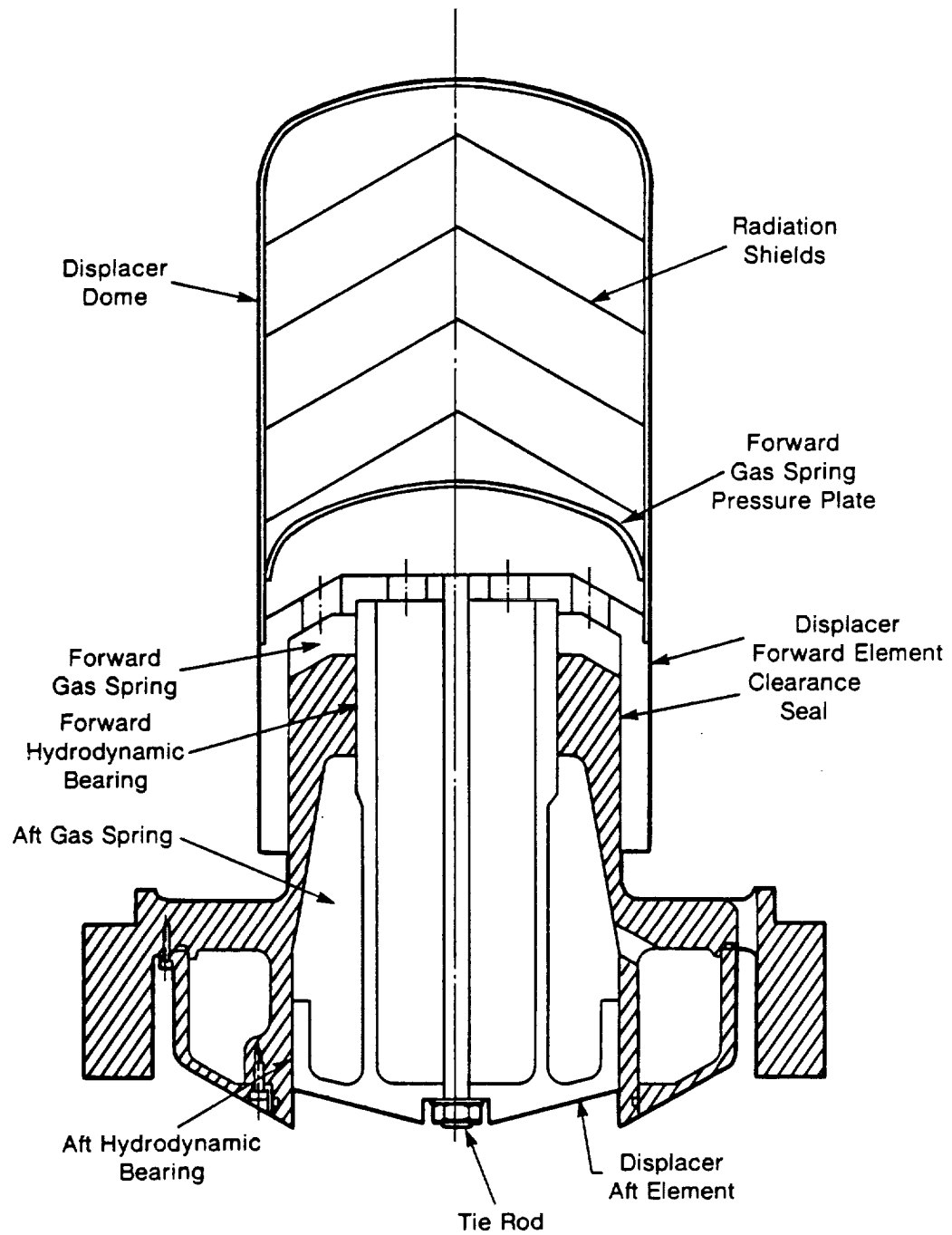
The displacer gas springs are designed with nearly equal stiffness, thereby balancing the displacer inertia with the lowest total gas spring loss. The upper spring comprises the volume between the support cone and the post, the volume between the support cone and the pressure cap, and the portion of the inside of the displacer rod that lies above the dividing bulkhead. The position of the pressure cap can be adjusted to achieve the required spring stiffness.

The lower spring uses the lower inside portion of the displacer rod and continues out to the gas spring cylinder. Additional volume can be added, as required, by hollowing out the post. All of the "cold" parts of the displacer assembly are made from beryllium to minimize mass and gas spring losses. Inconel is used for the displacer dome and radiation shields.

An electric induction motor is used to spin the displacer, which creates hydrodynamic gas films for its support. The spin motor design uses the rod of the displacer as the rotor, with the stator windings fixed in a slot in the post wall (see Figure 3-1). This design takes advantage of the electrical conductivity of the beryllium rod and uses no rotor windings, therefore adding no additional mass to the displacer. Eddy currents are induced in the beryllium rod by the rotating magnetic field set up by the stator windings, and the rod is dragged around with some slip. The motor efficiency is expected to be rather low (50%), but the required spin power for the 150-kW<sub>e</sub> engine is small (150 W). Therefore, dissipation of the motor losses is not expected to result in significant temperature gradients in the displacer drive. To avoid the addition of a separate spin motor for the power piston, the piston is coupled to the displacer. The coupling is a simple set of magnets arranged to repel (see Figure 3-8), but provides no axial coupling force. Two couplings are used to provide adequate torque for startup and to dynamically balance the spinning pistons.

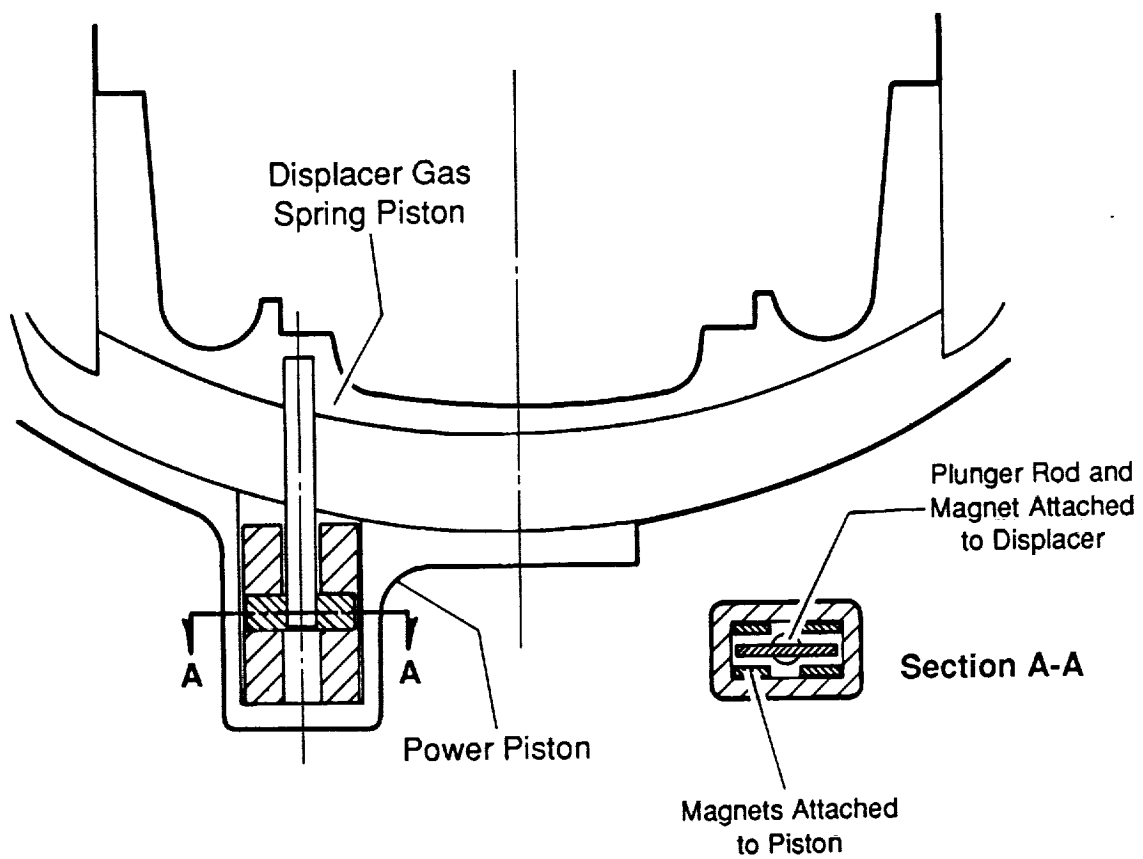
The motor and coupling were sized to handle the frictional loads of the displacer and power piston at startup, assuming horizontal attitude with 1-g gravity field (for ground testing). In order to reduce the start-up torque load to a reasonable level, the use of a hard nickel-boron coating on the bearing surfaces was assumed. Coefficients of friction as low as 0.05 have been reported for this coating [2]. The running torque is due only to bearing drag (negligible) and windage.

The estimated coupling specific mass is 0.01 kg/kW<sub>e</sub> for the displacer and 0.015 kg/kW<sub>e</sub> for the piston.



88788

Figure 3-7. Typical Displacer Drive Design



89714

Figure 3-8. Coupling Detail for Hydrodynamic Gas Bearings

### 3.3 Heat Exchanger Assembly

The heat exchangers of the radial engine form an annular assembly. The heater is encircled by the regenerator, which in turn is surrounded by the cooler. The engine working fluid flows radially in and out through the heat exchangers, giving the engine configuration its name. As mentioned in Section 2.2, the heater and cooler are constructed from stacks of thin metal plates, spaced to form gas-flow passages arranged in a radially spoke-like pattern. The heater heat pipes and cooler coolant pipes are inserted into holes through the stack of plates, and the assembly is furnace-brazed to form a compact heat exchanger unit. The radial distance between pipes and the distance between the pipe surface and the gas channel base are set to 1 mm to provide a reasonable plate web. This distance also minimizes the temperature drop between engine gas and the heat source, or sink.

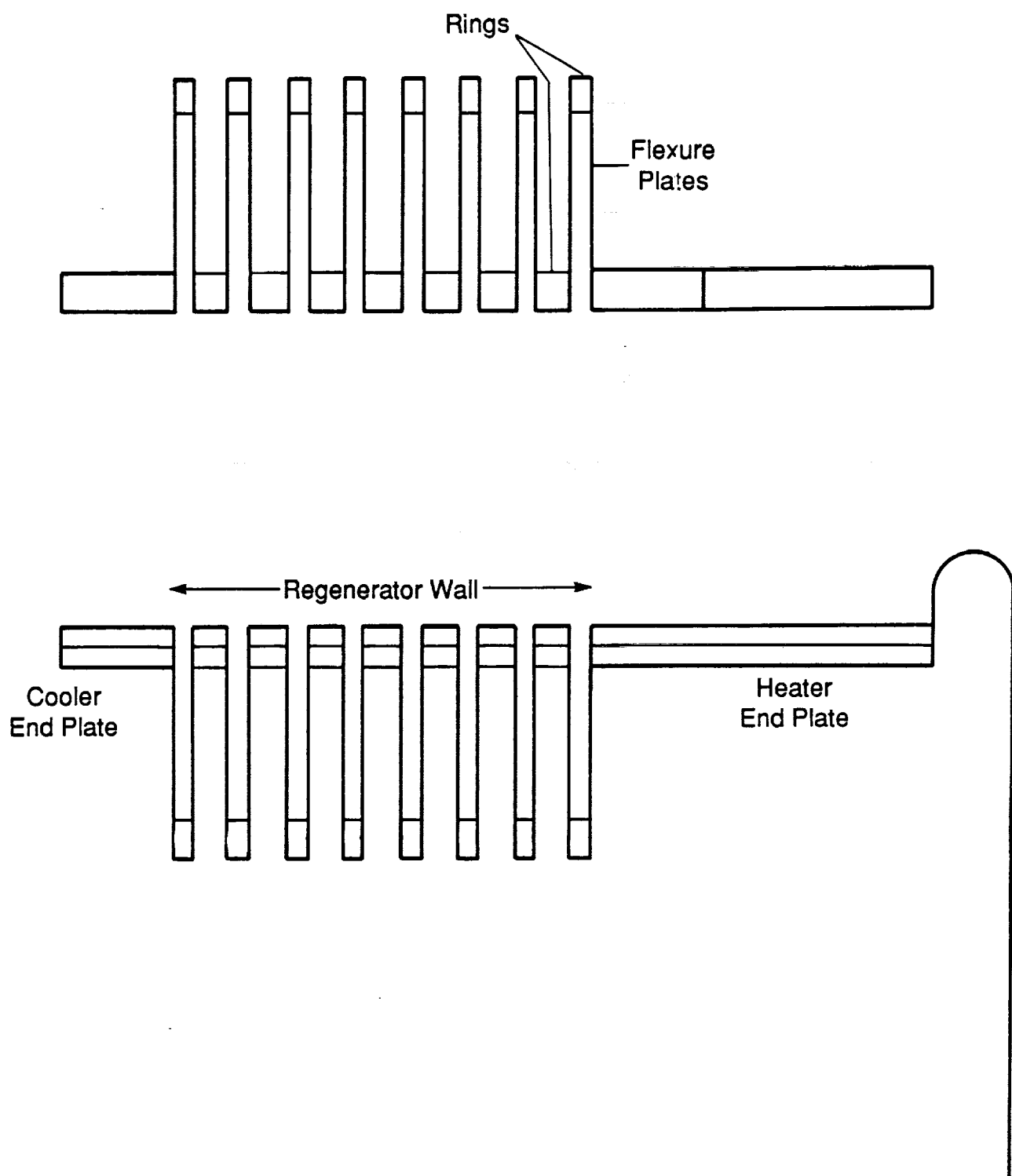
For the heater, nickel-201 is used for the plates because of its good thermal conductivity, giving a heater surface effectiveness greater than 85%. Beryllium is the material selected for the cooler plates because of its good thermal conductivity and low density. The cooler surface effectiveness is greater than 90%. Beryllium replaces the aluminum used for the cooler fins during the concept selection phase because of a better thermal expansion match with the surrounding structure.

Since the heat exchangers are located inside of the engine pressure vessel, the heat exchanger walls (end plates) are subjected to only the engine pressure amplitude, typically 10 to 15% of mean pressure. This results in considerable weight savings compared to the modular heat exchanger walls, which carry the full pressure load. The radial temperature gradient across the regenerator wall does introduce a difficult stress condition, but analysis has shown that a bellows type of segmented wall (shown in Figure 3-9) allows for the radial expansion of the regenerator with acceptable stress levels. The minimum radial length of the regenerator from stress considerations is governed by the regenerator diameter and the temperature difference between heater and cooler. For an engine temperature ratio of 2.0, the minimum regenerator length is 8% of the mean regenerator diameter. The minimum regenerator length increases with increasing temperature ratio.

The regenerator matrix can be constructed by rolling screen around a mandrel of the same diameter as the outside of the heater. Another approach is to use felt metal, which can be easily fabricated to the desired shape. In engine tests, felt metal regenerators have produced thermodynamic performance similar to screen regenerators.

The dimensions of the heat exchangers vary considerably between the minimum mass and maximum efficiency designs. For example, at the 150-kW<sub>e</sub> power level at a temperature ratio of 2.0, the axial height of the heat exchangers varies from 140 mm for the minimum mass design to 200 mm for the maximum efficiency design.

The inside diameter of the heater was minimized for the minimum mass designs since the hot-end pressure vessel diameter is set by the outside diameter of the cooler, and the cooler diameter changes with heater diameter. The requirements of the heat transport systems and their close relationship with heat exchanger size are discussed in the following sections.



89716

Figure 3-9. Segmented Regenerator Wall Concept Schematic



### 3.4 Heat Transport Systems

#### 3.4.1 Heater Heat Pipes

To provide a uniform gas-side heater wall temperature while minimizing the temperature drop between the heat source and the engine working fluid (helium), the ideal heat-pipe heater interface\* for the radial engine configuration would consist of narrow, oblong-shaped heat pipes with the helium flowing past the long wall, as sketched in Figure 3-10. The temperature drop would then only be across the heat-pipe wall, and the heat would be distributed at an even temperature to the helium. However, the heat-pipe walls must carry the full engine pressure, and noncircular tubes do not make efficient pressure vessels. The oblong pipe would require internal supports and thick walls, resulting in excessive heat-pipe weight and large wall temperature drop.

In order to achieve a relatively even temperature distribution along the gas channels, round heat pipes of a small diameter are used. This minimizes the distance between heat pipe and channel. The minimum heat-pipe inside diameter based on current technology\*\* is 9.5 mm. Heat-pipe performance predictions are discussed in Section 4.2.

In order to maintain reasonable specific mass of the engine pressure vessel, the diameter of penetrations through the vessel in the hot zone must be kept small. Increasing the penetration diameter results in a direct mass increase of the spherical-shaped hot section of the pressure vessel. Therefore, the number of penetrations must be minimized.

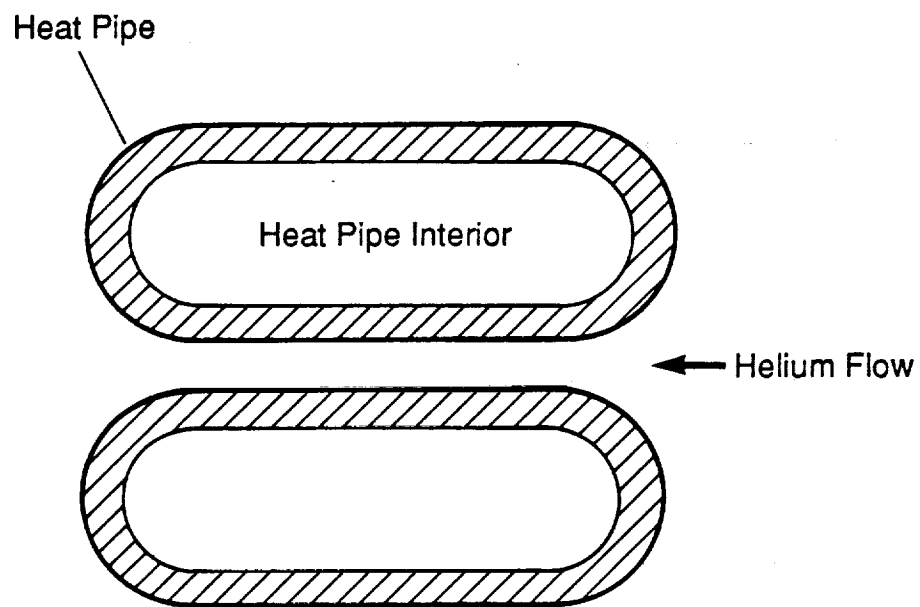
For all of the engine designs investigated in the parametric analysis portion of this study, the number of penetrations giving reasonable pressure-vessel specific mass was less than the number of small-diameter heat pipes needed in the heater. Therefore, it was necessary to branch the main pipes that penetrate the vessel into the smaller pipes that mate with the heater, as shown in Figure 2-11. At the 25-kW<sub>e</sub> engine size, the number of heat-pipe branches per main pipe is three. When the engine is scaled to 150 kW<sub>e</sub>, the diameter of the main pipes must be increased to keep the penetration diameter small relative to the vessel diameter outboard of the cooler. For constant axial heat flux density in the main pipes, the number of main pipes increases at a slower rate than the power level. However, because the branch pipe diameter was fixed at 9.5 mm, the number of branch pipes increases proportional with power level. Thus, the number of branch pipes per main pipe must increase with power level, increasing to six at 150 kW<sub>e</sub>. The concept of using branched heat pipes is not totally new, but is not standard practice and requires development testing.

Selection of the heat-pipe wall material was another difficult area. Several material options were investigated in the course of the engine design. The high engine mean pressure causes compressive hoop stress in the pipe wall. Therefore, compressive creep and buckling of the heat pipes must be considered. The material strength requirements are based on the stress-rupture strength and 1% creep strength at an average material temperature of 1100 K. Since test data on the compressive creep of superalloys is very sparse, the more typical tensile creep data was used for design calculations. However, available test data on UDIMET 700 shows compressive creep to be significantly lower than tensile creep (see Figure 3-11). The pipes were designed with a safety factor of 1.5 using the tensile creep-rupture data, so the design may prove to be conservative. Compressive creep tests need to be performed on selected materials to establish a less conservative design basis. For buckling, a safety factor of 2.5 was used due to the large uncertainties in prediction of the onset of buckling. For all designs in the study, creep rupture of the heat pipes was the limiting constraint.

---

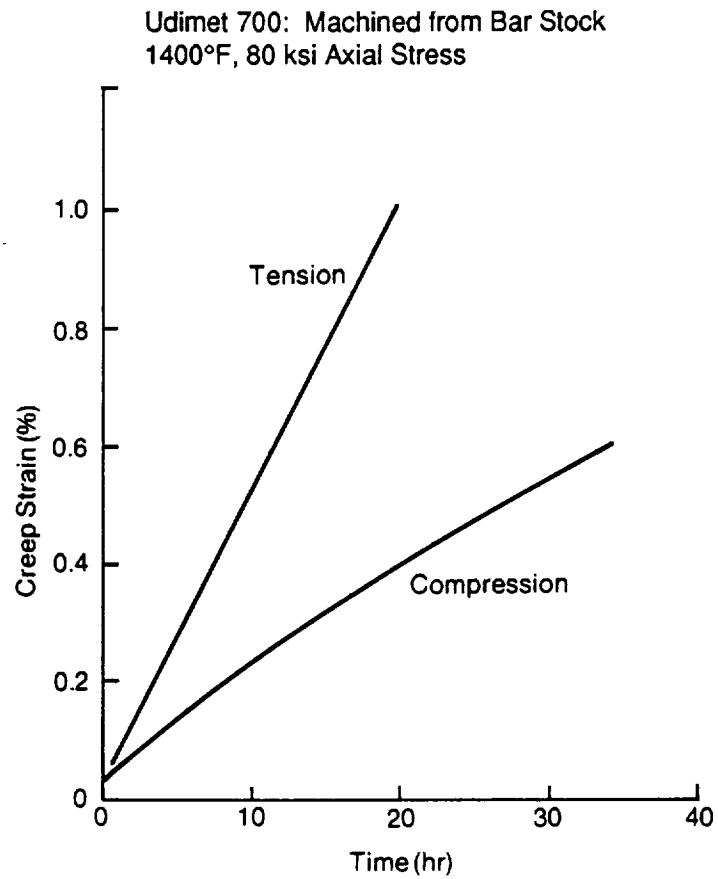
\*Based on the engine heater frontal area and surface area requirements for good performance.

\*\*Based on Thermacore information for arterial heat pipes.



89717

Figure 3-10. Ideal Heat Pipe Based on Engine Heater Requirements



881012

Figure 3-11. Compression-Creep Curves as Compared to Tension-Creep Curve for Udimet 700

The materials considered for the heat-pipe wall included the nickel-based superalloys Inco-713 and Inco-625, and the cobalt-based superalloys HS-31 and HS-25\*. Due to the welding difficulties associated with Inco-713, it was eliminated from consideration. Heat-pipe wall temperature drop and wall compatibility with sodium were the main concerns in material selection. Wall thickness and wall WT (assuming 2.5-kW heat load per pipe, 9.5-mm heat-pipe ID, and 100-mm condenser length) for the materials considered are as follows:

Heat Pipe Material	Wall Thickness (mm)	Wall $\Delta T$ ( $^{\circ}C$ )
HS-31	1.18	34.0
HS-25	1.79	52.0
Inco-625	2.17	69.0

Based on NASA-LeRC recommendation, a large wall  $\Delta T$  is unattractive due to increased sodium corrosion with increasing temperature. The wall  $\Delta T$  can be reduced by increasing the heat transfer area, but it is done at the expense of increased engine mass, both directly and indirectly. The former is due to increased heat exchanger size, while the latter is due to the increase in engine volume. The increase in engine volume requires an increase in engine displacement to maintain engine pressure amplitude and power generation (larger pistons or longer stroke, leading to increased engine structural mass). Note that a less conservative design basis for compressive creep would also reduce the wall thickness and  $\Delta T$ .

The cobalt alloys are reported to have reasonably good compatibility with liquid metals [3], and no protective corrosion liner is assumed necessary. Nickel-based alloys are reported to be more susceptible to attack and would require some protection.

Based on these considerations, HS-31 was selected as the heat-pipe wall material. HS-31 is a cast alloy with relatively poor welding characteristics. However, according to material specialists contacted during this study, acceptable welds are possible with tight control of alloy composition.

### 3.4.2 Coolant System

The coolant system for this study was specified by NASA-LeRC to be a pumped NaK loop. The primary flow restriction on the engine side of the loop is the penetration through the pressure vessel wall. For the baseline 150-kW<sub>e</sub> design, a maximum of twenty-eight 38-mm diameter penetrations are allowed based on structural requirements for the load-carrying capability of the vessel, with 14 inlets and outlets each in the same plane. As shown in Figure 3-12, each inlet feeds two groups of coolant tubes in the cooler, connected in series.

Details on the selection of the coolant tube diameter and NaK mass flow rate are discussed in Section 4.2.

### 3.5 Alternator Assembly and Power Piston

The alternator assembly is composed of the power piston and cylinder, around which is wrapped the moving-magnet, permanent-magnet alternator (see Figure 3-1). The alternator plunger is cylindrical in shape and cantilevered off the back of the power piston in a reflexed fashion. The power piston and cylinder are straight bore designs to permit the use of very tight clearance-to-diameter ratios. The hydrodynamic piston bearing is incorporated into the bore area. The alternator inner stator is attached to the outside of the power piston cylinder. The outer stator is attached to a lightweight support cylinder, which is bolted to the main engine flange.

---

\*The cobalt alloys are also known as X-40 and L-605, respectively.

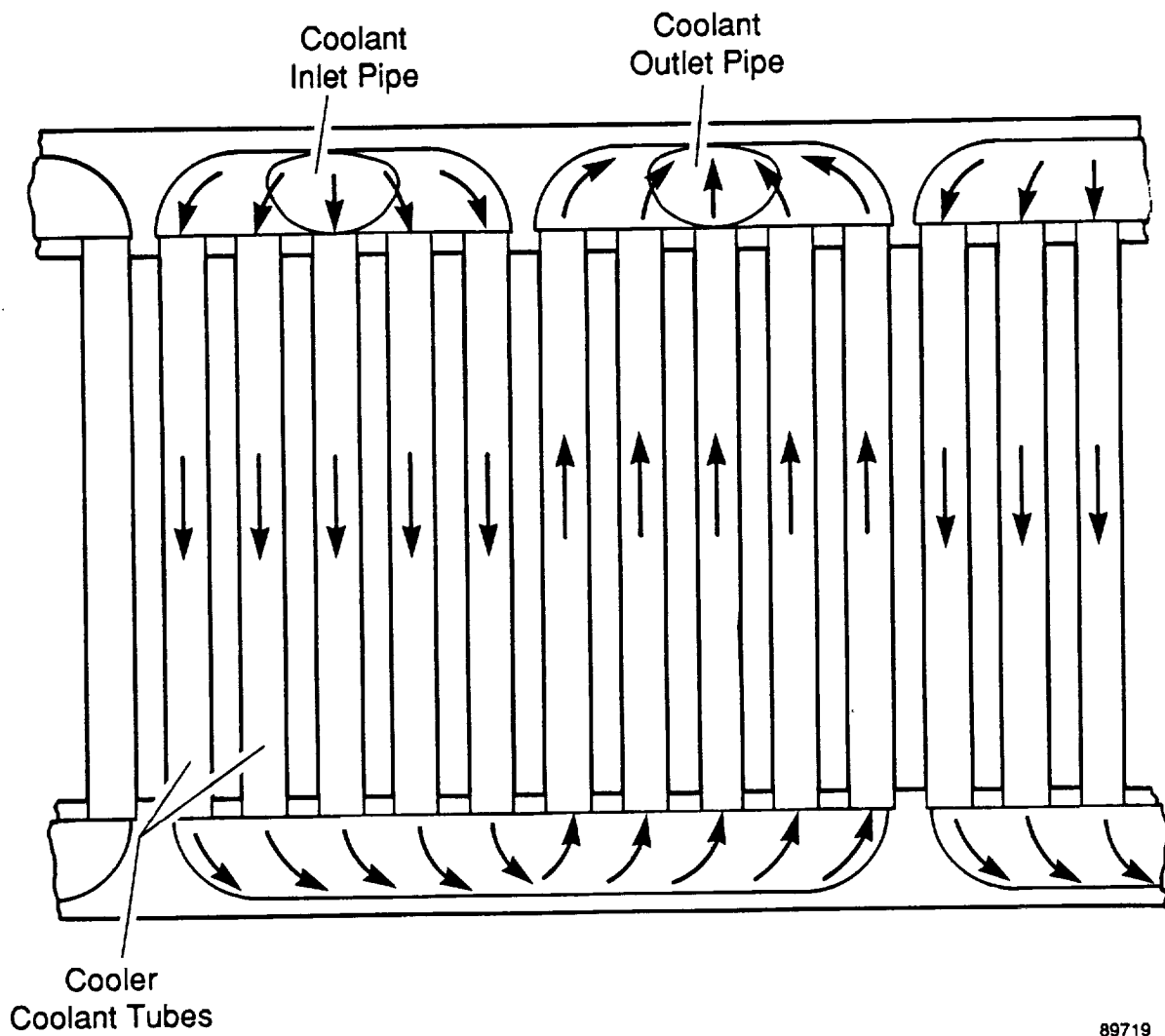


Figure 3-12. Radial Engine Cooler Coolant Flow Schematic

The alternator plunger moves between the inner and outer stators in the gap, which for the baseline 150-kW<sub>e</sub> design is 11 mm. Samarium-cobalt permanent magnets make up most of the plunger, with the magnet thickness filling 80% of the gap. The magnets are radially magnetized, with four magnet rings of alternating polarity per coil section. The plunger is structurally strengthened with a titanium cage made of struts and end rings. This strength is necessary to support the magnets, which have little tensile strength against the inertial forces due to axial reciprocation, and to provide circumferential stiffness. The struts have a rectangular section with round threaded ends to attach to the end rings. They occupy approximately 5% of the plunger cross section (magnets make up the remaining 95%).

The stators are made of Vanadium Permendur (Hyperco-50) tapered laminations (0.36-mm average thickness). The outer stator laminations are tapered to minimize the space between laminations at the outside edge and to reduce the stator OD. The coil slot is rectangular in cross section, which allows the use of square wire to give an increased packing factor. However, circular wire was assumed for this study, with a packing factor of 60%.

The power piston is supported on a hydrodynamic gas bearing at the outside diameter of the piston. The power piston seal clearance is set to 12.7- $\mu$ m radial clearance for piston diameters up to 152 mm, and increases linearly with diameter thereafter. The piston and cylinder are made from beryllium.

Depending on the stiffness requirements, the piston gas spring can be designed to use just the piston interior, or the entire volume around the alternator out to the pressure vessel as well as the piston interior. In the former case, an inside piston cylinder is required in addition to the primary cylinder, with the inner cylinder supported by a connecting piece bolted to the end of the alternator support cylinder. Since the inner cylinder is positioned relative to the alternator support, the inner seal clearance is increased by 30% to allow for tolerance stackup.

### 3.6 Dynamic Balancer Assembly

The balancer assembly includes the dynamic balance mass, balance cylinder and gas springs, and support connections (see Figure 3-1). The balance cylinder is supported by a connecting structure that bolts to the end of the alternator stator support. The balance cylinder and the structure of the balance mass piston are made from beryllium. Bolted to the center web of the balance piston is a disc of heavy material (tungsten or depleted uranium), which provides the bulk of the balance mass. The balance piston is supported on a hydrodynamic bearing and is spun by an independent induction spin motor of similar construction to the displacer/piston spin motor. Two balancer gas springs are used, with the required stiffness divided equally between them. The seal between gas springs is a clearance seal and also acts as the bearing surface. Pressure caps for the gas springs are attached to the balance cylinder.

## 4.0 PARAMETRIC STUDY

The scaling and parametric analysis tasks of this study required analysis of the power module performance and specific mass, as well as analyses of the power module subsystems. This section summarizes all of the analytical work performed in support of these tasks, followed by discussion of the parametric study results.

### 4.1 Parametric Study Requirements and Procedure

The first 150-kW<sub>e</sub> radial engine layouts were for minimum mass and maximum efficiency configurations at a temperature ratio of 2.0. These layouts were completed to demonstrate the design feasibility of a single-cylinder FPSE/LA producing 150 kW<sub>e</sub>. This required addressing all aspects of the engine and alternator design to the level required to demonstrate concept feasibility and determine component masses. With feasibility demonstrated, characteristics of designs at other operating points were generated by performing design optimizations to meet the particular design objective, as explained below.

The goal of the parametric study was to determine the relationships between power module thermal efficiency, power module specific mass, power output, and temperature ratio. This entailed performing a parametric study of power module performance over a temperature ratio range of 1.7 to 3.0, and over a power range from 25 to 150 kW<sub>e</sub>. Plots of the results were made and an empirical relationship was derived for power module thermal efficiency as a function of power module specific mass, power output, and temperature ratio.

The 12 operating points for the study were defined as follows: three power levels - 25, 75, and 150 kW<sub>e</sub>, with four temperature ratios (1.7, 2.0, 2.5, and 3.0) at each power level. Separate power module optimizations were performed at each operating point for each of the following goals:

- Maximum power module thermal efficiency
- Minimum power module specific mass
- Maximum ratio of power module thermal efficiency to power module specific mass (referred to as the baseline designs).

With three power module optimizations performed at each operating point, a total of 36 design optimizations were required.

In order to evaluate power module characteristics, performance predictions were required of the engine thermodynamics, engine mechanical systems, and alternator, as well as calculations of power module specific mass. A computer model of the engine/alternator geometry was developed that enabled calculation of the power module weight as a function of component sizes. The heat exchanger geometries were specified through input variables. The power module optimizations involved varying the heat exchanger parameters to achieve the optimization objective (maximum efficiency, minimum mass, or baseline design).

The heat exchanger parameters varied in the optimizations define the geometry of the heat exchangers and connecting ducts, as follows:

- Heater and Cooler
  - Flow passage dimensions (height, width, and length)
  - Fin thickness
  - Number of parallel passages

- Regenerator
  - Frontal area
  - Length
  - Porosity
- Connecting Ducts
  - Flow area
  - Hydraulic diameter.

These parameters were automatically varied by the code to search for the maximum or minimum of the objective function. The engine operating conditions (mean pressure, frequency, and piston strokes) were manually selected at each operating point to maintain control over the design.

The optimization procedure used by the code involved the following steps:

1. Select optimization parameter; calculate power module performance for starting value.
2. Vary parameter between preselected lower and upper bounds, calculating performance at each point. Select parameter value that results in the maximum or minimum of the objective function.
3. Repeat Steps 1 and 2 for each selected optimization parameter.
4. Repeat passes through set of optimization parameters until performance is unchanged between successive sweeps.
5. Return data file incorporating the set of optimized parameters.

The 36 operating points of the study were for single-cylinder engines using dynamic balancer assemblies for vibration control. If two identical power modules are connected in an opposed, in-line configuration, the resulting power module is dynamically balanced and the balance unit becomes unnecessary. The performance and specific mass of opposed power modules (at twice the power levels, e.g., 50, 150, and 300 kW<sub>e</sub> per power module) are reported in Section 4.4.

Each calculation of power module performance requires calculations of thermodynamic, gas spring, alternator, and balancer performance. Module net power output is held constant for each point in the optimization via adjustments of engine displacement (piston diameters).

## 4.2 Power Module Analysis

### 4.2.1 Engine Thermodynamics and Dynamics

The thermodynamic analysis of the power module was performed using the MTI harmonic analysis code HFAST. Generation of power module characteristics over a range of specific mass levels required 36 engine optimizations, as discussed in Section 4.1.

Helium was specified as the engine working fluid in the design specifications. The heater metal temperature was specified as 1050 K (gas-side wall temperature), with the cooler wall temperature a function of the specified temperature ratio at a given operating point.

**4.2.1.1 Piston and Displacer Stroke and Phase Angle.** Prior to performing the optimizations, the relationship between expansion volume amplitude and compression volume amplitude was investigated to determine the ratio giving the best performance. This relationship was then held fixed for all design points.



Figure 4-1 shows indicated engine efficiency as a function of  $\Delta V_e / \Delta V_c$ , where  $\Delta V_e$  is the expansion space volume amplitude (displacer hot side area multiplied by displacer stroke amplitude), and  $\Delta V_c$  is the compression volume amplitude due to the power piston (piston area multiplied by piston stroke amplitude). The maximum efficiency occurs in the range of  $\Delta V_e / \Delta V_c = 0.55$  to 0.7, which holds over the entire range of different mean pressure and frequency conditions considered in the study. For all points in the study, the value of  $\Delta V_e / \Delta V_c$  was set to 0.7 based on the good efficiency level and the similarity with previous FPSE designs. This amplitude ratio can be achieved by various combinations of piston and displacer diameters and strokes, and selection of the "best" stroke-diameter relationship involves mechanical as well as thermodynamic considerations.

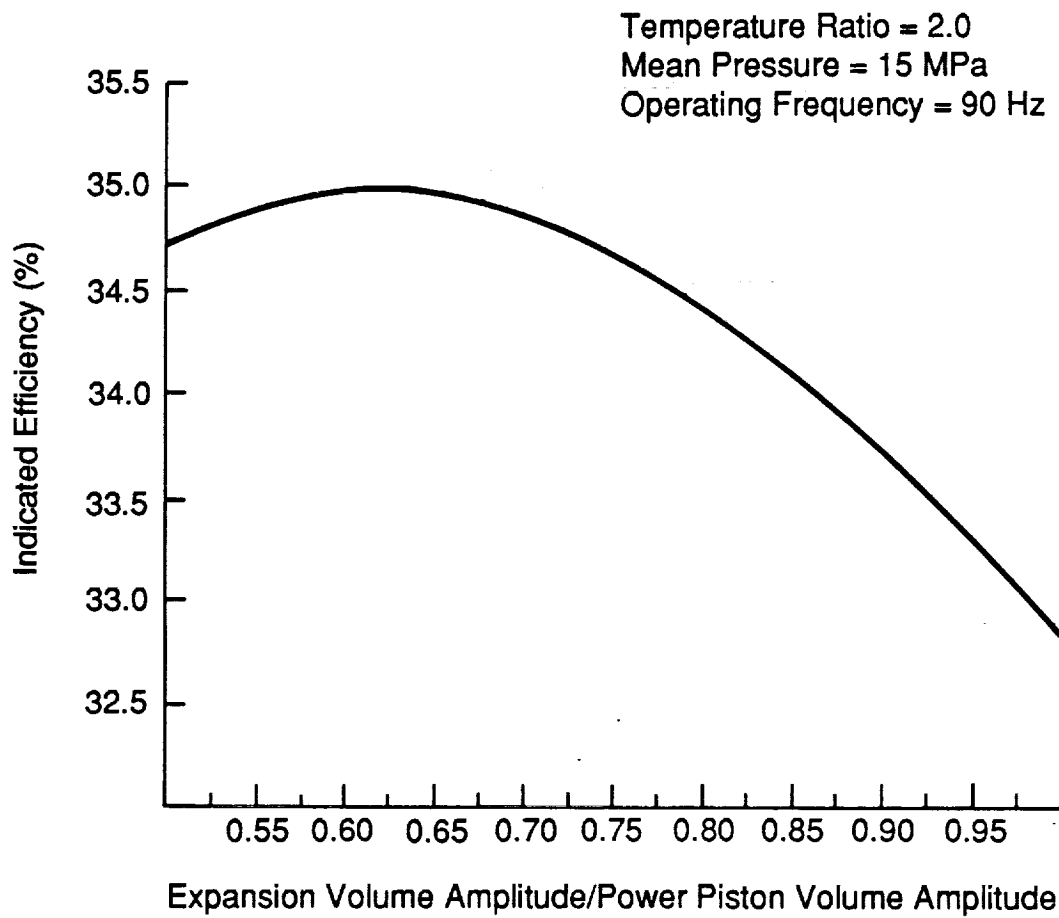
A smaller piston diameter and a longer stroke result in increased gas spring losses. Piston mass decreases with decreasing diameter, but not enough to offset the decreasing gas spring stiffness. Therefore, the gas spring pressure amplitude must be increased. An increase in gas spring pressure amplitude results in higher gas spring hysteresis loss. Gas spring seal leakage can increase or decrease, depending on the rate of change in seal clearance with diameter. On the compression space side of the piston, the seal leakage drops with decreasing piston diameter. The selection of piston stroke is made based on the trade-off between engine and gas spring losses, power module specific mass, dynamic tuning requirements, and alternator considerations. Discussion of the alternator is provided in Section 4.2.3.

The displacer gas spring losses also increase with increasing stroke, while the engine thermodynamic losses decrease (expansion space hysteresis loss drops due to decreasing surface area, appendix gap enthalpy flux drops due to decreased leakage, but shuttle conduction loss increases). The mass of the displacer drive assembly drops with increasing stroke, but increased stroke increases the length of the displacer drive and makes the bearing design more difficult. Based on trade-offs of these considerations, the largest displacer stroke that would accommodate a reasonable displacer drive design was desired for all operating points in the study.

The displacer-to-piston phase angle ( $\phi_d$ ) was set to  $65^\circ$  for all points in the study based on considerations of efficiency and power generation (Figures 4-2 and 4-3). Engine efficiency increases at lower  $\phi_d$  because of decreasing mass flow through the heat exchangers and lower pumping loss in the engine. On the other side of the coin, the power generated by the engine for a given piston displacement is maximum for  $\phi_d$  of  $75^\circ$  to  $90^\circ$ , and decreases with decreasing phase angle. Thus, the selection of  $\phi_d$  reduces to a trade between efficiency and specific mass, and the choice of  $\phi_d = 65^\circ$  is valid over the entire range of operating condition considered in the study.

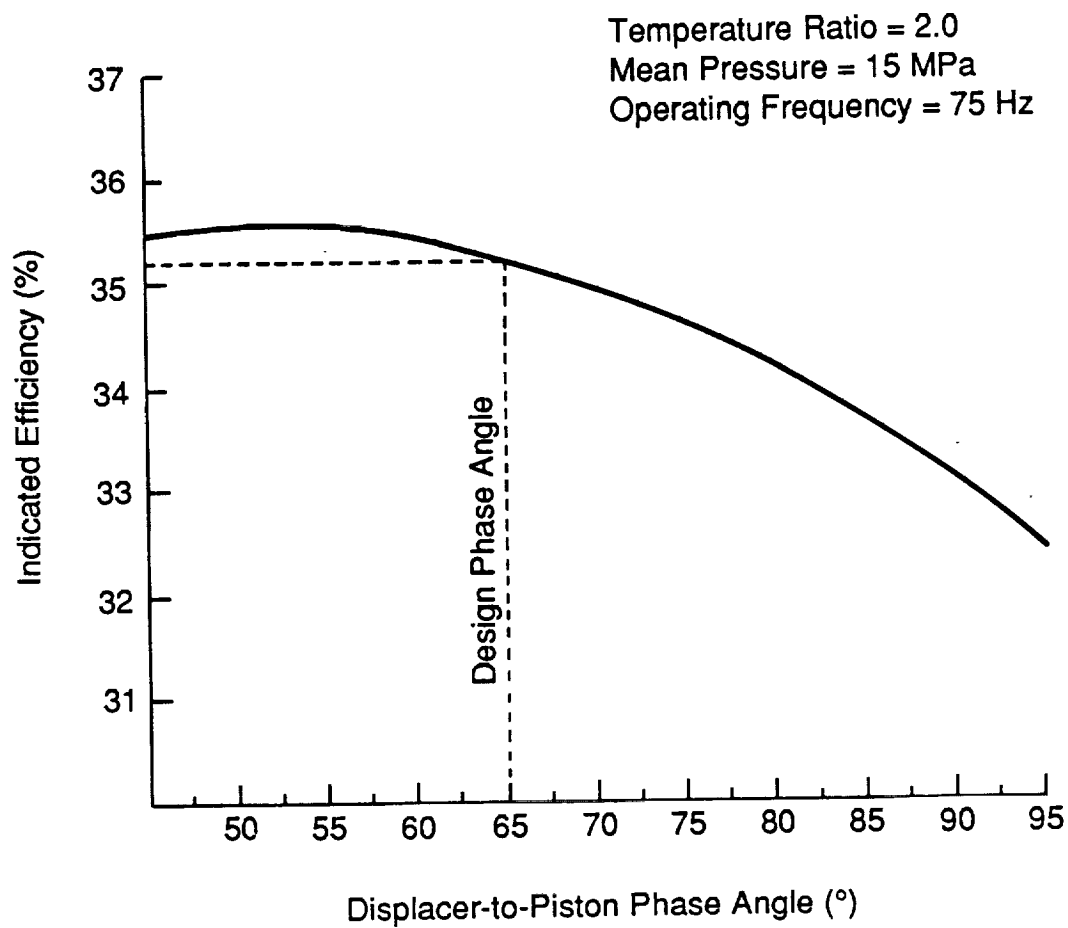
To maintain the desired power during optimizations, the piston area and displacer area were automatically adjusted. The piston and displacer strokes were selected for each point in the study prior to the optimization, taking the engine thermodynamic and mechanical efficiencies and power module specific mass into consideration.

**4.2.1.2 Heat Exchanger Considerations.** The selection of the channel and fin dimensions for the heat exchangers was made automatically by the optimization code based on considerations of thermodynamic efficiency (dependent on fin effectiveness, hydraulic diameter, flow area) and heat exchanger specific mass. For the heater, use of nickel for the fins resulted in a high fin effectiveness, and therefore allowed a significant increase in surface area from that of the fin base area. For example, the 150-kW<sub>e</sub> baseline design used fins with a length- (to the middle of the helium flow channel) to-thickness ratio of approximately 4. The resulting hydraulic diameter (flow area per unit wetted perimeter) of the heater channels was very small as compared to that achieved with previous engine designs (0.5 mm versus 1.25 mm for the SPDE shell-and-tube heater), resulting in higher heat transfer and improved efficiency. The specifics of flow passage dimensions varied between different optimization points, but small hydraulic diameter resulted for all points.



89718

Figure 4-1. 150-kW<sub>e</sub> Radial Engine Indicated Efficiency versus Hot-to-Cold Volume Amplitude Ratio



89720

Figure 4-2. 150-kW<sub>e</sub> Baseline Design. Indicated Efficiency versus Displacer-to-Piston Phase Angle

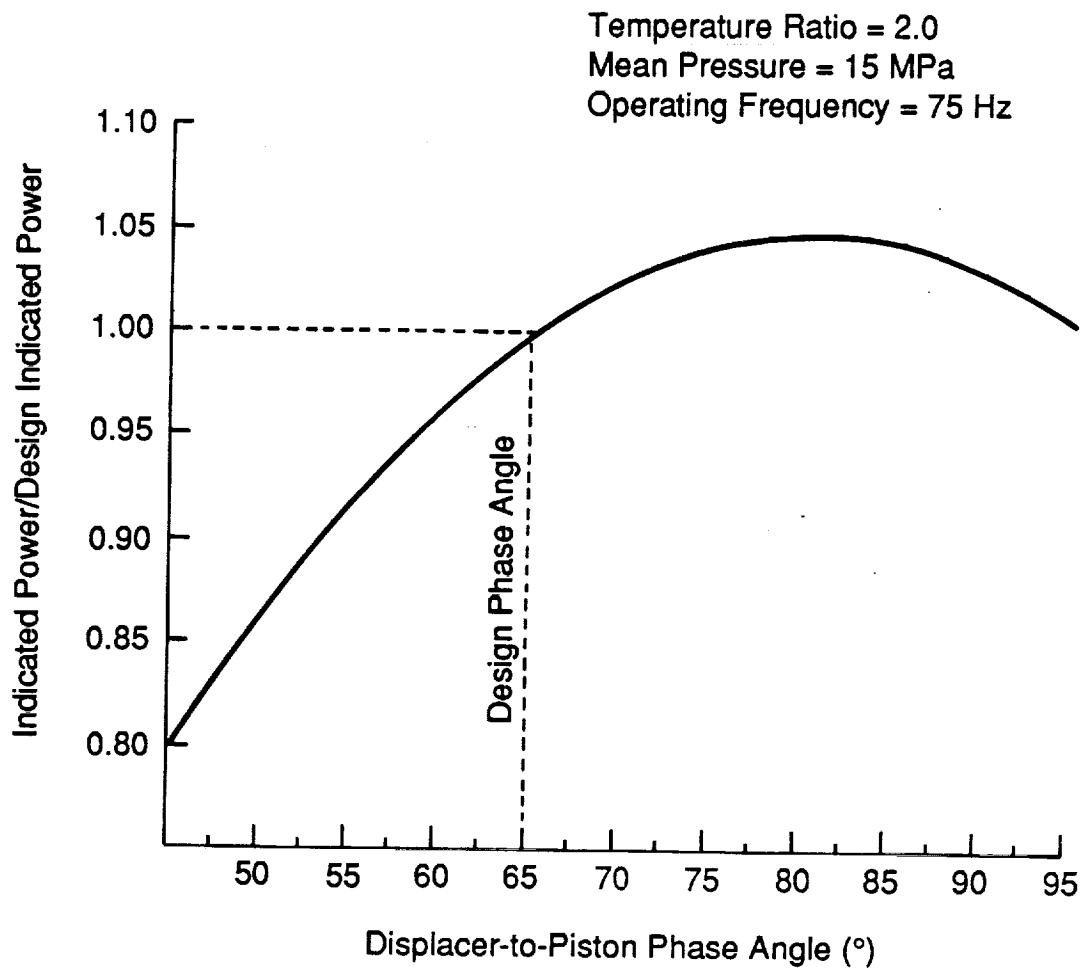


Figure 4-3. 150-kW<sub>e</sub> Baseline Design. Normalized Power versus Displacer-to-Piston Phase Angle

891021

In the cooler, high-conductivity copper was initially considered for the fin material, but the cooler specific mass was undesirably high. Aluminum and beryllium have low density and high thermal conductivity, resulting in high fin effectiveness and low mass. Beryllium was selected as the prime material due to the close match of thermal expansion coefficient with the Inconel coolant tubes. Similar to the heater, the cooler hydraulic diameter is quite small relative to other designs.

The frontal area of the regenerator has a major impact on the thermodynamic performance of the engine, and the radial engine allows incorporation of a large regenerator frontal area. Also, due to the reduced regenerator wall constraint because of the flexure arrangement (discussed in Section 3.3), a relatively short regenerator in the direction of flow is possible.

Significant changes were made in heat exchanger size between the minimum mass and maximum efficiency designs. For minimum specific mass, the heat exchanger's axial length was shortened to the minimum length at which the heater wall temperature drop equaled  $40^{\circ}\text{C}$  (considered the maximum desirable  $\Delta T$ ) or the heat-pipe heat flux exceeded the maximum limit set by the heat-pipe design. The inside diameter of the heater was set by the number of heat pipes and their arrangement. In general, the minimum mass was achieved when, for the required number of heat-pipe legs, the number of primary heat pipes was minimized. That required putting more legs per primary heat pipe, subject to the drop in efficiency with increasing heater channel length.

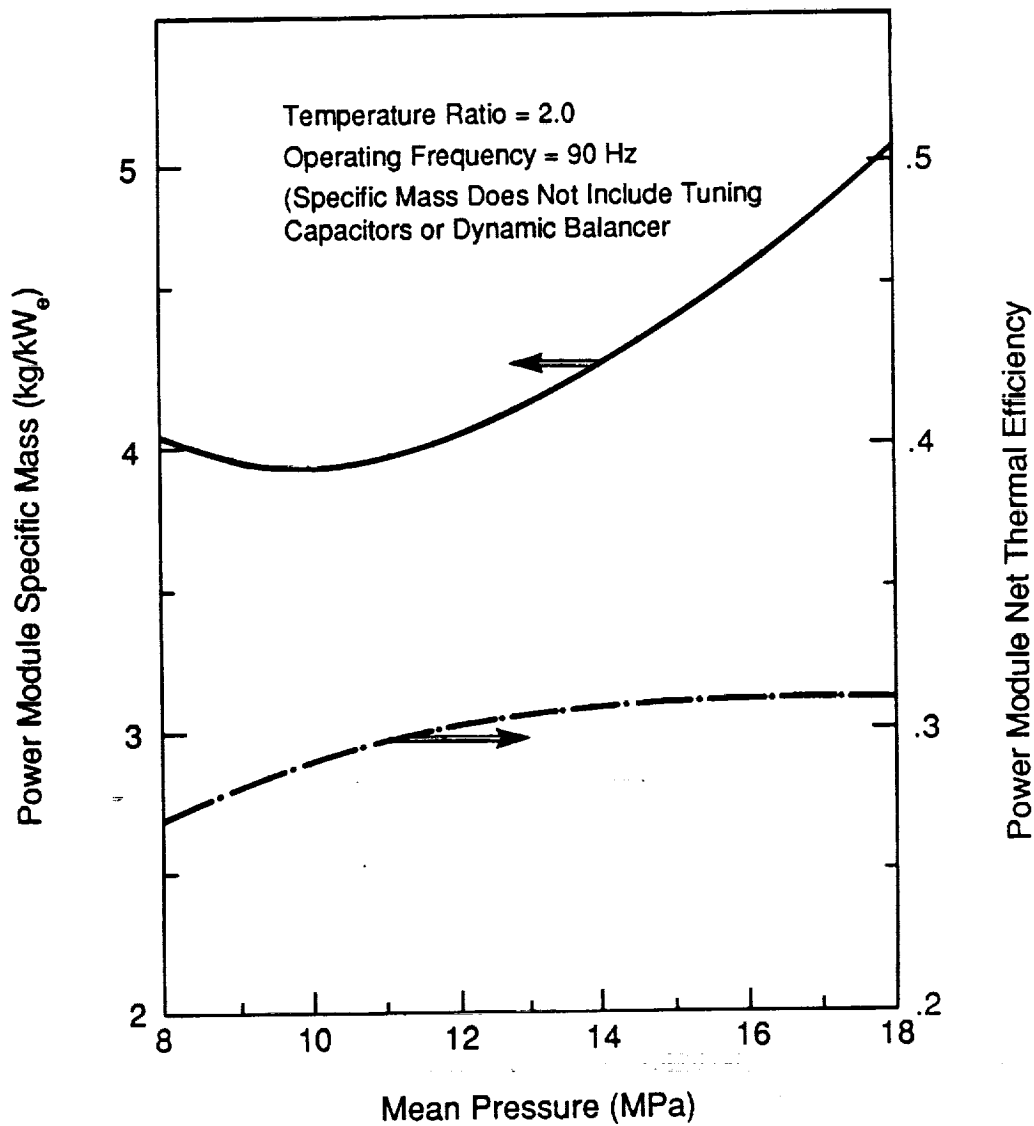
For some of the minimum specific mass designs, the mass was minimized by moving the heat exchangers up above the top of the displacer piston, thus allowing the inside diameter of the heater to be less than the displacer diameter. This reduced the outside diameter of the heat exchangers, and therefore the pressure vessel diameter. However, the length of the pressure vessel must be increased to accommodate the elevated location of the heat exchangers, and this arrangement results in lower mass only when the extra mass due to increased pressure vessel length is less than the mass savings due to reduced diameter.

For maximum efficiency, the heat exchanger axial length was increased until the rate of efficiency increase with specific mass increase ( $\Delta\eta/\Delta SM$ ) became unacceptably low.

The heat exchanger dimensions varied considerably over the temperature ratios of the study. Increasing the temperature ratio decreases the heat exchanger height, primarily because the engine thermal efficiency increases. These changes reduce the required heat flux through both the heater and cooler.

**4.2.1.3 Mean Pressure.** The effect of mean pressure on power module efficiency and specific mass was evaluated for the 150-kW<sub>e</sub> design at a frequency of 90 Hz and a temperature ratio of 2.0 (see Figure 4-4). This showed minimum specific mass occurring at 11 MPa mean pressure. The reason for the strong dependence of specific mass on mean pressure is the decoupling of the upper pressure vessel size from engine displacement, explained in the following paragraphs.

To avoid exceeding the heat pipe operating limits, the number and diameter of the heat-pipe legs in the heater are bounded by minimum values. For a given heat-pipe arrangement in the heater (for example the legs arranged radially, three deep), the minimum circle diameter is then set. For the 150-kW<sub>e</sub> base-line design, this turned out to be larger than the displacer diameter. Thus the engine displacement can be increased or decreased (within limits) without forcing a change in diameters of the heat exchangers or upper pressure vessel. For a decrease in design mean pressure, the pressure vessel thickness drops in proportion, and since the increase in displacer piston size required to maintain power does not affect heat exchanger and pressure vessel diameter (until the inner heater diameter is reached), the pressure vessel mass drops. This drop in vessel mass is partially offset by increased mass of the displacer and piston subassemblies and the cold end pressure vessel. However, as shown in Figure 4-4, the power module specific mass drops with decreasing mean pressure, reaching a minimum at 11 MPa. The drop in specific mass is accompanied by a modest drop in efficiency.



89721

Figure 4-4. Power Module Specific Mass and Efficiency versus Engine Mean Pressure

The selection of the mean pressure level at a given operating point depends on the optimization goals. For minimum specific mass, a lower pressure is selected; for maximum efficiency, a higher pressure is selected. The pressure level was manually selected for each operating point prior to the optimization. The mean pressure levels of the minimum specific mass operating points were close to 11 MPa for all power levels and temperature ratios considered in the study. Similarly, the baseline points were all designed at mean pressure levels close to 13 MPa, and the maximum efficiency points were designed at levels close to 15 MPa.

**4.2.1.4 Operating Frequency.** The main variable in going from the maximum efficiency case to the minimum mass case was operating frequency. For minimum specific mass, operating frequencies of up to 110 Hz were investigated, but efficiency fell off rapidly for frequencies greater than 90 Hz. Therefore, 90 Hz gave the minimum specific mass, a result that was relatively independent of power level and temperature ratio. All of the minimum specific mass points in the parametric study were set at 90-Hz frequency.

For maximum power module efficiency, frequency was decreased to 60 Hz. For frequencies lower than 60 Hz, the specific mass increased with little gain in efficiency. All of the maximum efficiency points in the parametric study were set at 60-Hz frequency, except for two of the 150-kW<sub>e</sub> operating points for which operating frequencies of 58 and 55 Hz were selected.

The baseline optimizations (maximum ratio of power module thermal efficiency to power module specific mass) were performed at the intermediate operating frequency of 75 Hz. The sensitivity of efficiency and specific mass to operating frequency is shown in Figure 4-5 for an early power module design (prior to final optimizations) at a power level of 150 kW<sub>e</sub> and a temperature ratio of 2.0. Power module size was adjusted for each frequency to maintain 150-kW<sub>e</sub> power level, but heat exchanger optimization was not performed.

## 4.2.2 Thermal Analysis

The objectives of the thermal analysis performed during the course of the study were as follows:

- Evaluate heat pipe and engine heater design variables and select a heat-pipe design configuration consistent with heat-pipe performance limits and engine heat input and thermal loss requirements.
- Evaluate coolant system and engine cooler design variables and select configuration consistent with thermal loss and coolant system pumping power requirements.

**4.2.2.1 Heat-Pipe Analysis.** Analysis of a heat-pipe design for the SPRE performed by Thermacore showed that heat pipes using a sintered powder metal wick and sintered arteries (Figure 4-6) can meet performance requirements in both 0-g and 1-g gravity fields with adverse inclinations. Figure 4-7 shows a plot of heat-pipe performance limits versus vapor temperature for a 22.2-mm ID heat pipe with sintered powder metal wicks and arteries and sodium working fluid. The heat-pipe orientation in the gravity field is seen to affect the performance, but the capillary limit exceeds the design target by a margin of more than two for all cases.

For this study the Argonne National Laboratory heat-pipe code (ANL/HTP) was used to predict heat-pipe performance and temperature distribution during steady-state operation. Source and sink temperatures and heat transfer coefficients can be set as boundary conditions in the code and varied for parametric studies. Viscous, sonic, entrainment, capillary, and boiling limits are calculated. Figure 4-8 shows calculated performance limits as a function of heat-pipe ID for a fine-mesh screen wick with arteries. Similar characteristics to the sintered metal wick analyzed by Thermacore were specified since the ANL/HTP

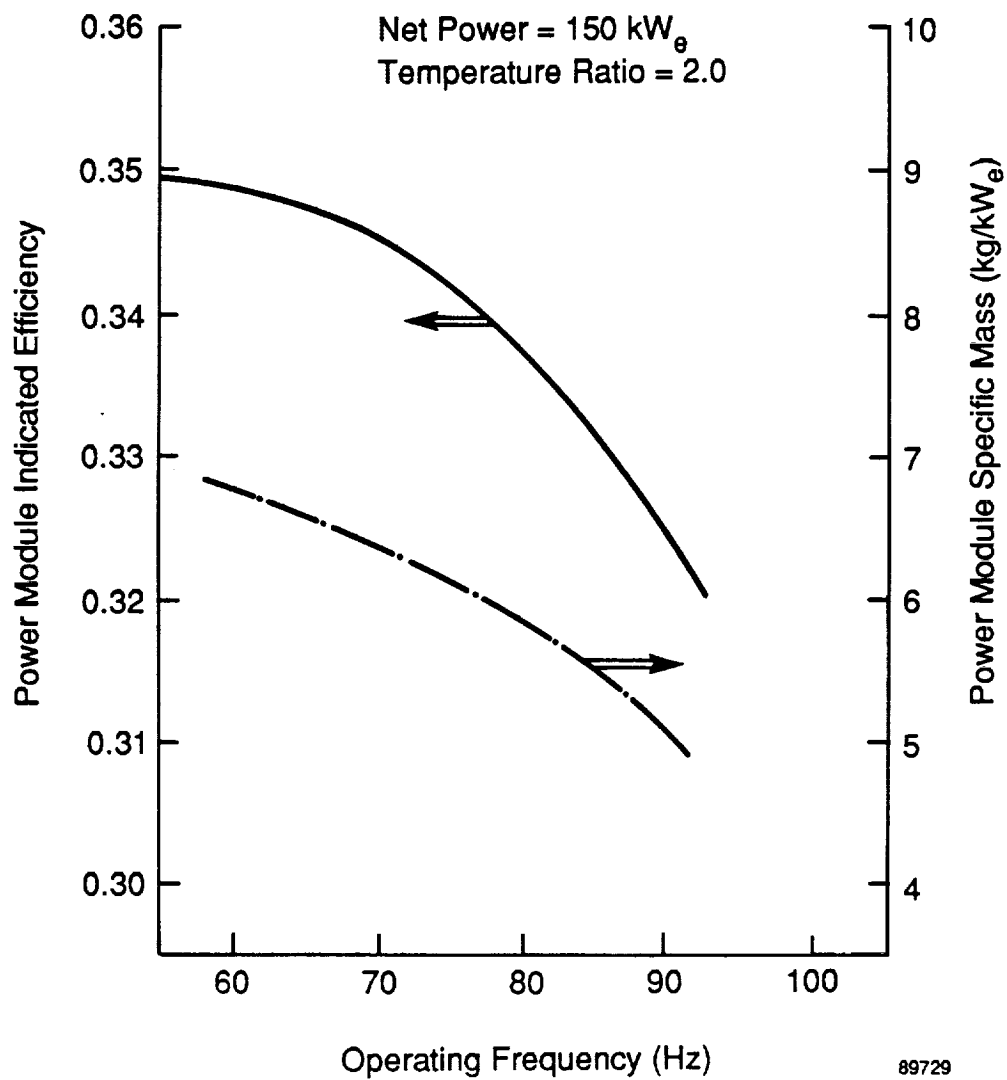
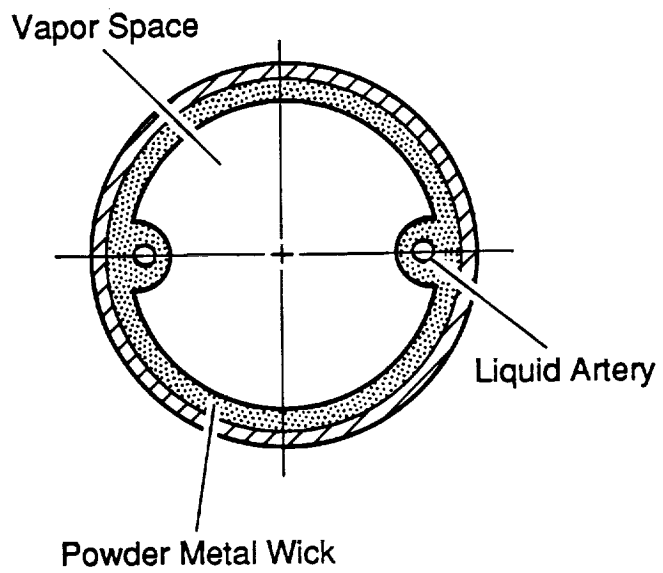


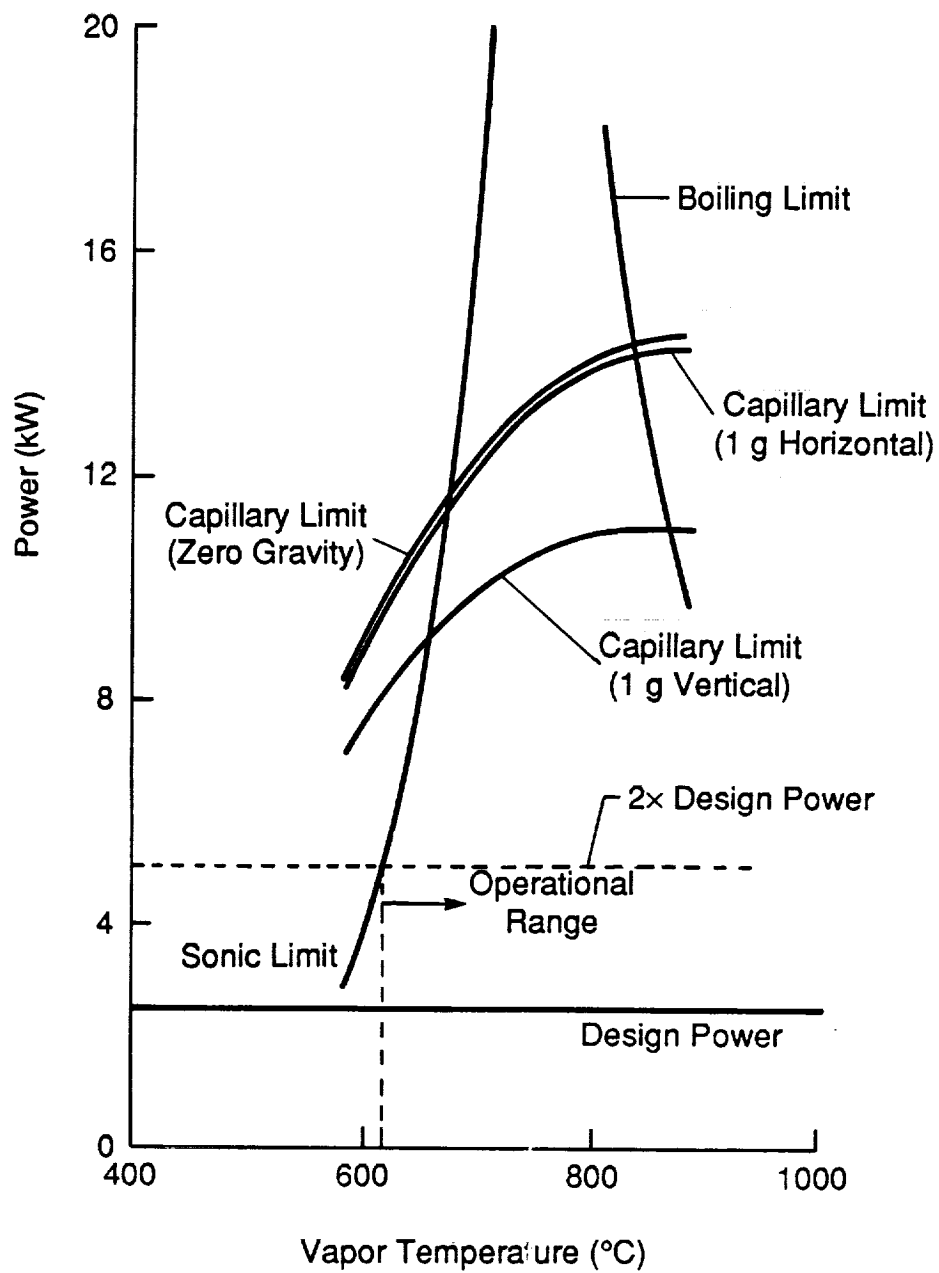
Figure 4-5. Power Module Efficiency and Specific Mass versus Operating Frequency





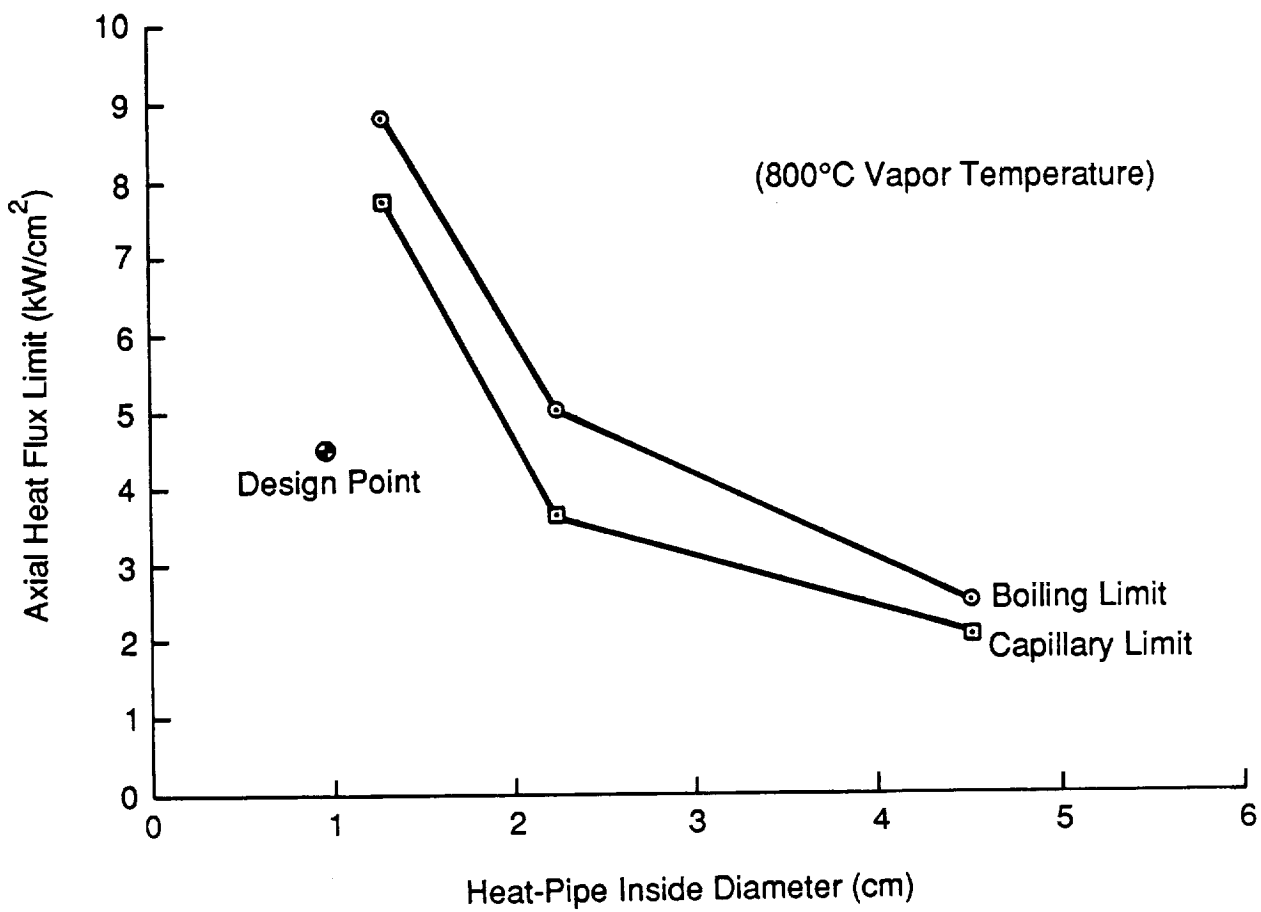
89722

Figure 4-6. Diagram of an Arterial Heat Pipe with Sintered Powder Wick and Arteries



89723

Figure 4-7. Power Transport Limits of a 2.22-cm ID Sodium Heat Pipe as a Function of Heat Pipe Vapor Temperatures



89724

Figure 4-8. Heat-Pipe Performance Limits versus Heat-Pipe Diameter

code cannot handle sintered wicks. Thermacore recommended 9.5 mm as the minimum heat-pipe ID based on manufacturing constraints for arterial heat pipes. The minimum predicted heat flux limit for this diameter heat pipe is the entrainment limit, which is close to the capillary limit. Using a heat-pipe design safety factor of 2, the 9.5-mm pipe ID is acceptable.

**4.2.2.2 Coolant System Analysis.** Selection of the NaK coolant tube diameter and NaK flow rate depends on the trade-offs between temperature drops (bulk and film), pump head, and coolant pumping power requirements. The coolant pumps are assumed to be hermetically sealed, electromagnetic pumps, which have a low efficiency and low pressure head capability. Since the coolant system power requirements do not enter into the efficiency calculations of the power module, the temperature drops were given more weight in the evaluation. The NaK mass flow rate was set to limit the bulk NaK  $\Delta T$  across the cooler to 15°C, thereby providing a fairly uniform cooler metal temperature.

Sizing of the coolant tubes involves selection of the minimum diameter (smaller diameter reduces the NaK film  $\Delta T$  and increases the cooler flow area on the helium side) without excessive pressure drop. Since the mean cooler diameter is greater than the mean heater diameter in the radial engine design, the cooler is less restricted than the heater on both the engine side (cooler frontal area) and the coolant side. Figures 4-9 through 4-12 show NaK temperature drops ( $\Delta T_{\text{bulk}} = T_{\text{out}} - T_{\text{in}}$ ;  $\Delta T_{\text{film}} = T_{\text{wall}} - T_{\text{NaK}}$ ), pressure drop (cooler core drop and estimated loop loss), and total coolant loop pumping power for the 150-kW<sub>e</sub> baseline design, as a function of NaK mass flow rate and coolant tube inside diameter. The coolant loop was undefined, and 10 velocity-heads of pressure drop were assumed for the calculations. A tube ID of 6.35 mm was selected for all design points in the study, with a maximum pump head of 35 kPa. NaK mass flow rate was scaled proportional with engine power level; the total NaK mass flow rate for the 150-kW<sub>e</sub> baseline design is 25 kg/sec.

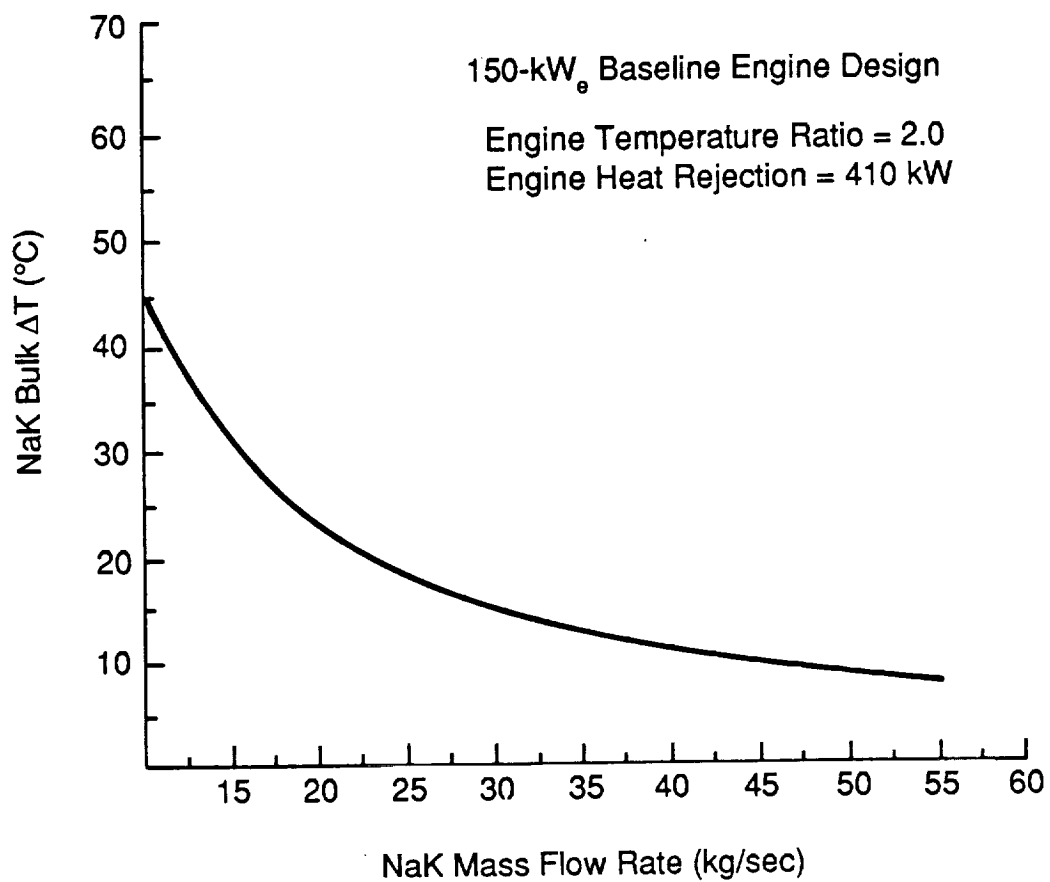
### 4.2.3 Alternator Analysis

Based on previous work performed at MTI, permanent magnet linear alternators result in higher efficiency and lower specific mass than external-wound, dc-field linear alternators.

The design of the permanent magnet linear alternator for this study was based on three levels of analysis. The first-order analysis, based on a simple model for a moving permanent magnet alternator, provided the basic alternator scaling rules and generation of the base alternator dimensions. As a check on the first-order design, a second-order MTI code (LPMMA), based on a thin gap analysis, was used for detailed alternator loss calculations on the 150-kW<sub>e</sub> baseline design at a temperature ratio of 2.0. To complete the analysis, commercial third-order finite element codes (FLUX and MAXWELL) were used to calculate structural losses and perform detailed flux mapping for the baseline design. The results of the detailed analysis were then applied to all of the design points of the study.

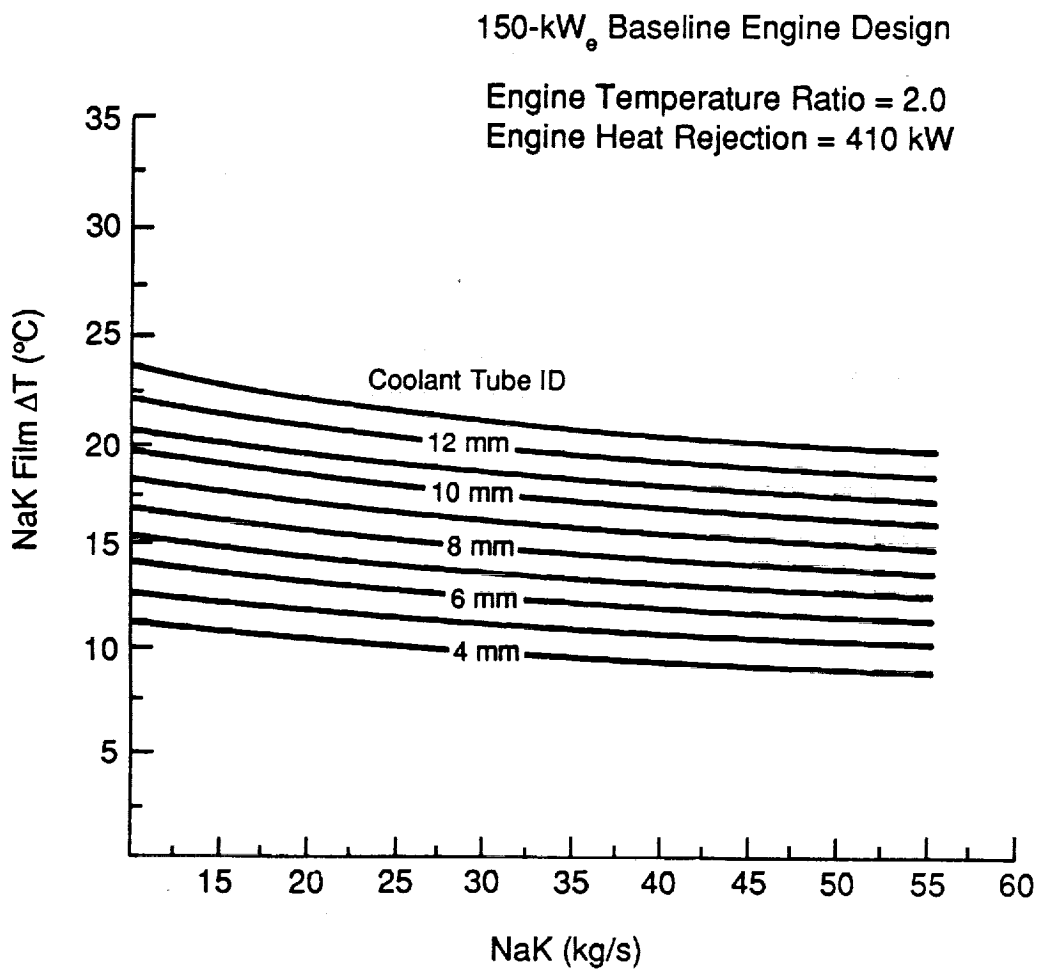
The first-order model sizes the iron and copper based on specified power level, efficiency, stroke, frequency, and plunger diameter. Prescribed values for alternator and structural eddy-current losses (calculated using finite-element codes) are used to determine the loss available for copper ( $I^2R$ ) and core losses. Constraints on the alternator sizing that were used to avoid unworkable designs are listed below:

- Minimum radial gap between inner and outer stators = 8 mm (structural)
- Magnet plunger thickness to gap ratio = 0.8 (sidepull - bearing loads)
- Plunger structural frame = 5% of plunger cross section (structural)
- Pole width = magnet width = plunger stroke (optimal performance)
- Inner stator ID = piston cylinder OD (geometry)
- Coil packing factor = 60% (insulation thickness; fabrication)



89725

Figure 4-9. NaK Bulk Temperature Drop versus NaK Mass Flow



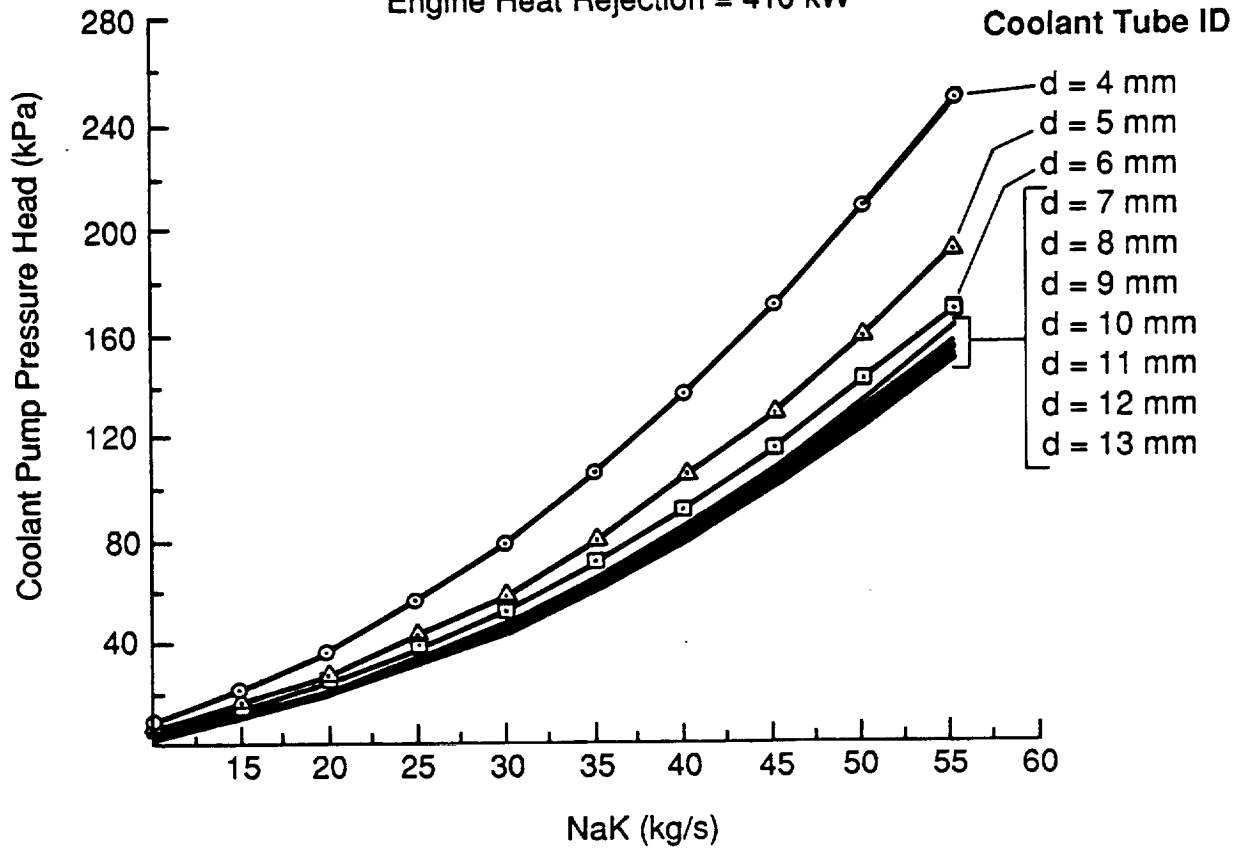
89726

Figure 4-10. NaK Film Temperature Drop versus NaK Mass Flow  
as a Function of Coolant Tube Diameter

150-kW<sub>e</sub> Baseline Engine Design

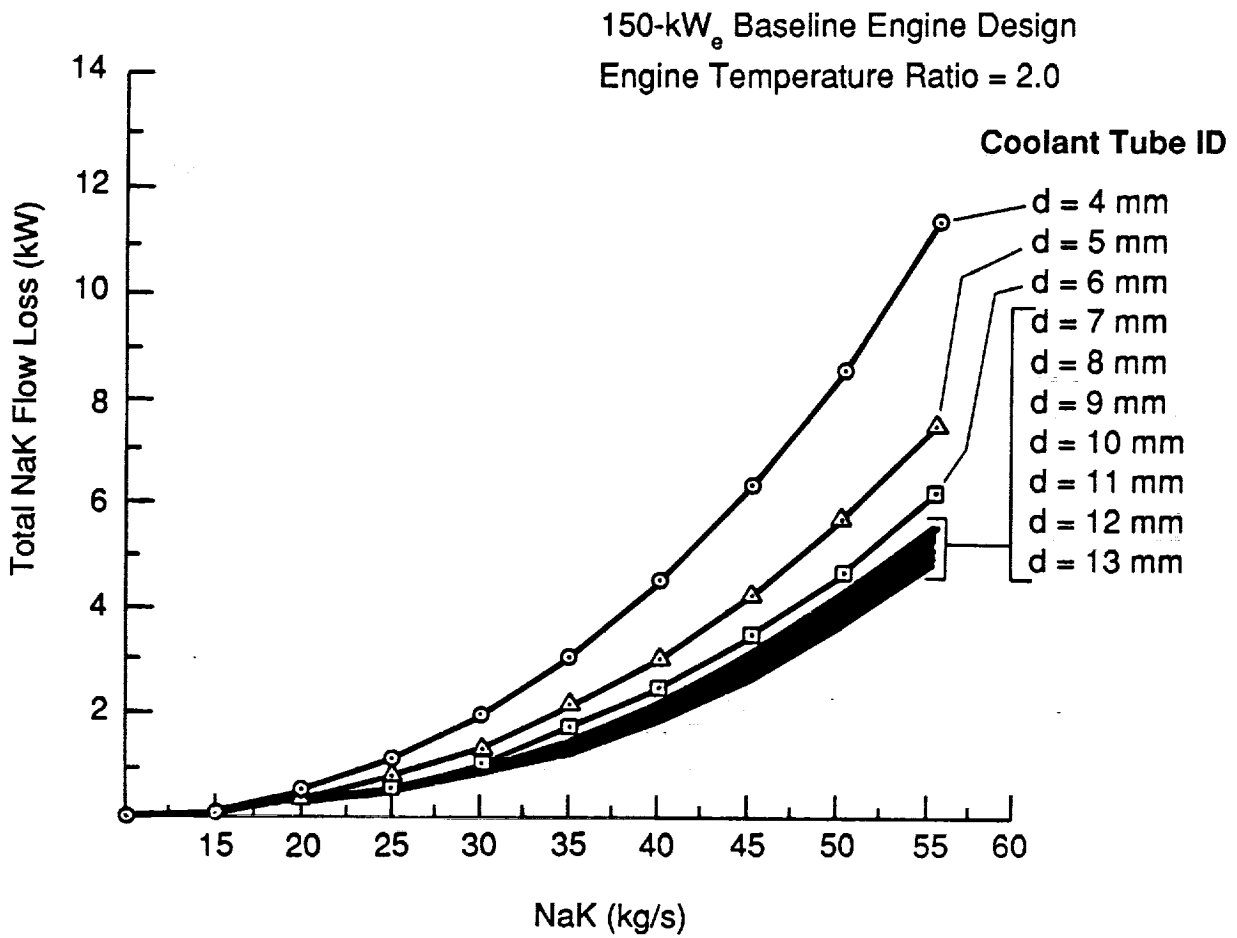
Engine Temperature Ratio = 2.0

Engine Heat Rejection = 410 kW



89772

Figure 4-11. NaK Pump Head versus Flow Rate as a Function of Coolant Tube Diameter



89727

Figure 4-12. Total NaK Flow Loss Including Entrance/Exit and Manifolds versus NaK Mass Flow as a Function of Coolant Tube Diameter



- $\beta_{\max} = 1.0$ , where  $\beta$  is the ratio of inductance voltage drop to magnet-induced voltage (selected based on power module stability criteria)
- Maximum flux density in stator laminations = 2.2 T (tesla) (saturation)
- Magnet demagnetization limit based on magnet B-H curve at temperature of  $T_{\text{Cooler}} + 50^{\circ}\text{C}$ . For temperature ratio of 1.7, alternator cooling must provide sufficient cooling to maintain magnet temperature at same temperature as for temperature ratio of 2.0 (magnet material).

The inputs to the first-order analysis are the power level, number of alternator sections, plunger stroke and diameter, operating frequency, alternator efficiency, eddy-current losses, and terminal voltage. For designs with multiple alternator sections, the coils were assumed to be electrically connected in series. The first-order design of the alternator is independent of the alternator voltage level. The alternator voltage level was selected for each power level based primarily on consideration of coil wire diameter. The number of wire turns in the coil varies proportionally with voltage level. The minimum voltage level is set by coil winding considerations (wire diameter increases with decreasing voltage; large wire is more difficult to wind). At high voltage levels corona discharge from the alternator becomes a problem, and a maximum voltage level of 1000 V was set for all designs.

Tuning capacitor size is also set by the alternator voltage level. Aluminum foil capacitors with teflon dielectric were assumed for capacitor mass calculations. The dielectric strength and voltage level determine the dielectric thickness, and the capacitor area is set by the dielectric constant, dielectric thickness, and required tuning capacitance. The foil thickness is based on trade-off between mass and efficiency ( $I^2R$  loss in the capacitor increases with decreasing foil thickness). The 25-, 75-, and 150-kW<sub>e</sub> alternator designs in the study used voltage levels of 200, 400, and 600 V, respectively. The capacitor specific mass for all designs was calculated to be 0.2 kg/kW<sub>e</sub>.

Magnet and coil eddy-current losses were prescribed to be 1% of the alternator input (shaft) power, and structural losses were set at 2%. Net alternator efficiency was set to 92% for the maximum efficiency designs, 90% for the minimum specific mass designs, and 91% for the baseline designs.

The calculated output from the first-order analysis includes

- The dimensions of the plunger, stators, and coil
- The mass of the magnets, copper, and iron
- Wire size and number of turns
- Copper and iron losses
- Current, inductance, series tuning capacitance, and capacitor mass.

The first-order analysis routine attempts to select a gap-to-stroke ratio resulting in  $\beta = 1.0$ . If the gap required to achieve  $\beta = 1$  is less than the minimum acceptable gap, then the gap is set to the minimum, and the inductance ratio falls below 1. In general, a lower  $\beta$  results in a higher alternator specific mass. However, system stability falls with increasing  $\beta$ . A good compromise between performance, stability, and specific mass is achieved with  $\beta = 1$ , so this was selected as the maximum acceptable inductance level.

The prescribed loss values used in the first-order alternator analysis were backed up with the second-order and third-order analyses. Table 4-1 shows LPMMA code calculations for the basic alternator losses of the 150-kW<sub>e</sub> baseline design at a temperature ratio of 2.0. The losses match the first-order calculations very closely. The coil  $I^2R$  loss is identical to the first-order calculated coil loss. The alternator eddy losses are 1.1% (versus 1% prescribed). The stator hysteresis loss is 0.6% (versus 0.5% from the first-order calculation).

Table 4-1. Results of Second-Order Alternator Analysis Using LPMMA Computer Program  
(150 kW<sub>e</sub>, Three-Section Baseline Alternator; Engine Temperature Ratio = 2.0)

- Calculated Alternator Loss Breakdown:

<u>Alternator Component</u>	<u>Loss Per Alternator Section (W)</u>
Coil	
— I <sup>2</sup> R	3033.0
— Eddy Current	243.0
Magnets	
— Hysteresis	19.0
— Eddy Current	347.0
Stators	
— Hysteresis	314.0
— Eddy Current	27.0
Total	3983.0

- Calculated Alternator Efficiency = 92.8% (Excluding Structural Losses)

Table 4-2 shows the third-order code calculations made with the commercial code FLUX for the structural losses of the 150-kW<sub>e</sub> baseline design at a temperature ratio of 2.0. Structural losses are calculated for the piston cylinder and alternator support cylinder. The outer pressure vessel was not included in the analysis since it is made of nonmagnetic material and there is a relatively large gap between it and the outer stator. The total calculated structural loss is very low (0.1% versus 2% assumed), but is probably significantly under-predicted since the finite-element grid used for the calculation was too coarse. Due to the financial limitations of this study, additional runs with reduced mesh size could not be made. However, it is expected that structural losses will not exceed the 2% allocated.

Third-order analysis made with the commercial code MAXWELL was used to generate detailed magnetic flux maps and to calculate flux distribution in various locations of the alternator. Two coil sections of the three-section, 150-kW<sub>e</sub> baseline alternator design at a temperature ratio of 2.0 were analyzed to check for interactions between adjacent sections.

The flux distribution was first calculated at the maximum stroke position of the plunger (all the way in, toward the engine compression space) with no coil current. Figure 4-13 shows the flux distribution in the two alternator sections that were analyzed. For this case the top magnet ring of each section was completely outside the gap, while the third magnet ring was located directly under the coil slot. The second and fourth magnets drive the flux counterclockwise around the coil. The radial flux density in the gap as a function of axial position along the plunger is plotted in Figure 4-14, with zero position corresponding to the upper end of the top magnet. The coordinate system is defined such that positive flux is to the right in Figure 4-13. As seen from the closer spacing of the flux lines on the lower pole of each section, the flux density is higher there than under the upper poles because of the flux leakage across the slot and down to the magnet under the slot. The flux density values are approximately 21% lower across the upper pole faces because of the leakage.

Figure 4-15 shows the radial flux density as a function of axial position along a line parallel with the plunger, cutting the outer stator at the point of minimum iron cross section, just beyond the top of the pole "shoe." The flux densities are higher than at the pole faces because of less iron area. The upper and lower poles have nearly equal flux levels (1.24 T versus 1.28 T) at this location since there is very little flux leakage from the stator arm on the outside of the coil.

The axial flux density across the center of each section analyzed is shown in Figures 4-16 and 4-17. The inner and outer stators have nearly equal flux densities, with very little difference between alternator sections, indicating little interaction.

The second case analyzed was with the plunger at midstroke position with full design-point coil current. The calculated flux distribution for this case is shown in Figure 4-18. The first and third magnets oppose the current-induced flux, resulting in the skewed flux lines. Since the lower half of the second magnet is under the slot and not the pole face, there is a significant flux leakage across the corner of the slot. Figure 4-19 shows the radial flux density in the gap along the plunger, indicating fairly even flux densities across the upper and lower pole faces and similar results for the top and bottom alternator sections.

Figure 4-20 shows the radial flux density as a function of axial position along a line parallel with the plunger, again cutting the outer stator at the point of minimum iron cross section. The flux densities are higher than for the first case (maximum stroke plunger position), indicating that the current-induced flux is greater than the magnet-induced flux, but the flux densities are below the iron saturation level.\*

---

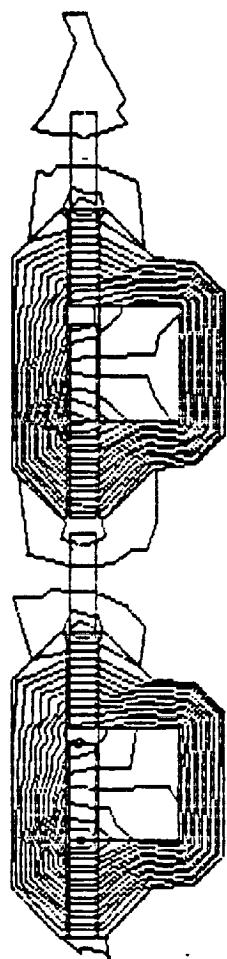
\*Vanadium Permedur (Hyperco-50), the assumed lamination material, saturates at a flux level of approximately 2.4 T. For design purposes, a limit of 2.2 T was selected.

Table 4-2. Results of Third-Order Alternator Analysis Using Flux Computer Program  
(150 kW<sub>e</sub>, Three-Section Baseline Alternator; Engine Temperature Ratio = 2.0)

- Maximum Flux Density in Stator = 2.1 T
- Calculated Structural Eddy-Current Losses (Total Alternator):

<u>Component</u>	<u>Loss (W)</u>
Piston Cylinder	98.0
Alternator Support	62.0
Total	160.0

- Net Alternator Efficiency = 92.7% (Including LPMMA Calculated Alternator Losses)
- First-Order Analysis Efficiency = 91%
- Calculated structural eddy-current losses are based on limited finite-element analysis. Additional analysis is recommended.



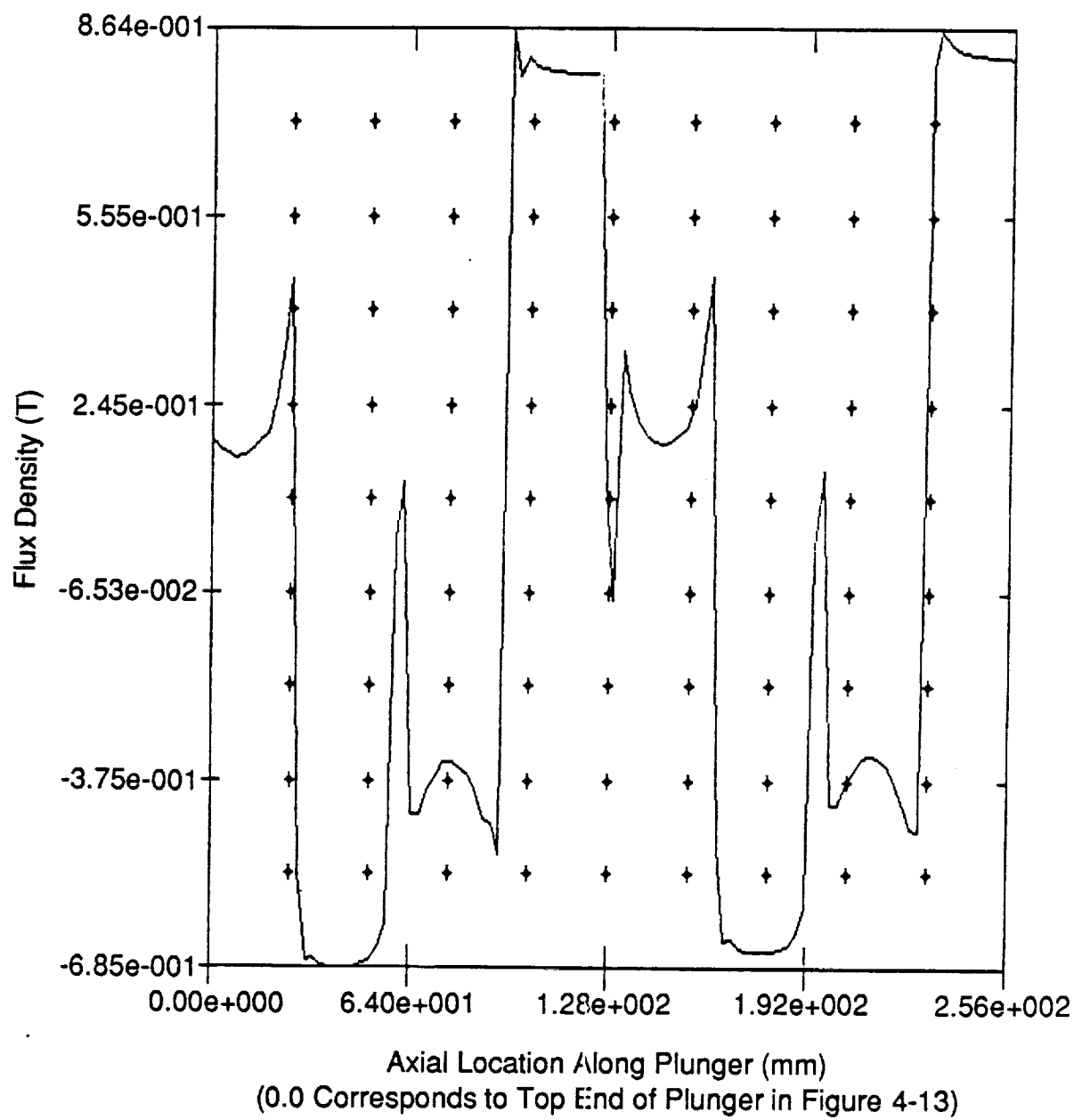
Segment No. 1

Segment No. 2

Flux Distribution: Plunger at Maximum Amplitude, No Current

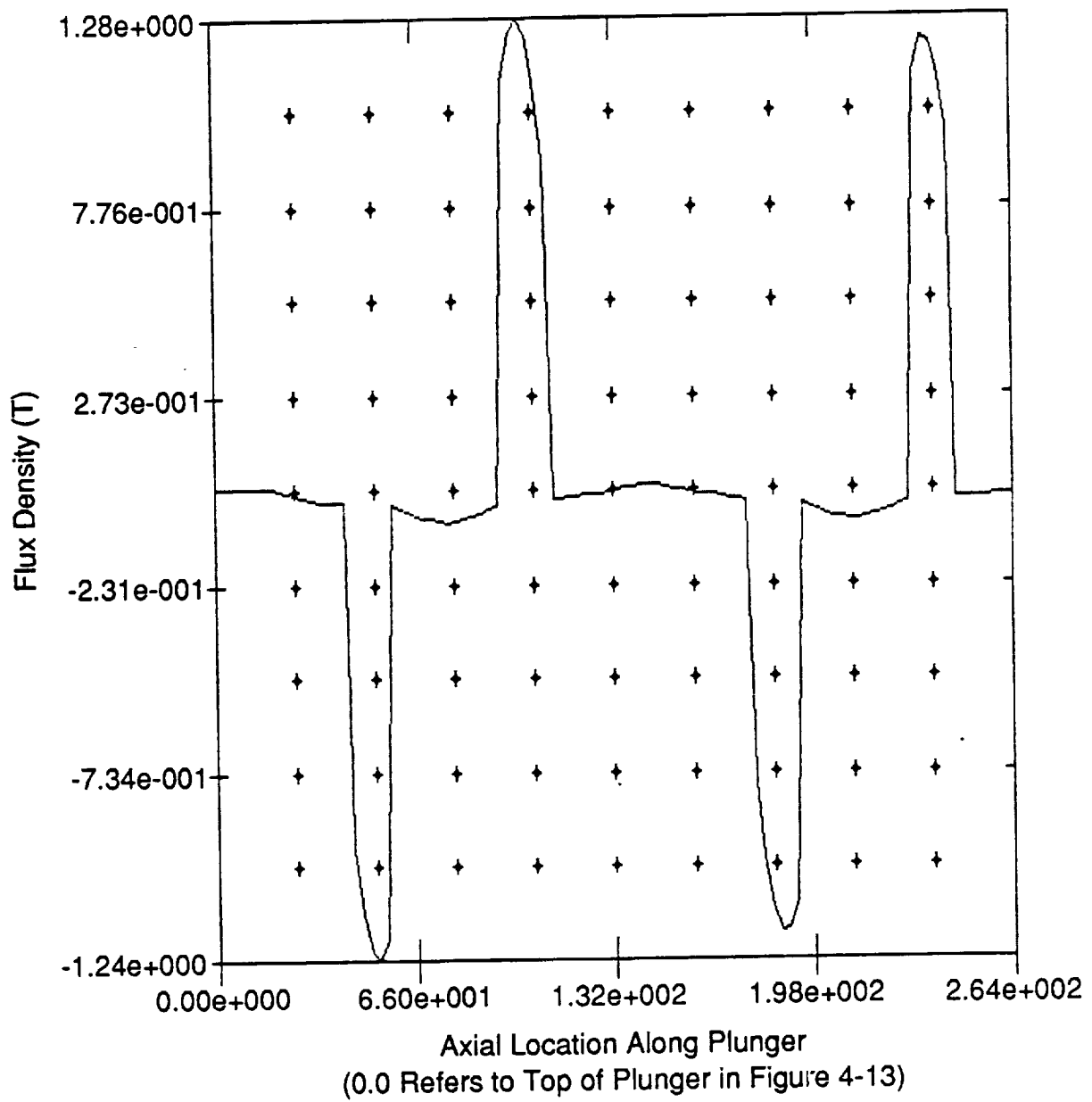
89751

Figure 4-13. 150-kW<sub>e</sub> Baseline Alternator (Two Coil Sections of Three-Section Alternator Assembly)



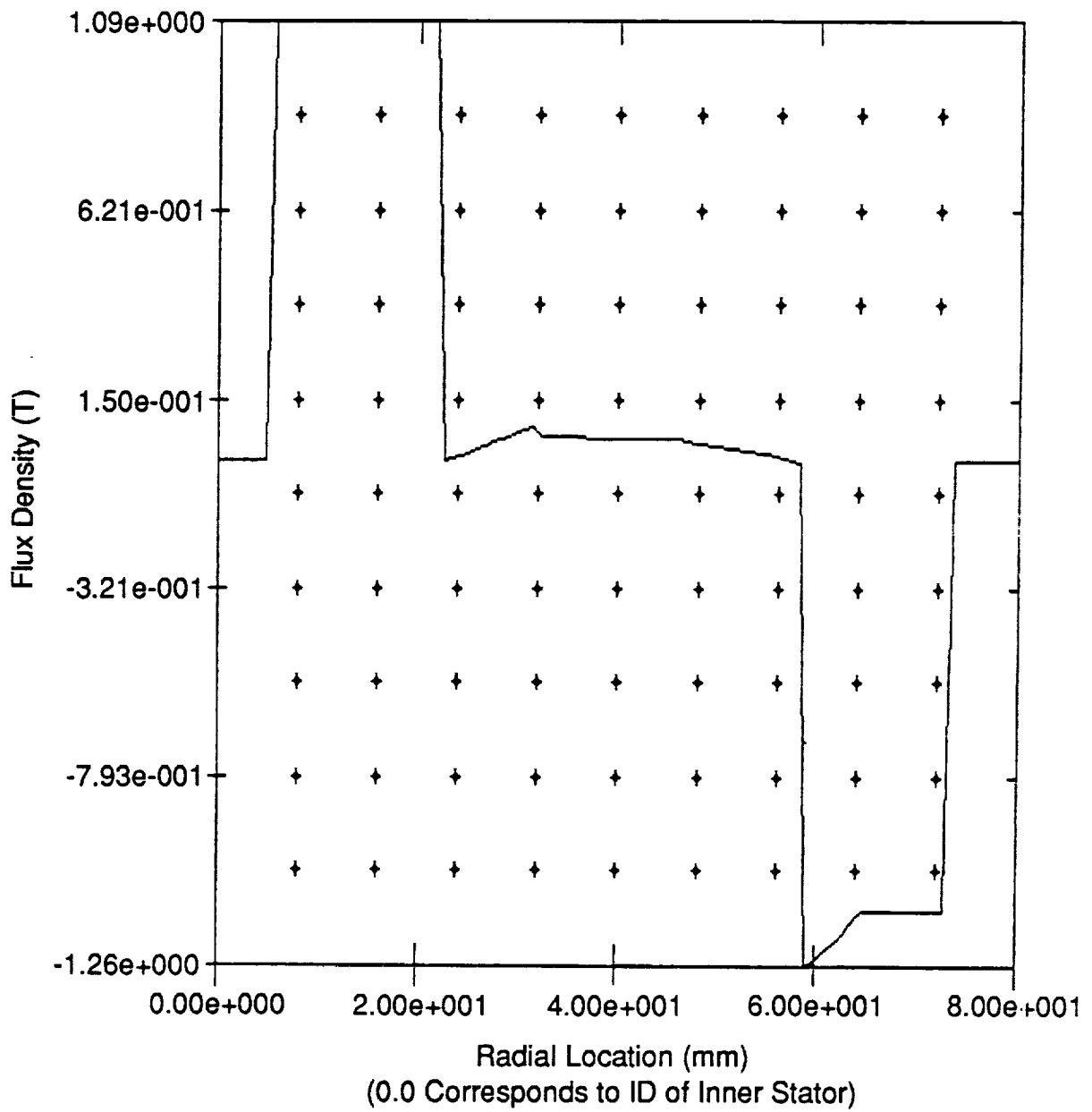
89752

Figure 4-14. Radial Flux Density in Gap versus Axial Position  
(Plunger at Maximum Amplitude, No Coil Current)



89753

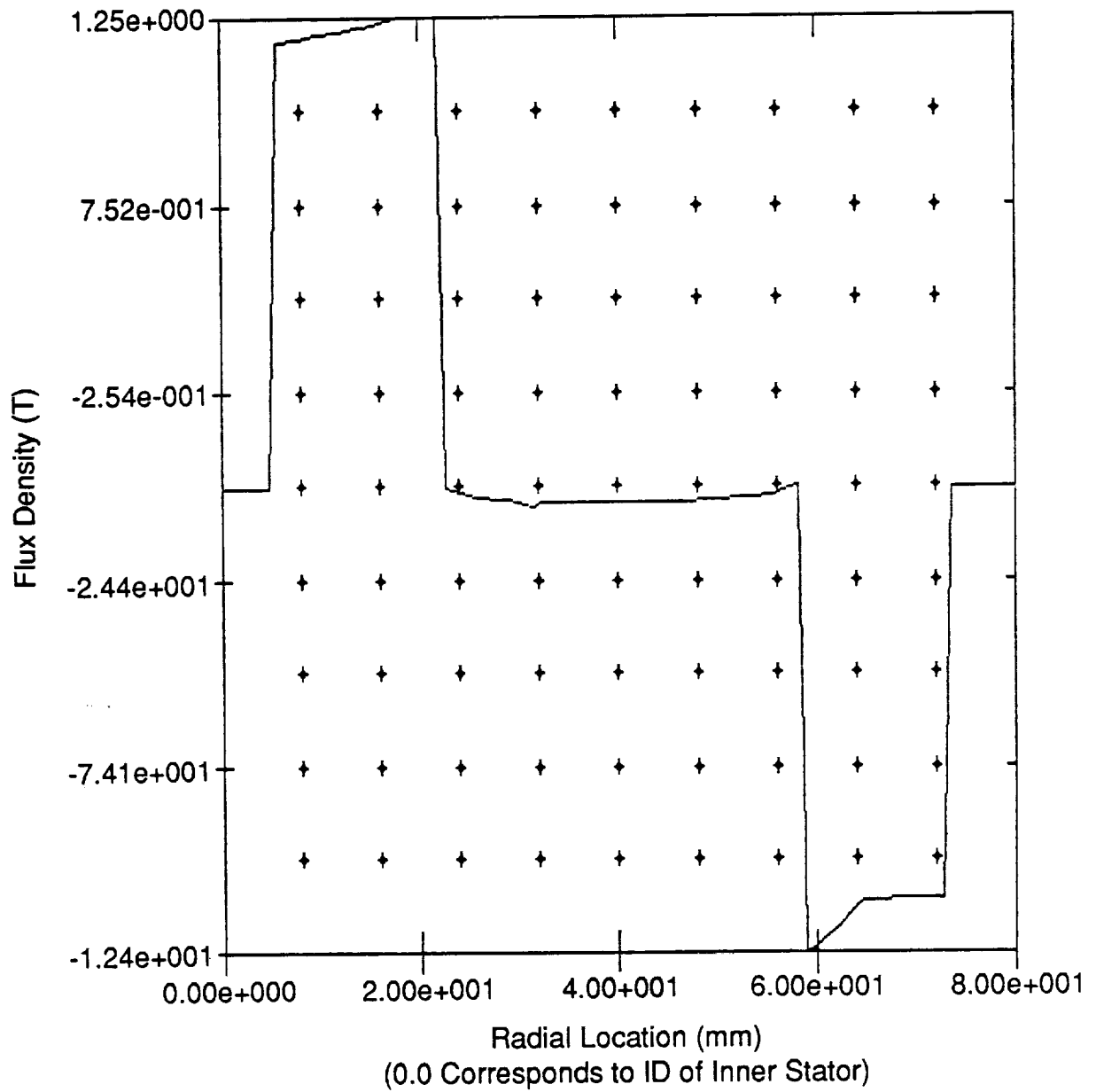
Figure 4-15. Radial Flux Density Outside of Coil versus Axial Position  
(Plunger at Maximum Amplitude, No Coil, Current)



89754

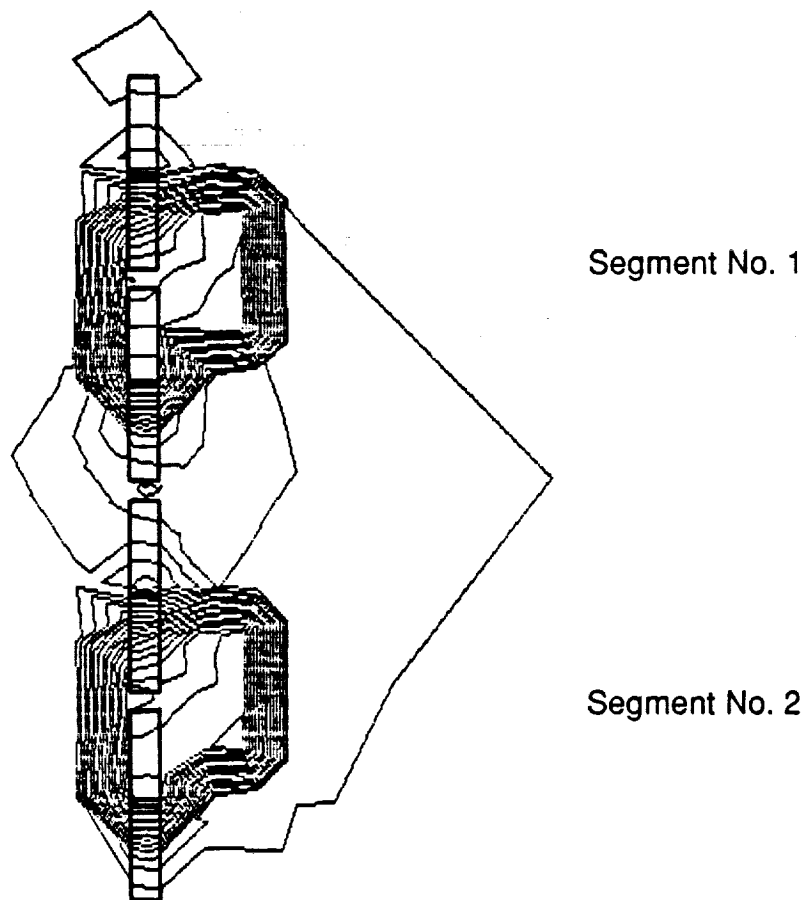
Figure 4-16. Axial Flux Density Across Segment No. 1 Center versus Radial Position





89755

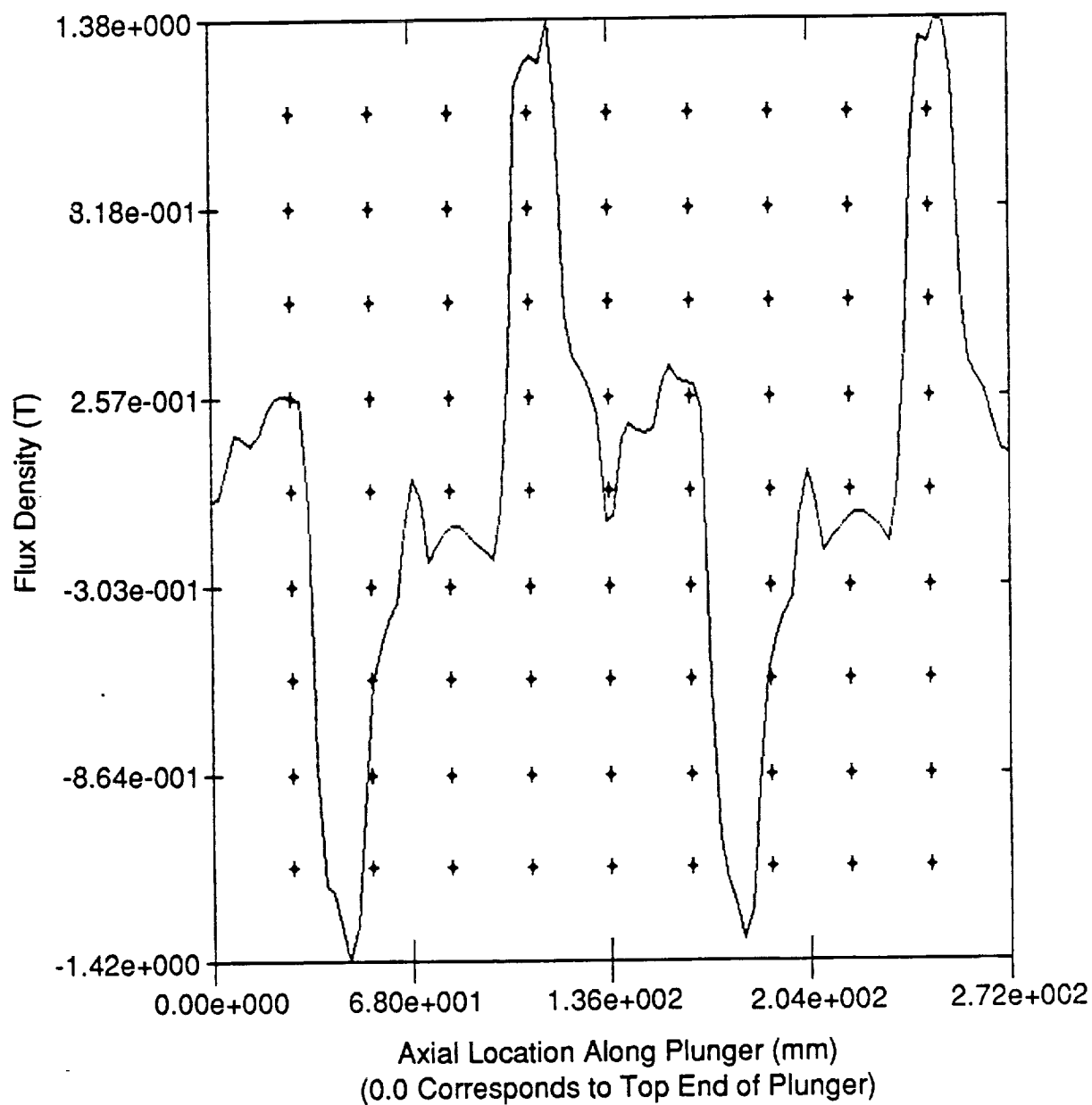
Figure 4-17. Axial Flux Density Across Segment No. 2 Center versus Radial Position



Flux Distribution: Plunger at Center Position, Maximum Current

89756

Figure 4-18. 150-kW<sub>e</sub> Baseline Alternator (Two Coil Sections of Three-Section Alternator Assembly)



89757

Figure 4-19. Radial Flux Density in Gap versus Axial Position  
(Plunger at Center Position, Maximum Coil Current)

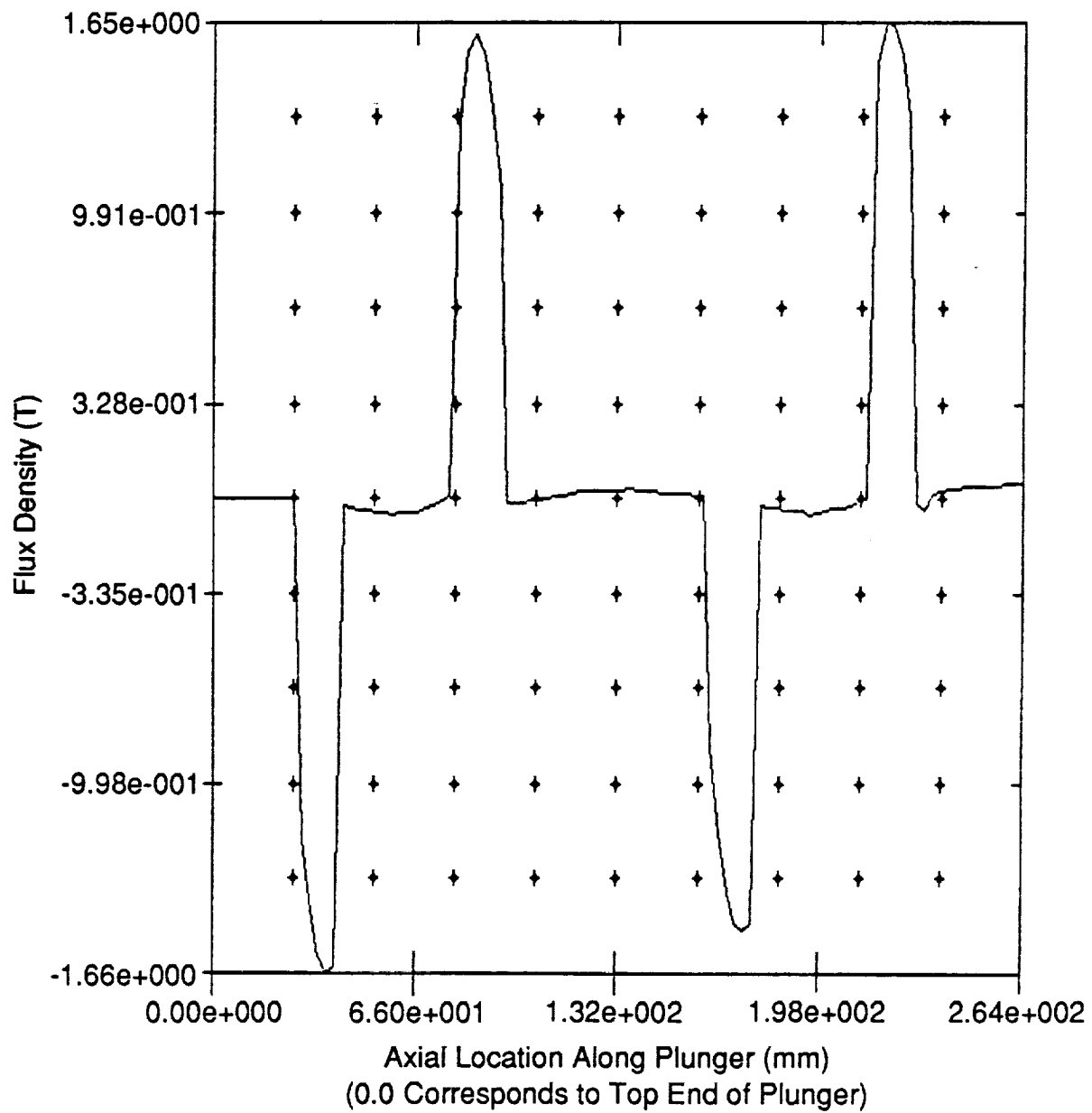


Figure 4-20. Radial Flux Density Outside of Coil versus Axial Position

89758

The axial flux density across the center of each section analyzed, shown in Figures 4-21 and 4-22, is only slightly higher in the upper alternator section due to the flux leakage between sections, indicating that the use of multiple alternator sections does not change alternator performance significantly.

The case of maximum flux occurs at a plunger position between the midstroke and end-of-stroke plunger positions analyzed above. The current-induced flux leads the magnet-induced flux by  $90^\circ$  ( $1/4$  cycle). The plunger position where flux is a maximum depends on the relative magnitudes of the magnet and coil fluxes. For the 150-kW<sub>e</sub> baseline case analyzed, the maximum flux in the gap occurs when the plunger is at 88% of full displacement, with 48% of full current in the coil. The maximum flux in the outer stator occurs when the plunger is at 63% of full displacement, with 77% of full current in the coil. Since saturation of the stator laminations is of primary concern, the maximum stator flux case was analyzed. Figure 4-23 shows the flux distribution for this case, with the radial flux density in the outer stator at the minimum iron cross section plotted in Figure 4-24. The maximum flux density of 2.1 T is less than the lamination saturation limit of 2.4 T.

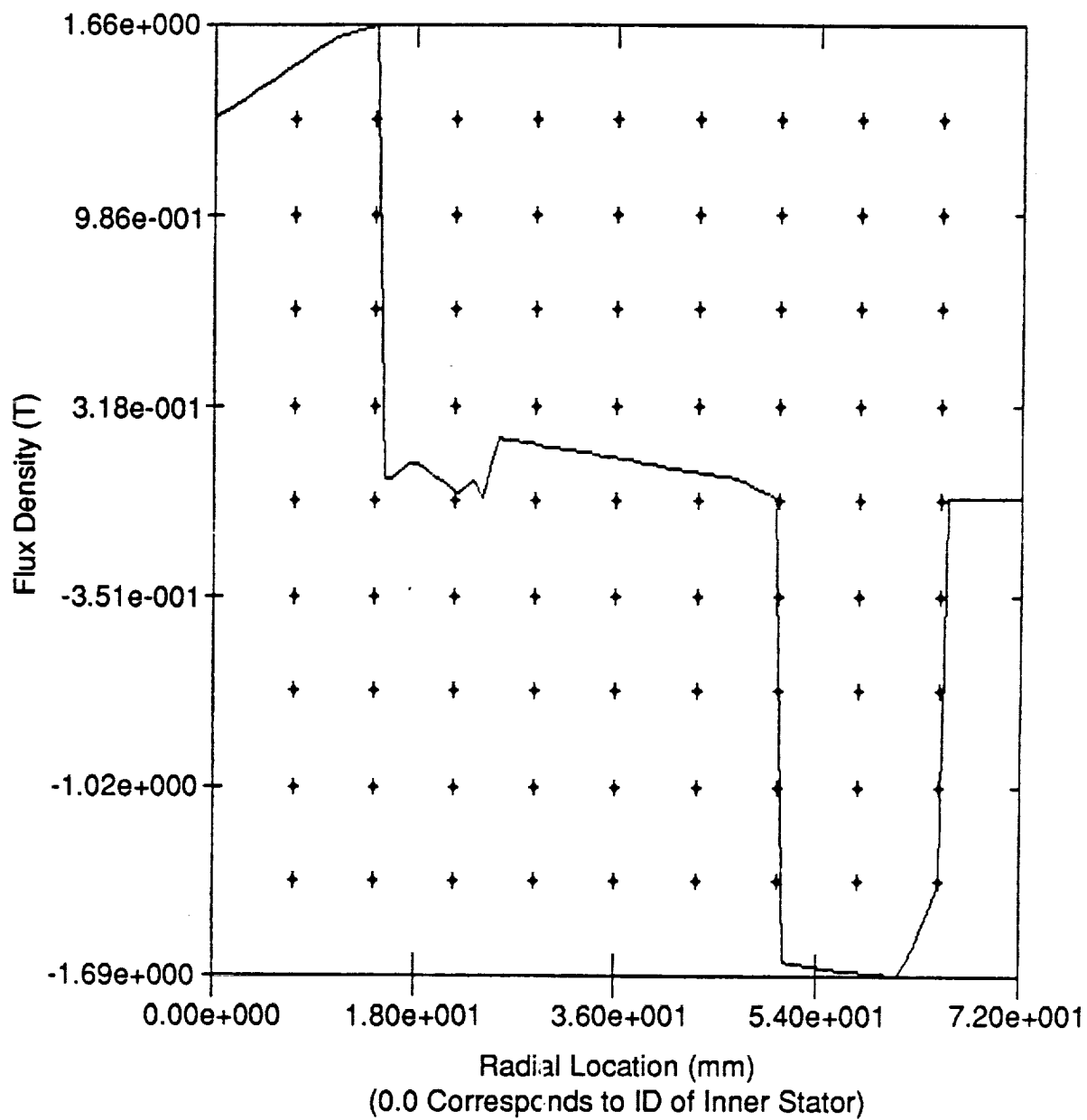
#### 4.2.4 Dynamic Balancer Analysis

Since the power module specifications call for a single-cylinder engine, a dynamic balancer system is required to achieve the specified casing vibration amplitude of less than 0.038 mm. For an ideal spring-mass balance system with no losses, the system can be tuned to cancel the piston dynamic forces with zero resultant casing motion. However, with a real balance system the losses in the balancer gas springs result in a residual casing vibration that cannot be balanced. Figure 4-25 presents the analytic model of the dynamic balancer and the equation giving casing vibration amplitude as a function of engine and balancer parameters. Figure 4-26 plots casing vibration amplitude as a function of balancer loss for the 150-kW<sub>e</sub> baseline engine at a temperature ratio of 2.0 (frequency = 75 Hz). As shown, in order to meet the vibration requirements the balance system losses must be less than 2.5 kW. For the 150-kW<sub>e</sub> power module, this corresponds to a balancer efficiency of 98.5%.

The balancer configuration considered for this study consists of a balance mass sprung to the engine casing. A structurally cleaner arrangement would use the balance mass sprung to the power piston, but this arrangement would not balance the displacer inertia and the net casing vibration would be excessive. Two opposing gas springs are used for the balance mass, separated by a clearance seal. The seal clearance was assumed to follow the same limitations as the engine seals, with clearance increasing with increasing diameter for diameters above 152 mm. The balancer gas was assumed to be helium to avoid the requirements for isolation of the balancer gas from the engine gas, and thus the increased control system complexity.

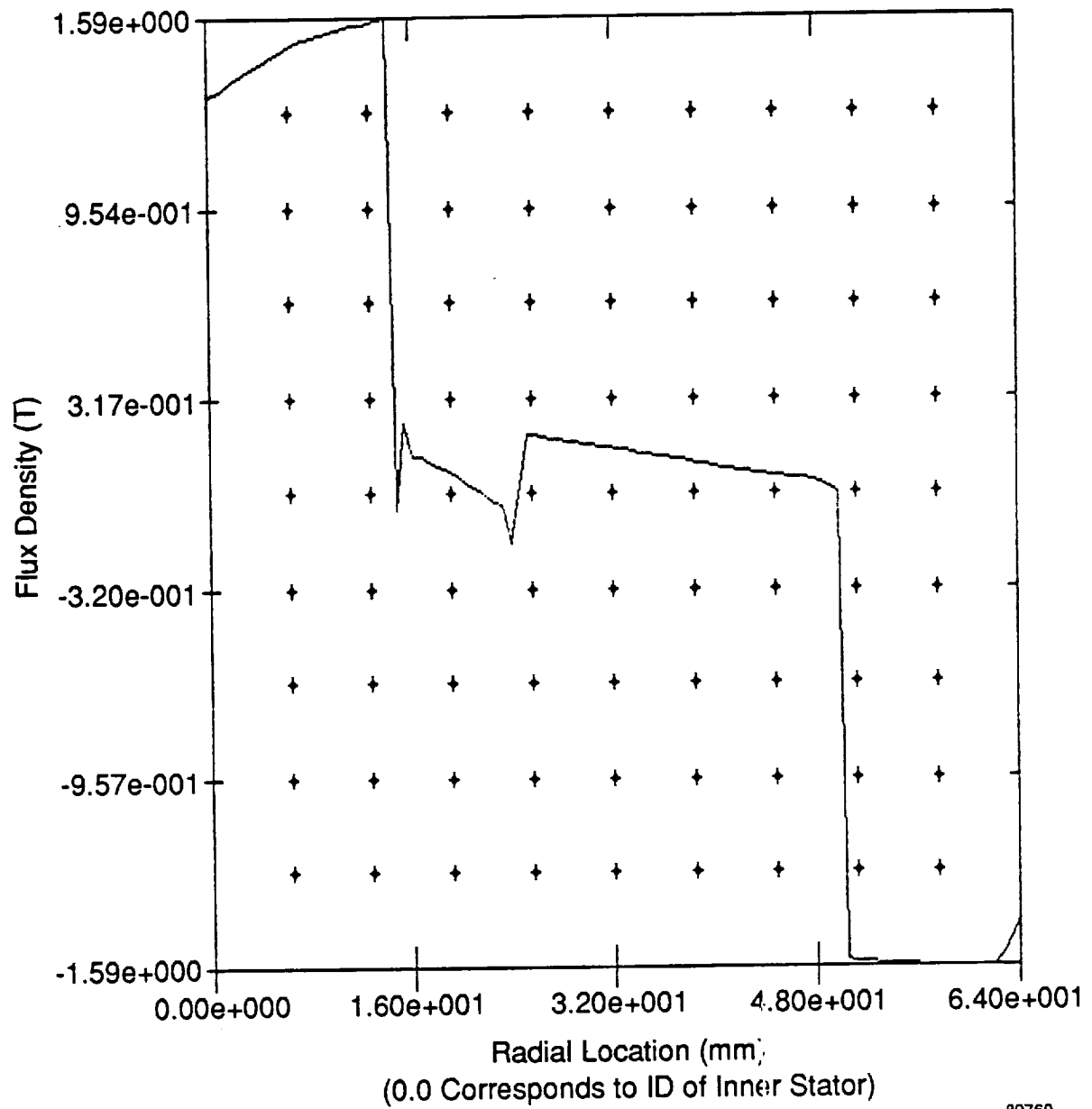
A breakdown of balancer losses and balance assembly specific mass is given in Table 4-3 for the 150-kW<sub>e</sub> baseline power module at a temperature ratio of 2.0. The gas spring losses are evenly divided between hysteresis and leakage losses. The balancer assembly mass is mostly (78%) in the moving mass, with 6% in the balance cylinder, gas springs, and support cylinder, and 16% in the extra cold-end pressure vessel required to enclose the assembly. The balancer assembly specific mass is shown in Figure 4-27 as a function of required casing vibration amplitude. The assembly mass at the vibration limit is quite high and represents approximately 25% of the total power module mass.

The balancer losses and mass can be significantly reduced by using a gas such as Freon, which has a lower specific heat ratio and thermal conductivity compared to helium. However, Freon was not considered for this study due to questions concerning system complexity.



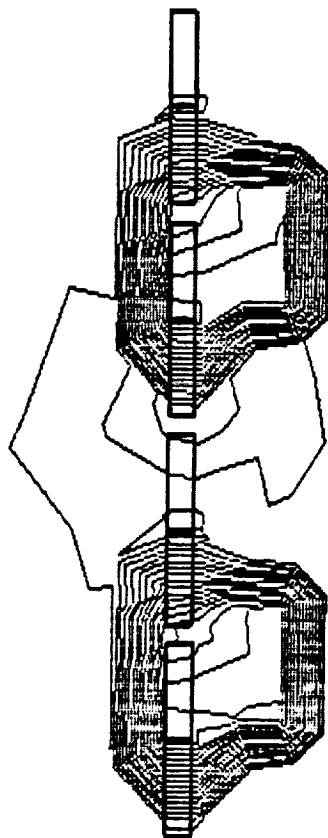
89759

Figure 4-21. Axial Flux Density Across Segment No. 1 Center versus Radial Position



89760

Figure 4-22. Axial Flux Density Across Segment No. 2 Center versus Radial Position

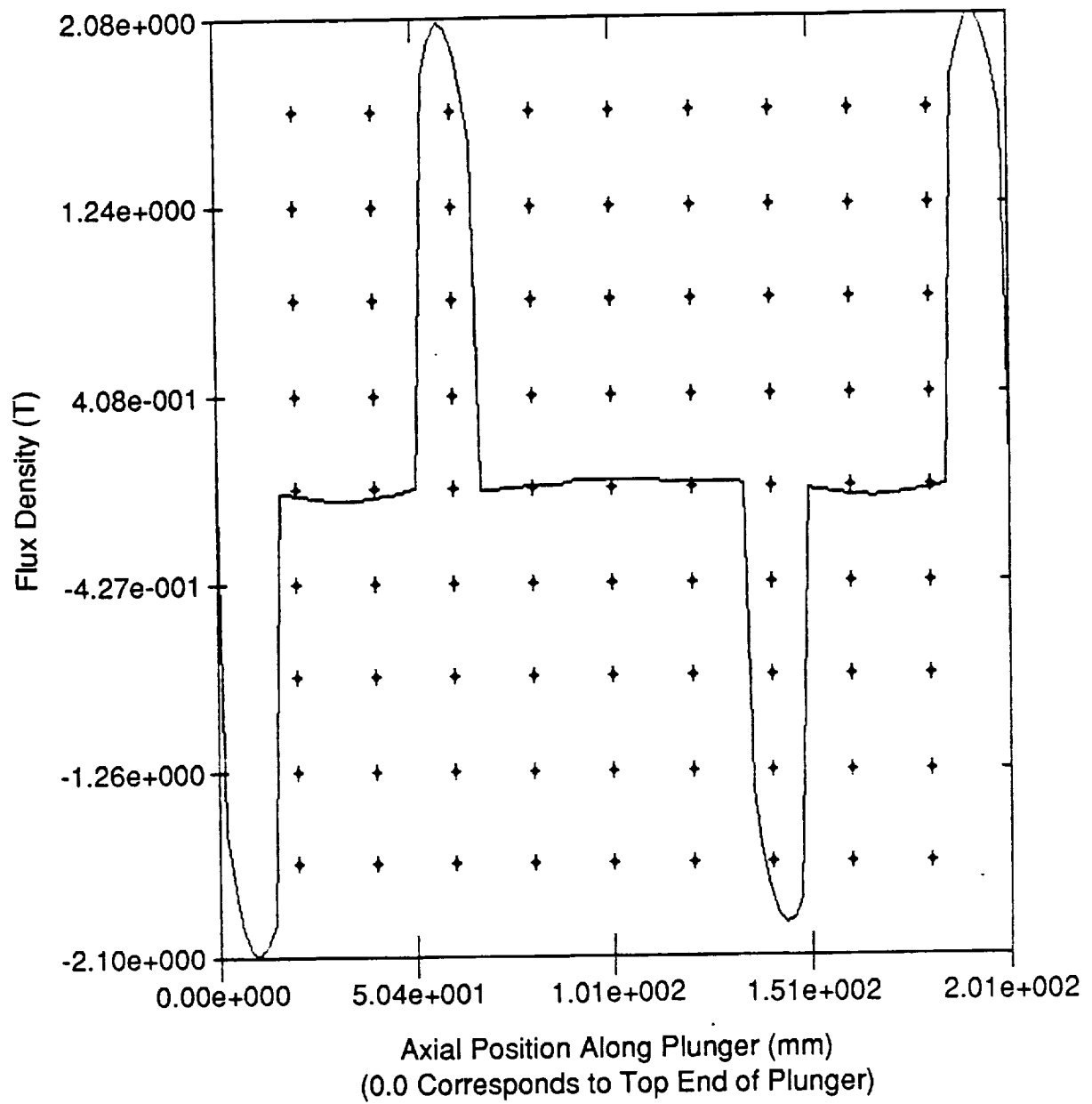


Flux Distribution: Plunger at Position of Maximum Stator Flux Density

Figure 4-23. 150-kW<sub>e</sub> Alternator (Two Coil Sections of Three-Section Alternator Assembly)

89762

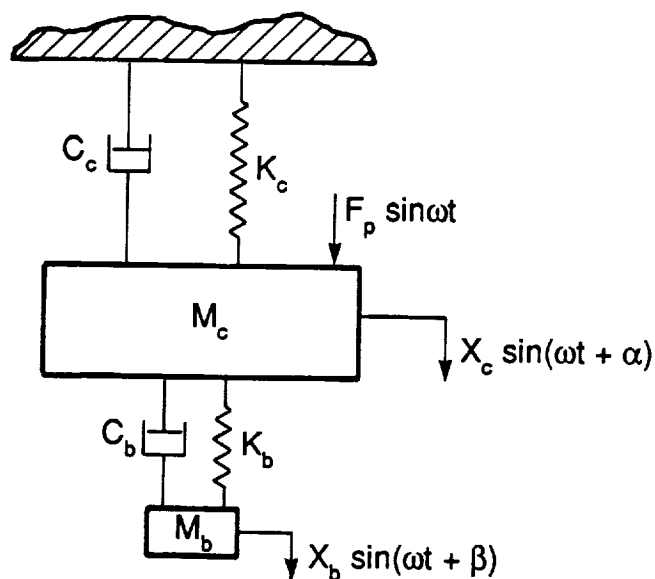




89761

Figure 4-24. Plunger at Position of Maximum Stator Flux Density - Radial Flux Density in Outer Stator versus Axial Location

### Dynamic Balancer Model



### Balance Unit Dynamic Equation

Casing Vibration Amplitude Given by:

$$(X_c/X_p)^2 = \frac{(M_p/M_b)^2 [(\Delta K_b/K_b)^2 + 4 \times \zeta^2]}{[(1 + \Delta K_b/K_b \times M_c/M_b)^2 + 4 \times \zeta^2 \times ((M_c + M_b)/M_b)^2]}$$

where:

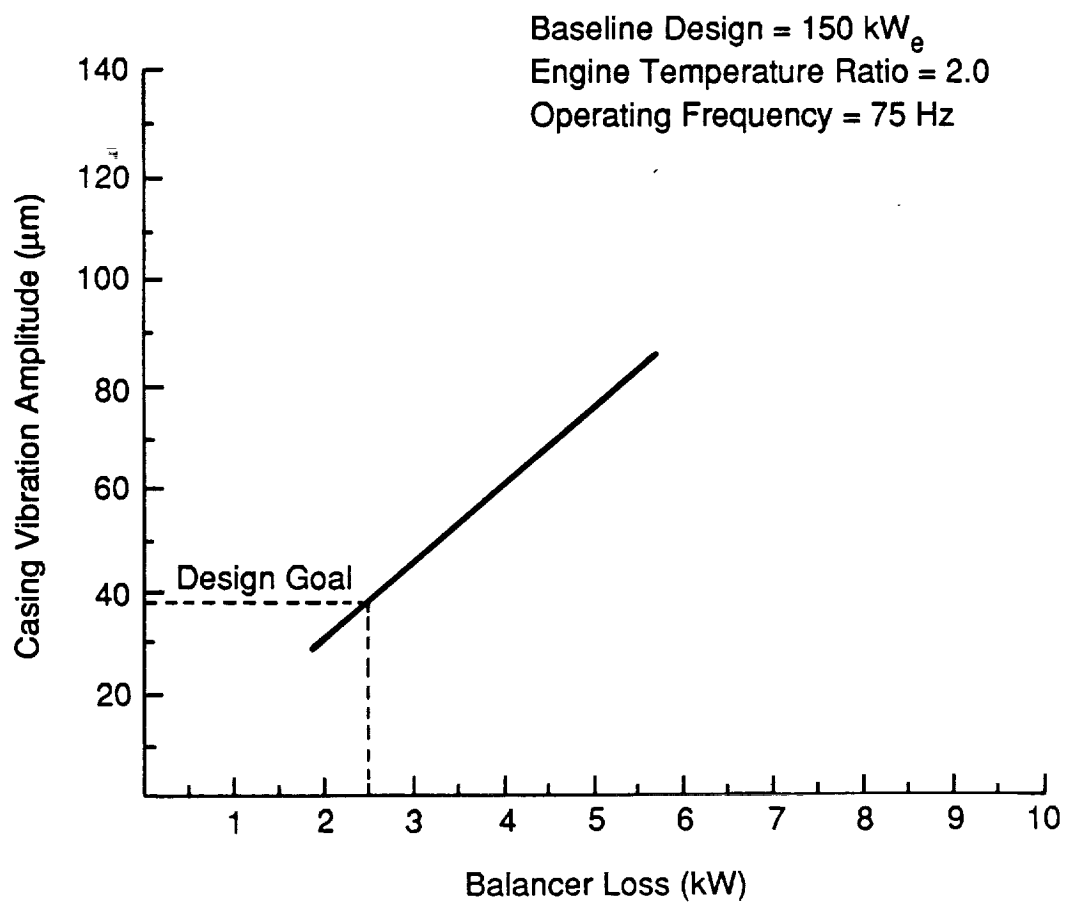
- $\zeta$  = Damping Ratio =  $C_b/(2 \times M_b \times \omega)$
- $\Delta K_b$  = Balancer Mistuning =  $K_b - M_b \omega^2$
- $M_c$  = Casing Mass
- $M_b$  = Balance Mass
- $M_p$  = Engine Piston/Plunger Mass
- $X_c$  = Casing Amplitude
- $X_p$  = Power Piston Amplitude
- $K_b$  = Balance Gas Spring Stiffness
- $C_b$  = Balance Gas Spring Damping
- $\omega$  = Engine Frequency

For  $\Delta K_b \equiv 0.0$  and  $\zeta \ll 1.0$ , Equation Reduces to:

$$(X_c/X_p)^2 = (M_p/M_b)^2 [(\Delta K_b/K_b)^2 + 4 \times \zeta^2]$$

89750

Figure 4-25. Dynamic Balancer Analytical Model and Governing Equation



891024

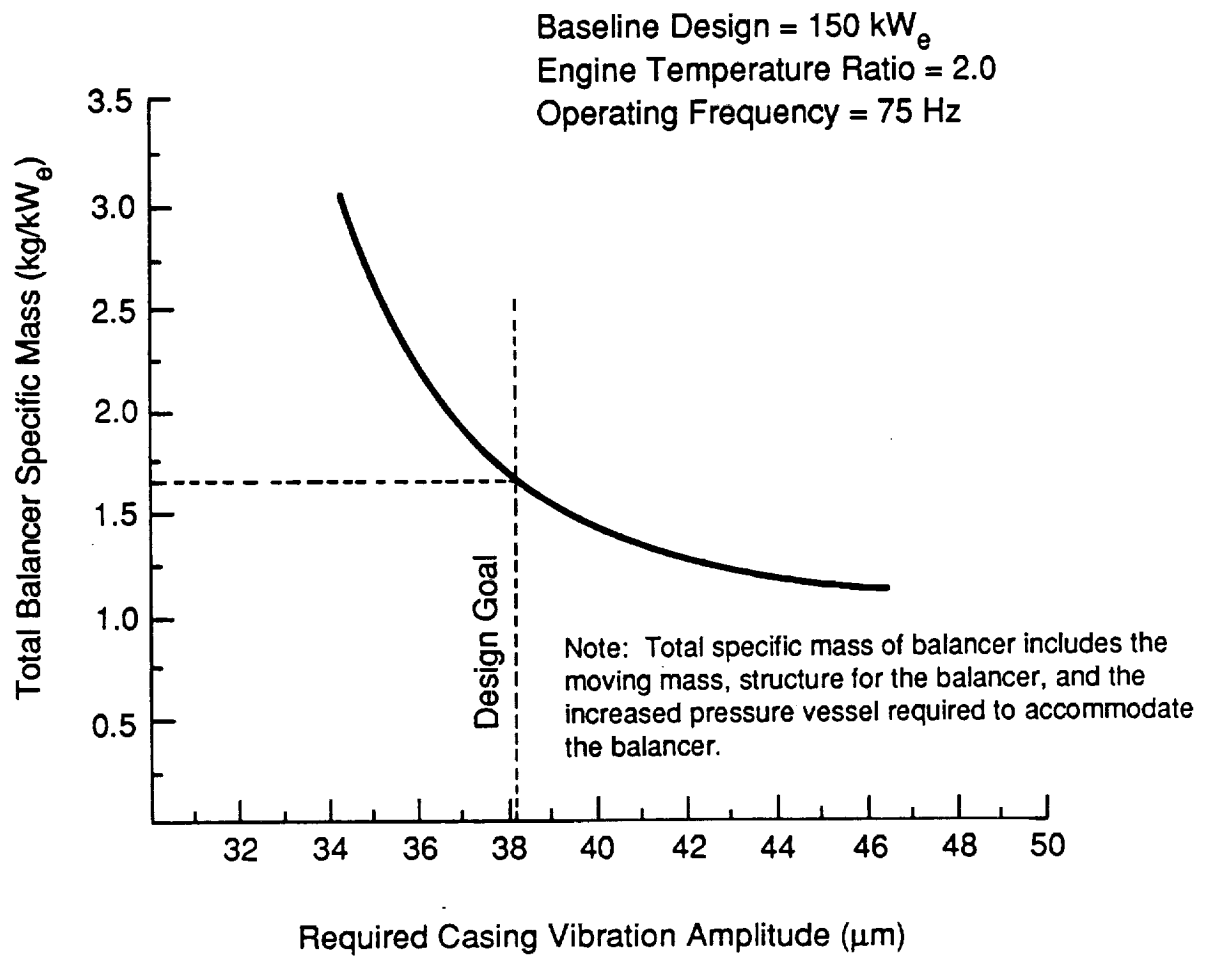
Figure 4-26. Power Module Casing Vibration versus Balancer Loss

Table 4-3. Dynamic Balance Unit - Performance and Mass Penalties\*

• Balance Gas Spring Losses (kW)	
— Hysteresis	1.21
— Leakage	1.20
— Porting	0.10
— Total	2.51
• Balance Unit Specific Mass (kg/kW <sub>e</sub> )	
— Moving Mass	1.29
— Cylinder and Structure	0.11
— Pressure Vessel	0.26
— Total	1.66

\*At baseline 150 kW<sub>e</sub> design point, engine temperature ratio = 2.0

C-2



89728

Figure 4-27. Balancer Total Specific Mass versus Required Casing Vibration Amplitude

### 4.3 Results

The terminology used to report the results of the parametric study is based on the latest formulation of efficiency standards for Stirling engine systems [4], originally defined in J. L. Crowley's paper [5], and subsequently modified for adoption by the Stirling Engine Committee of ASME. These standards have not yet been adopted, and may be subject to further revisions.

Accuracy of the results of this study is expected to be within 10% on power and efficiency, and within 5-10% on specific mass. For the performance predictions of opposed power modules (without the dynamic balancer), the parametric study results of the single-cylinder power modules with balancers were modified as reported in Section 4.3.4, but similar accuracy is expected.

The results of the parametric study are presented in Figures 4-28 through 4-30. Power module relative thermal efficiency (thermal efficiency + Carnot efficiency) is plotted as a function of power module specific mass for each power level, with temperature ratio as a parameter. Note that power module thermal efficiency includes the alternator efficiency. The curves at each temperature ratio and power level are defined by the three optimization points. The curves were drawn using the empirical equation developed to correlate the results (see Section 4.4). Since a quadratic relationship was used to map efficiency as a function of specific mass at constant temperature ratio and power level, the curves are of similar shape.

Discussion of the results is divided into three sections:

- General performance characteristics (relationships between efficiency and specific mass for all operating points)
- Heat exchanger temperature ratio sensitivity
- Power level sensitivity.

#### 4.3.1 General Performance Characteristics

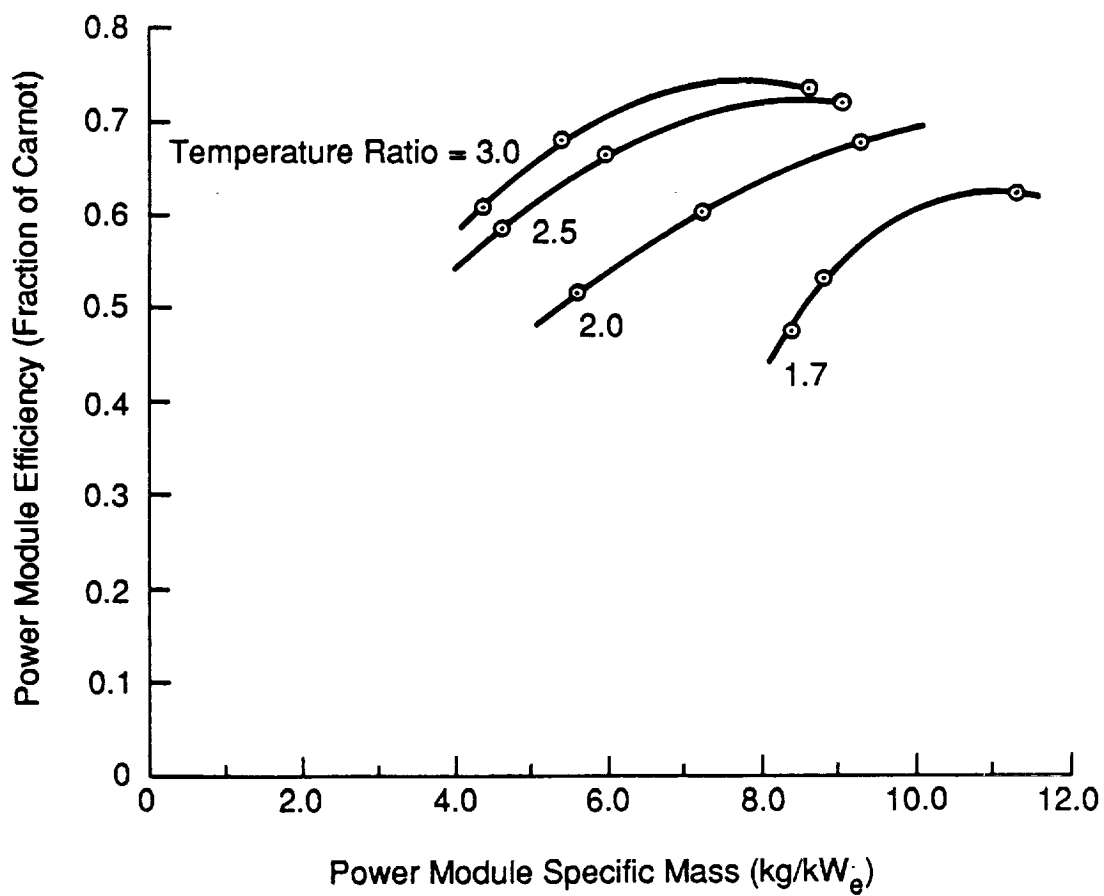
As seen in Figures 4-28 through 4-30, efficiency increases with increasing specific mass for all temperature ratios and all power levels. There is a diminishing gain in efficiency with increasing specific mass, as seen by the decreasing slope at the right end of each curve.

The maximum efficiency point on each curve represents the highest power module thermal efficiency that could be attained without unreasonable mass increase. For example, efficiency could be increased slightly by raising the engine mean pressure to 18 MPa, but would result in a large increase in specific mass, which was considered unreasonable.

The minimum specific mass point on each curve represents the lowest achievable power module specific mass. An increase in operating frequency results in decreasing engine efficiency. For frequencies greater than 90 Hz, the increased engine displacement required to maintain the power level causes an increase in specific mass. Since the curves are generated from only three points and fit with a quadratic relationship, they should not be extrapolated beyond the end points.

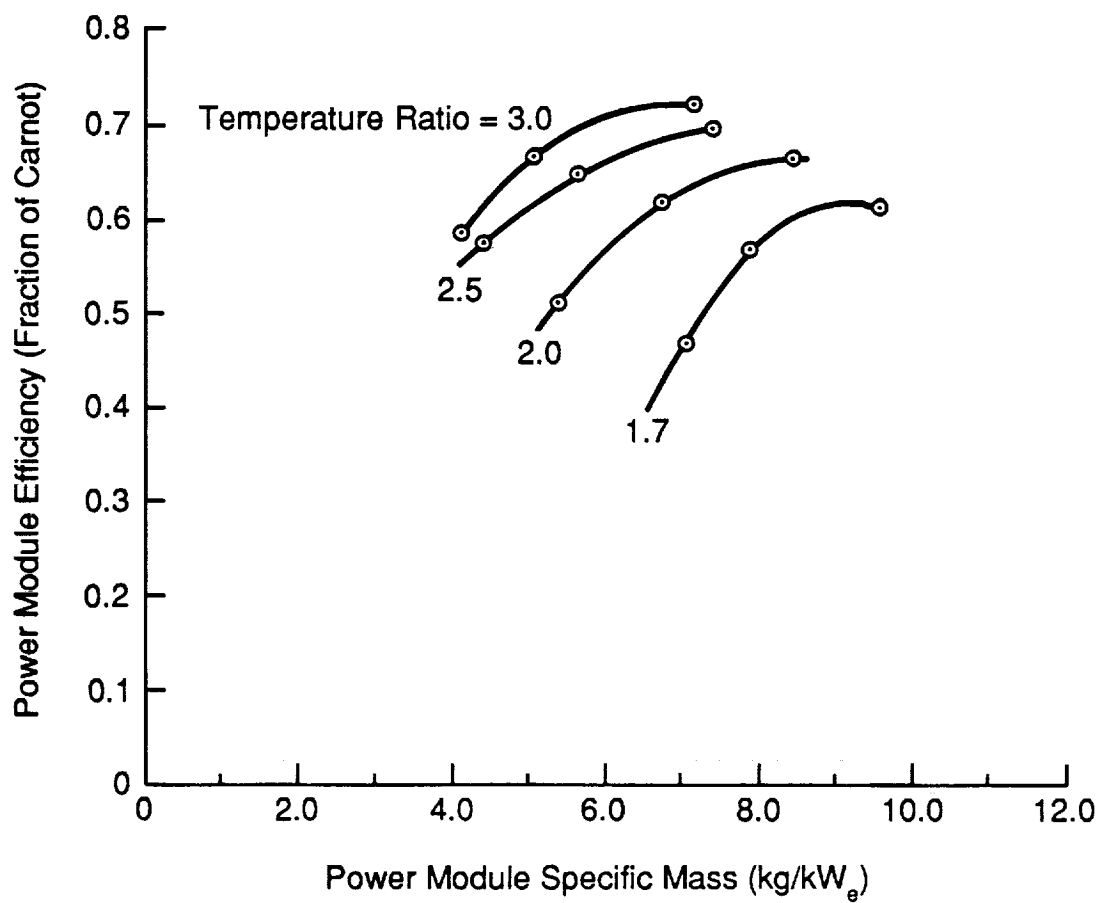
#### 4.3.2 Heat Exchanger Temperature Ratio Sensitivity

As seen in Figures 4-28 through 4-30, the percentage of Carnot efficiency increases with increasing temperature ratio for constant specific mass, and specific mass decreases with increasing temperature ratio for constant efficiency.



891026

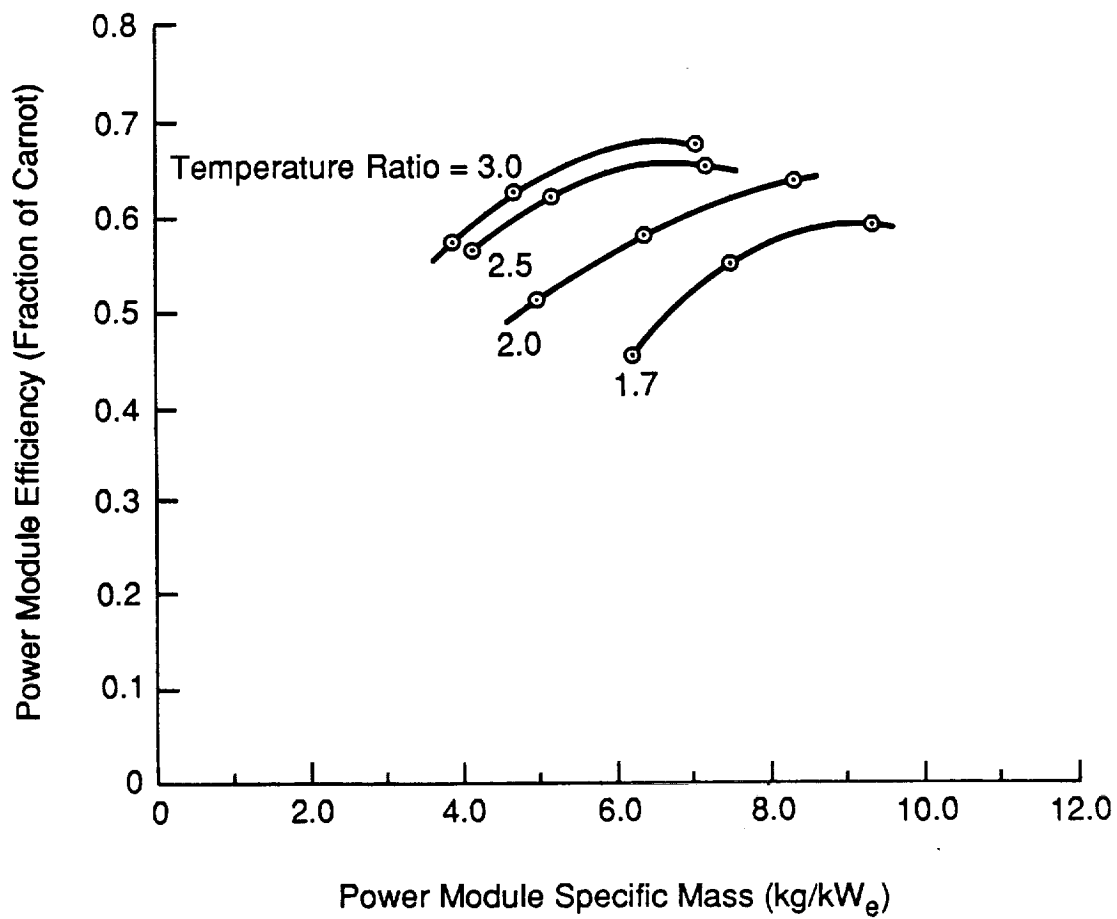
Figure 4-28. 150-kW<sub>e</sub> Power Module Parametric Study Performance Map



89773

Figure 4-29. 75-kW<sub>e</sub> Power Module Parametric Study Performance Map





89'30

Figure 4-30. 25-kW<sub>e</sub> Power Module Parametric Study Performance Map

Based on the relationship between temperature ratio and Carnot efficiency,  $\eta_{\text{Carnot}} = (T_R - 1)/T_R$ , for a constant power level the heat input (and therefore engine size) varies as an inverse function of temperature ratio,  $Q_{\text{in}} = T_R/(T_R - 1)$ . This explains the relative specific mass increase as the temperature ratio drops from 3.0 to 1.7.

Breakdowns of the performance and specific mass calculations show increases in all of the subsystem efficiencies with increasing temperature ratio, except for the alternator efficiency, which was held fixed. The mechanical efficiency increases because of the decrease in required engine displacement, and the corresponding drop in moving mass and gas spring requirements. All power module components have decreasing specific mass with increase in temperature ratio because of the overall reduction in engine size.

For a temperature ratio of 1.7, there was, as expected, a substantial increase in specific mass from a temperature ratio of 2. The drop in engine efficiency forces increases in engine displacement to maintain power, and the entire engine package increases in size.

#### 4.3.3 Power Level Sensitivity

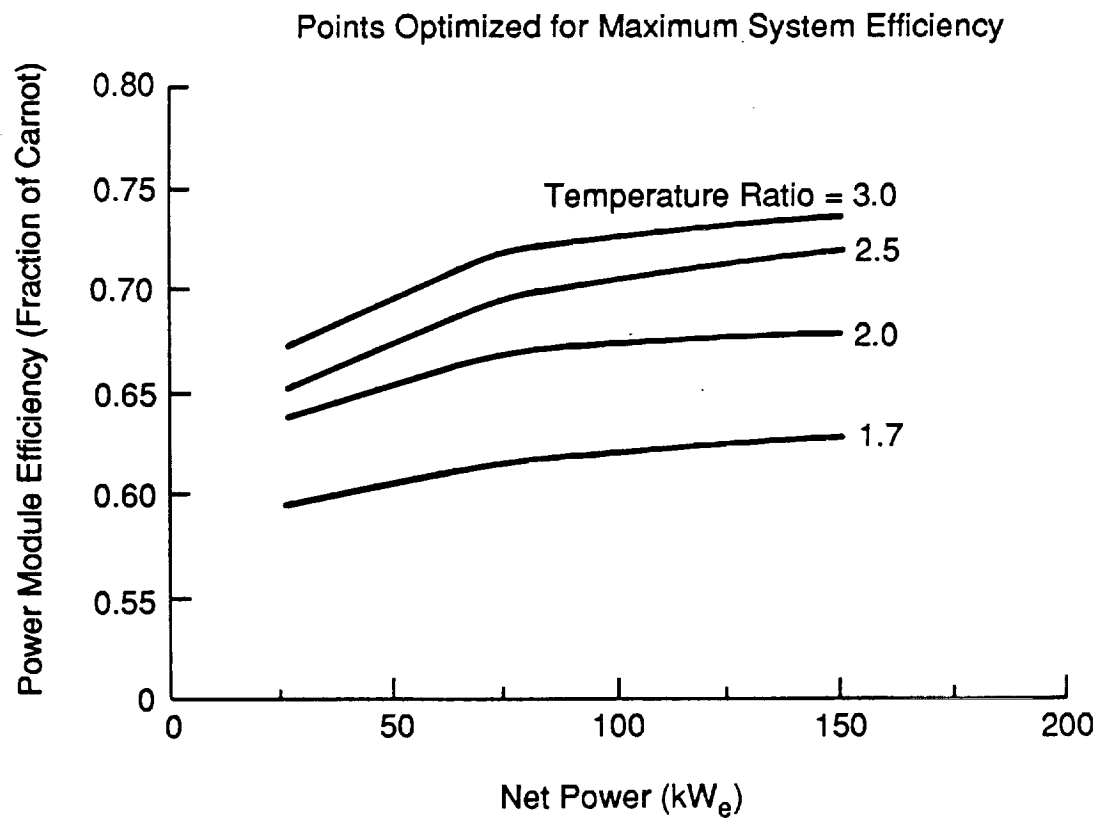
The change in efficiency and specific mass with engine power level is seen in Figures 4-31 and 4-32 for the power modules optimized for maximum efficiency. As shown, the efficiency increases with increasing power level, with a larger increase at higher temperature ratio. The specific mass also increases with increasing power level. The reason for the increase in efficiency is seen by looking at the sample efficiency and specific mass breakdowns given for different engines in Figures 4-33 through 4-40. At the lower power level, the heat-pipe requirements limit the frontal area of the heat exchangers, and the thermodynamic efficiency is lower than at 150 kW<sub>e</sub>, where the increased diameter results in increased frontal area. Due to the drop in cycle efficiency, the mechanical efficiency is also lower at 25 kW<sub>e</sub> because of the increased displacement required to make up for the efficiency loss.

The specific mass of the 25-kW<sub>e</sub> engine is lower than the higher power designs primarily because of the placement of the heat exchangers. Most of the weight savings occurs in the engine pressure vessel, which is at a relatively smaller diameter (compared to the displacer diameter) in the 25-kW<sub>e</sub> design.

Figures 4-41 and 4-42 show the performance as a function of power level for the power modules optimized for minimum specific mass. The overall trends are similar to those for the maximum efficiency power modules, but the sensitivities of efficiency and specific mass to power level are different. The efficiency growth as a function of power level for the minimum mass designs is less pronounced than for the maximum efficiency designs because increased efficiency was not the optimization goal. However, the specific mass growth with power level for the minimum mass designs was reduced relative to the maximum efficiency designs. For temperature ratios of 3.0, 2.5, and 2.0, the increase in specific mass with power level was very small. For all designs at a temperature ratio of 1.7 however, there is a strong dependence of specific mass on power level, owing to the mass penalties required in satisfying design constraints (heat-pipe heat flux limits, vibration level) at the low temperature ratio condition.

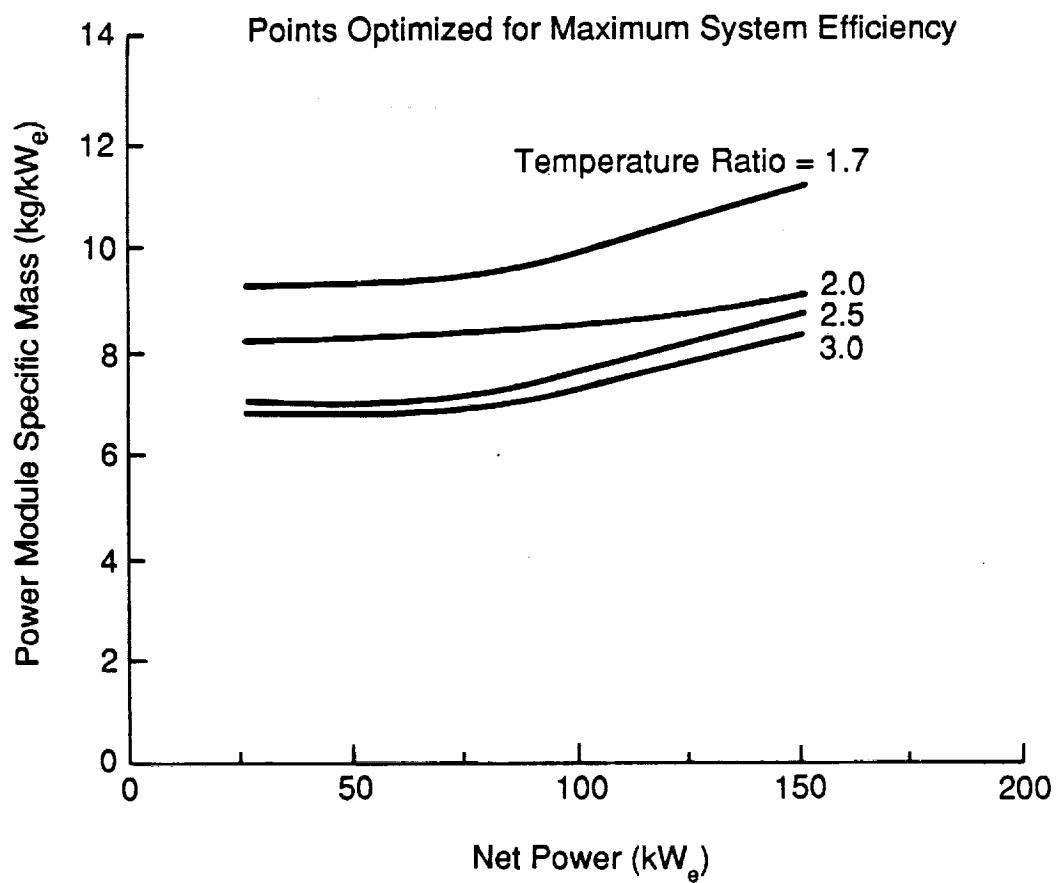
#### 4.3.4 Results for Opposed Power Modules Without Dynamic Balancer

The manner in which to join two identical single-cylinder power modules to obtain a dynamically balanced opposed power module was investigated. Attachment at either the hot ends or cold ends is possible, but the former results in the least additional structural mass and the shortest gas path for thermodynamic connection of the two engines. Design layouts of two hot-end structural attachments were made (Figures 4-43 and 4-44), differing in the heat-pipe design and penetration paths through the pressure vessel.



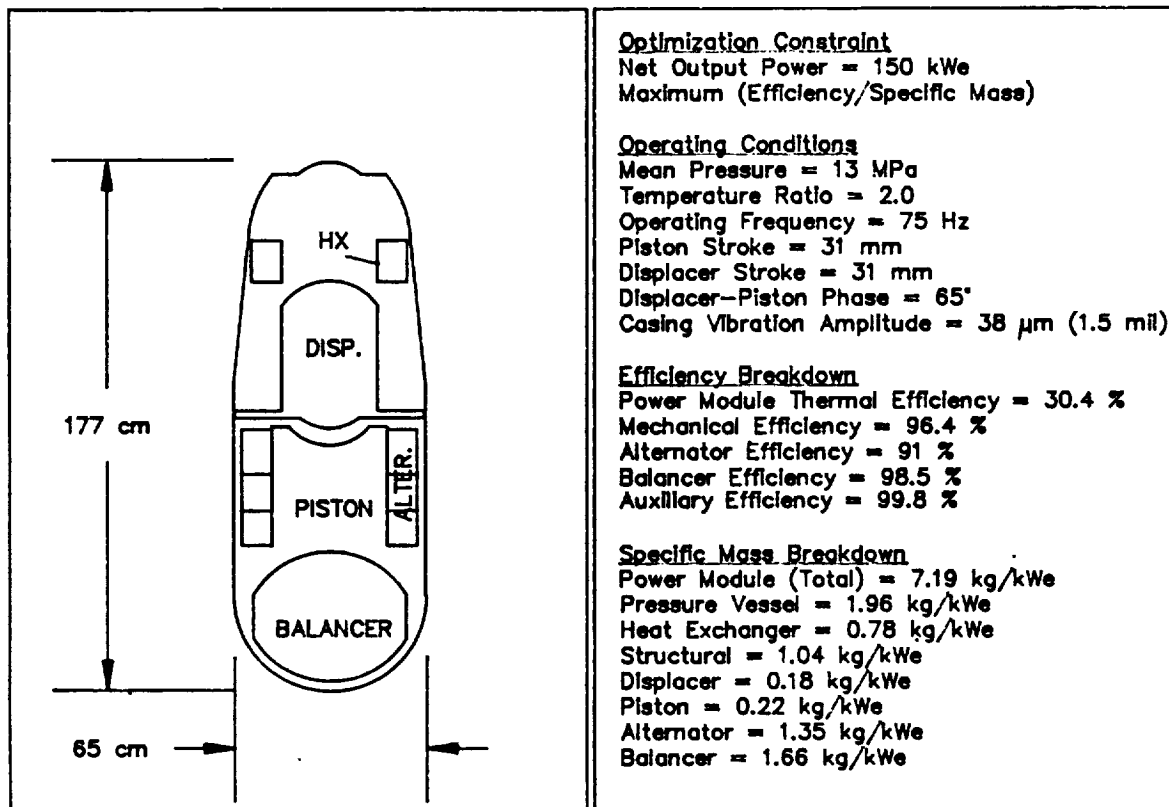
89731

Figure 4-31. Power Module Relative Efficiency versus Net Power



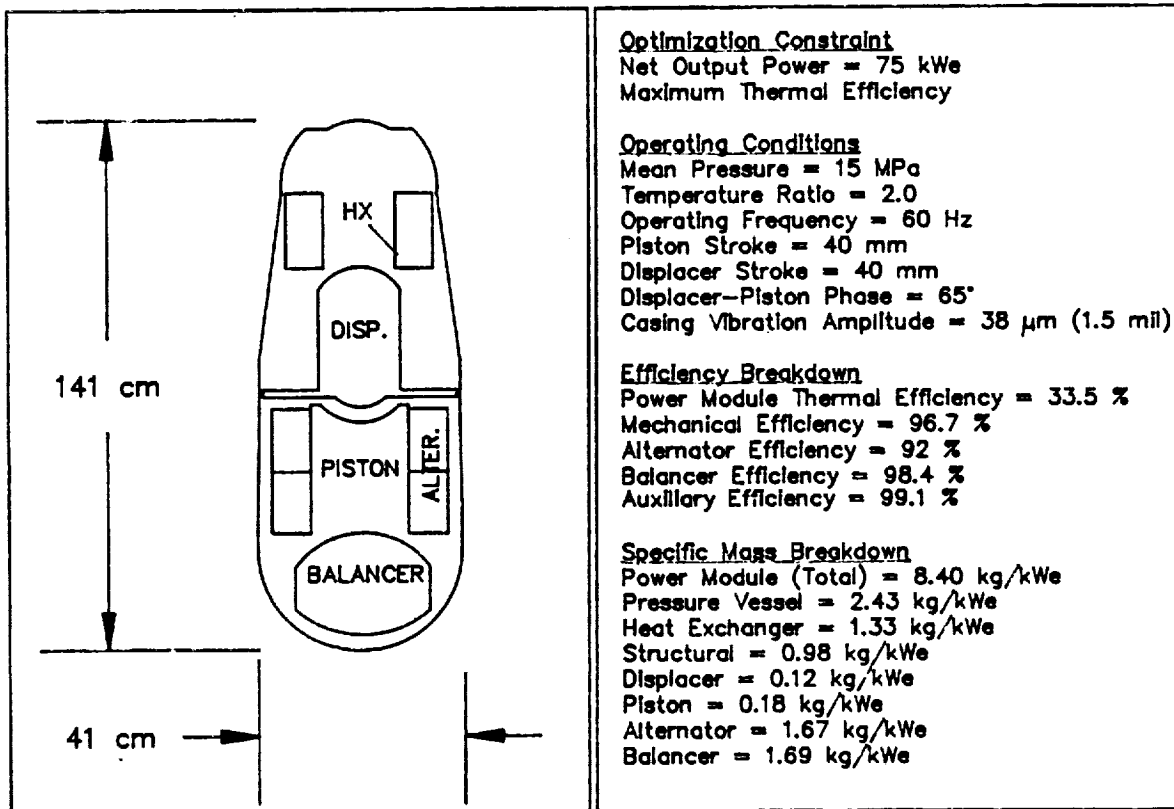
89734

Figure 4-32. Power Module Specific Mass versus Net Power



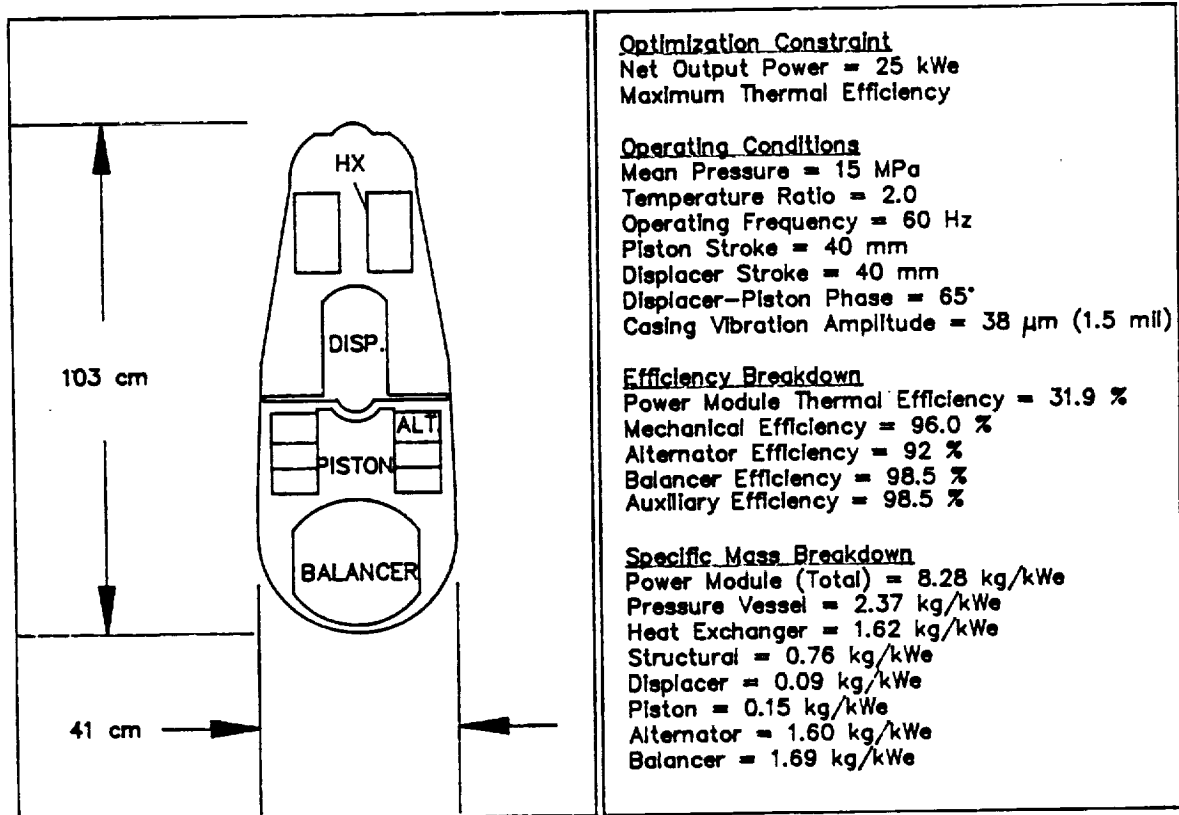
89741

Figure 4-33. 150-kWe Power Module (Temperature Ratio = 2.0) Optimized for Maximum Efficiency/Specific Mass. Performance and Specific Mass Summary



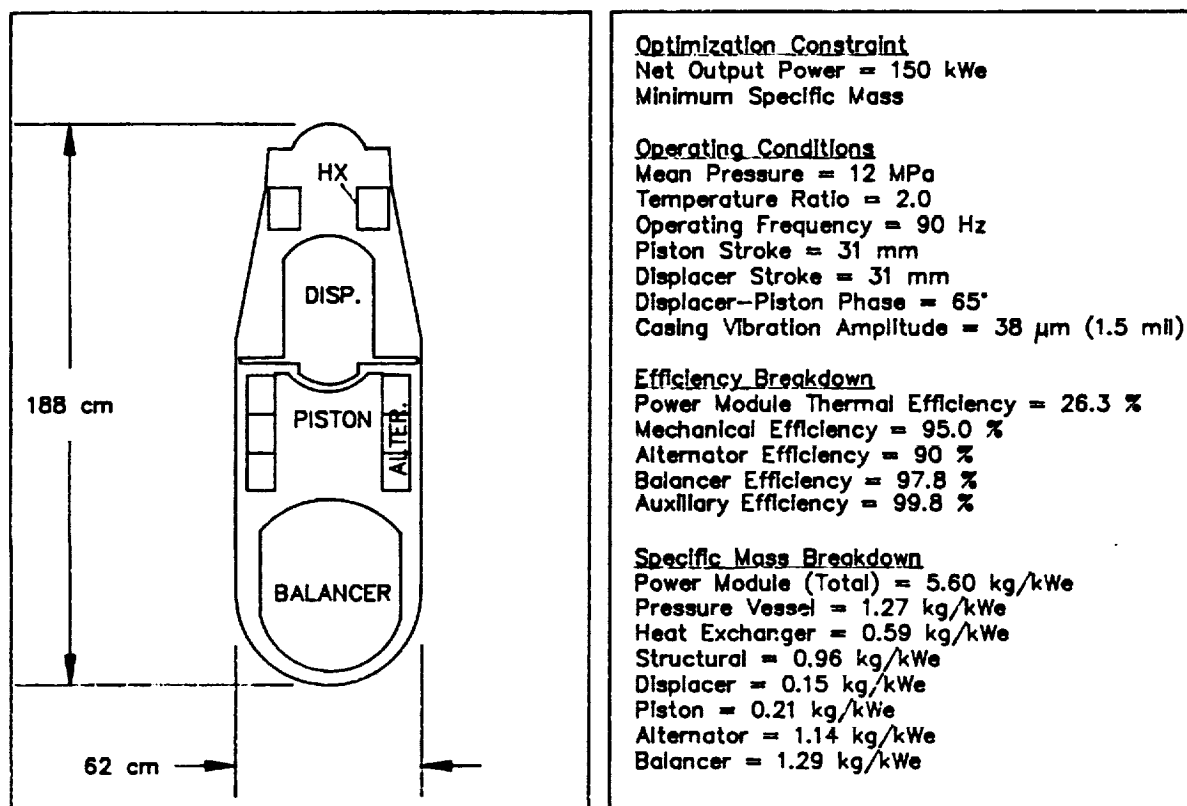
89743

Figure 4-34. 75-kWe Power Module (Temperature Ratio = 2.0) for Maximum Efficiency. Performance and Specific Mass Summary



89744

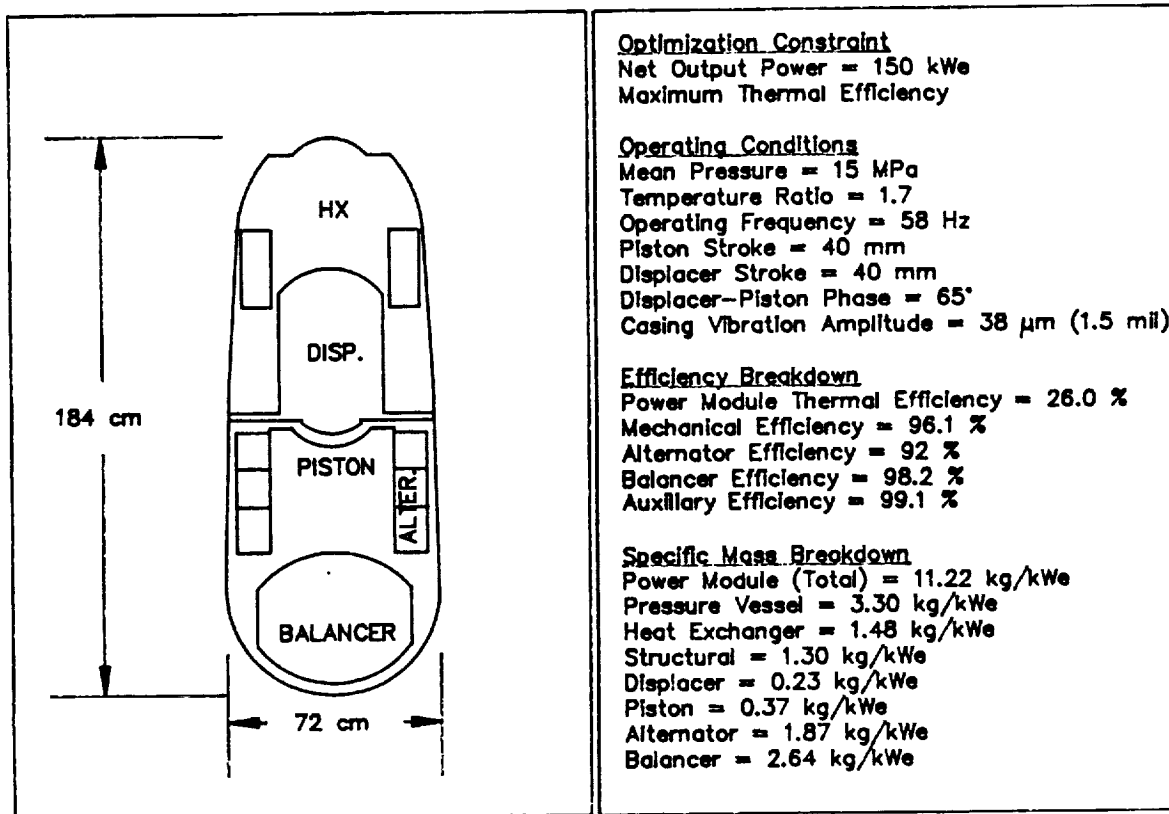
Figure 4-35. 25-kWe Power Module (Temperature Ratio = 2.0) Optimized for Maximum Efficiency. Performance and Specific Mass Summary



89742 -1

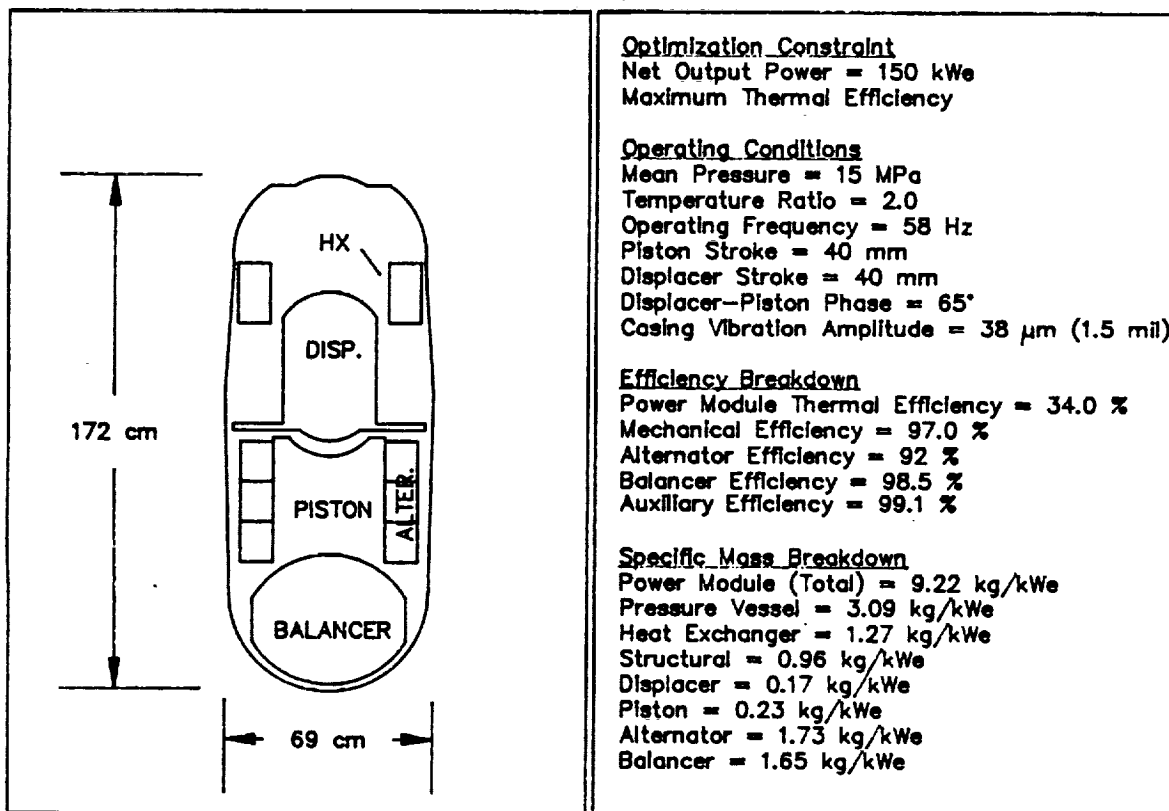
Figure 4-36. 150-kWe Power Module (Temperature Ratio = 2.0) Optimized for Minimum Specific Mass. Performance and Specific Mass Summary





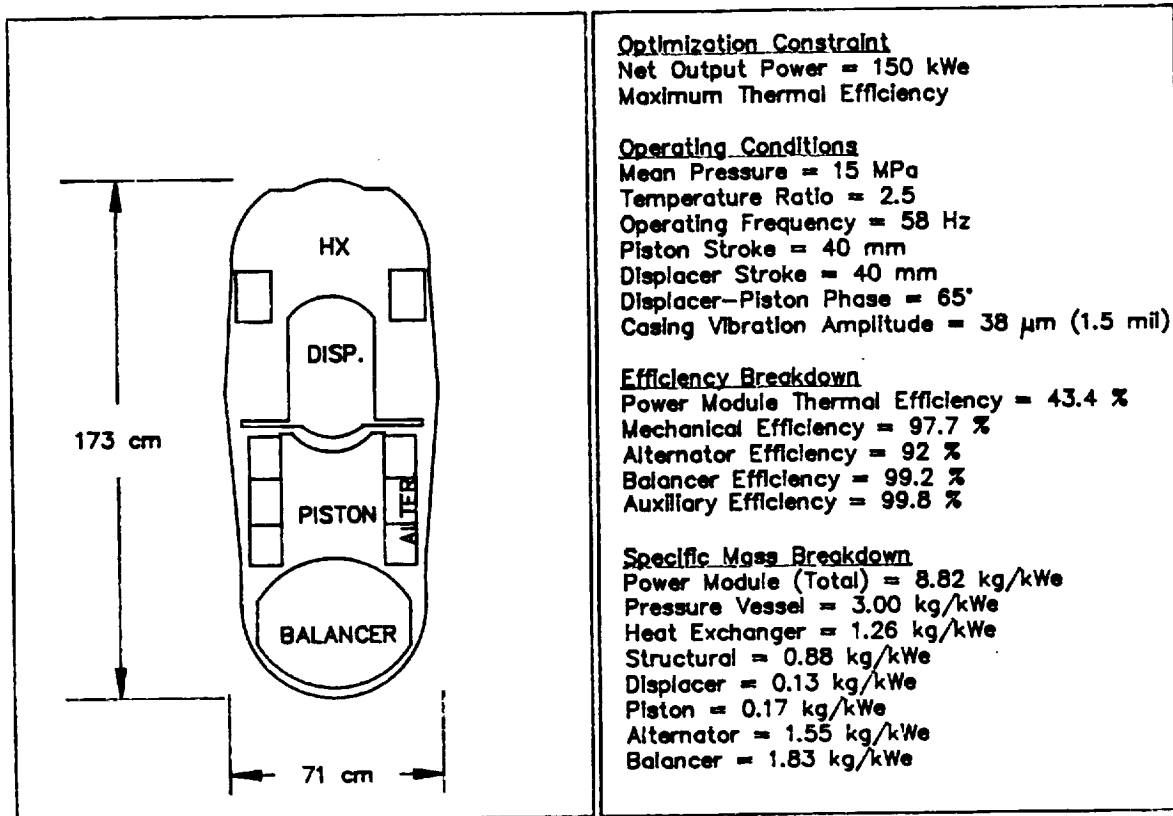
89737

Figure 4-37. 150-kWe Power Module (Temperature Ratio = 1.7) Optimized for Maximum Efficiency. Performance and Specific Mass Summary



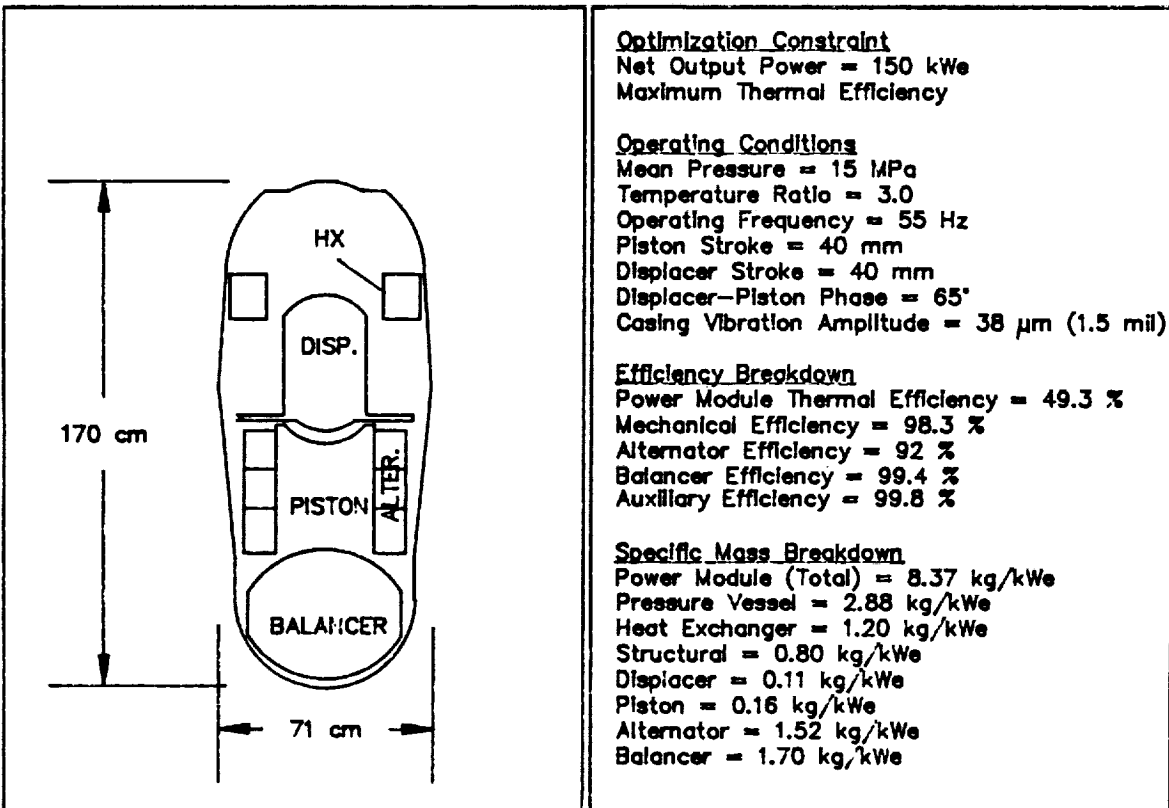
89738

Figure 4-38. 150-kWe Power Module (Temperature Ratio = 2.0) Optimized for Maximum Efficiency. Performance and Specific Mass Summary



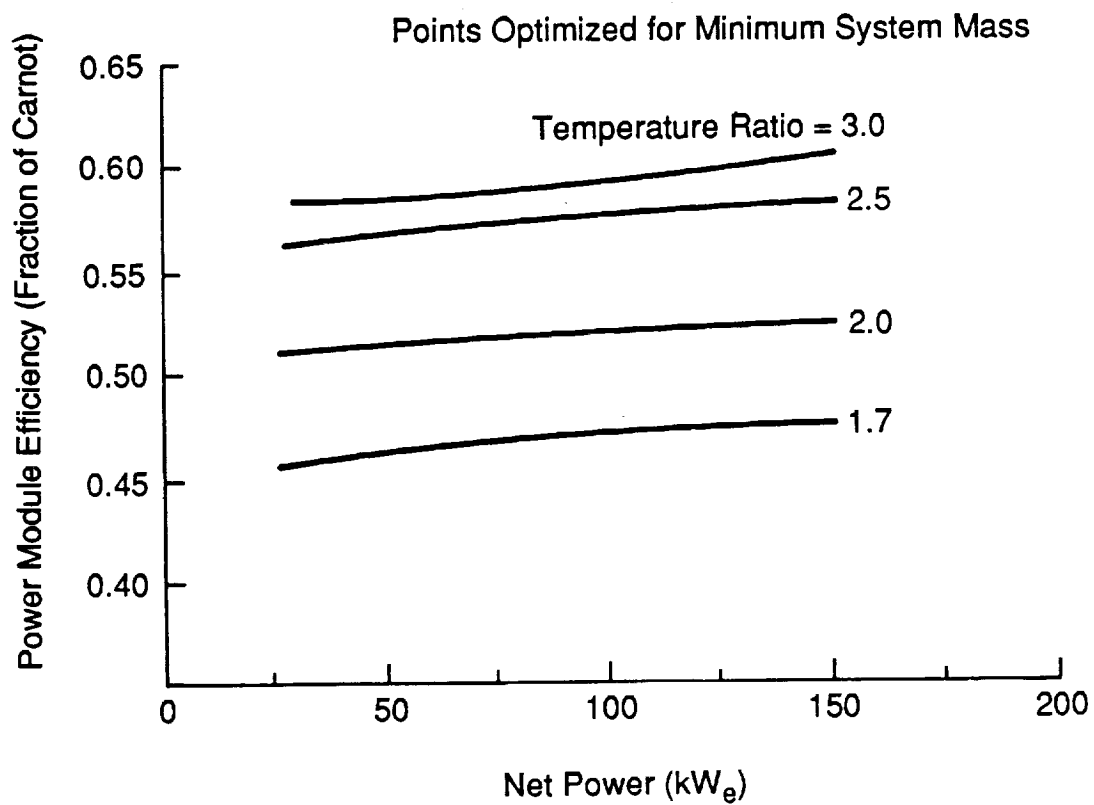
89739

Figure 4-39. 150-kWe Power Module (Temperature Ratio = 2.5) Optimized for Maximum Efficiency. Performance and Specific Mass Summary



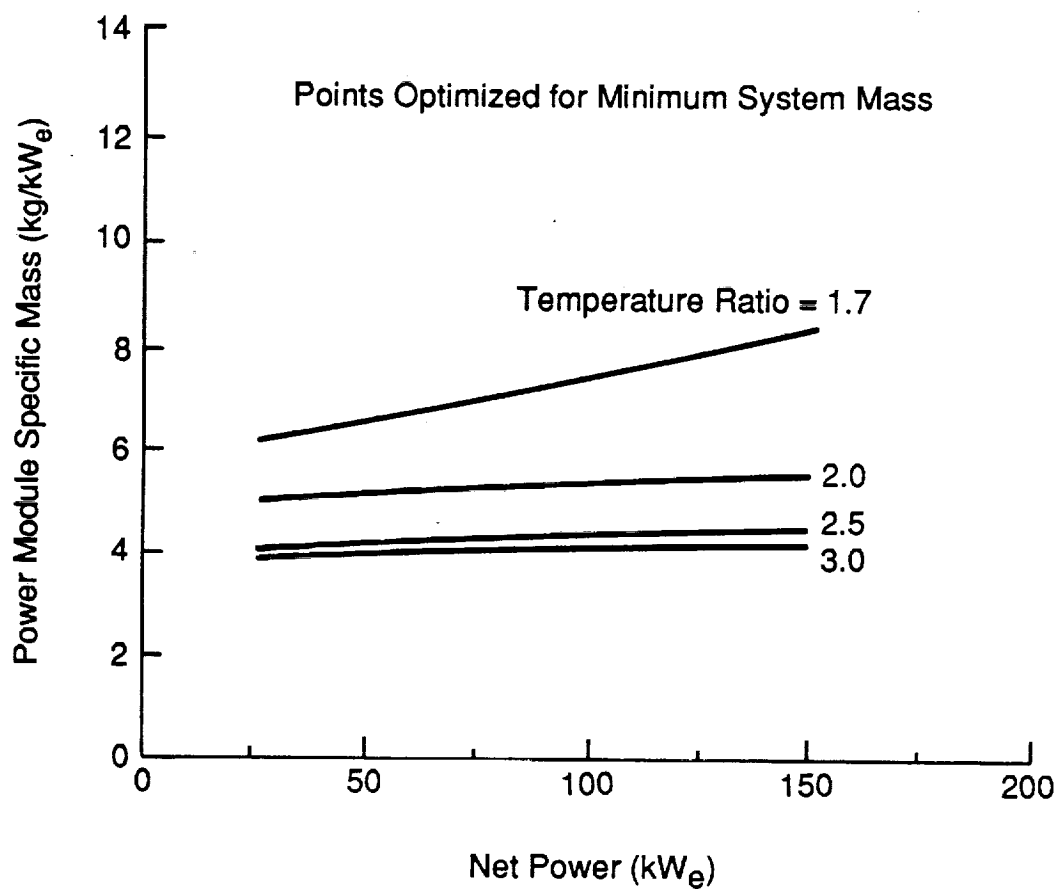
89740

Figure 4-40. 150-kWe Power Module (Temperature Ratio = 3.0) Optimized for Maximum Efficiency. Performance and Specific Mass Summary



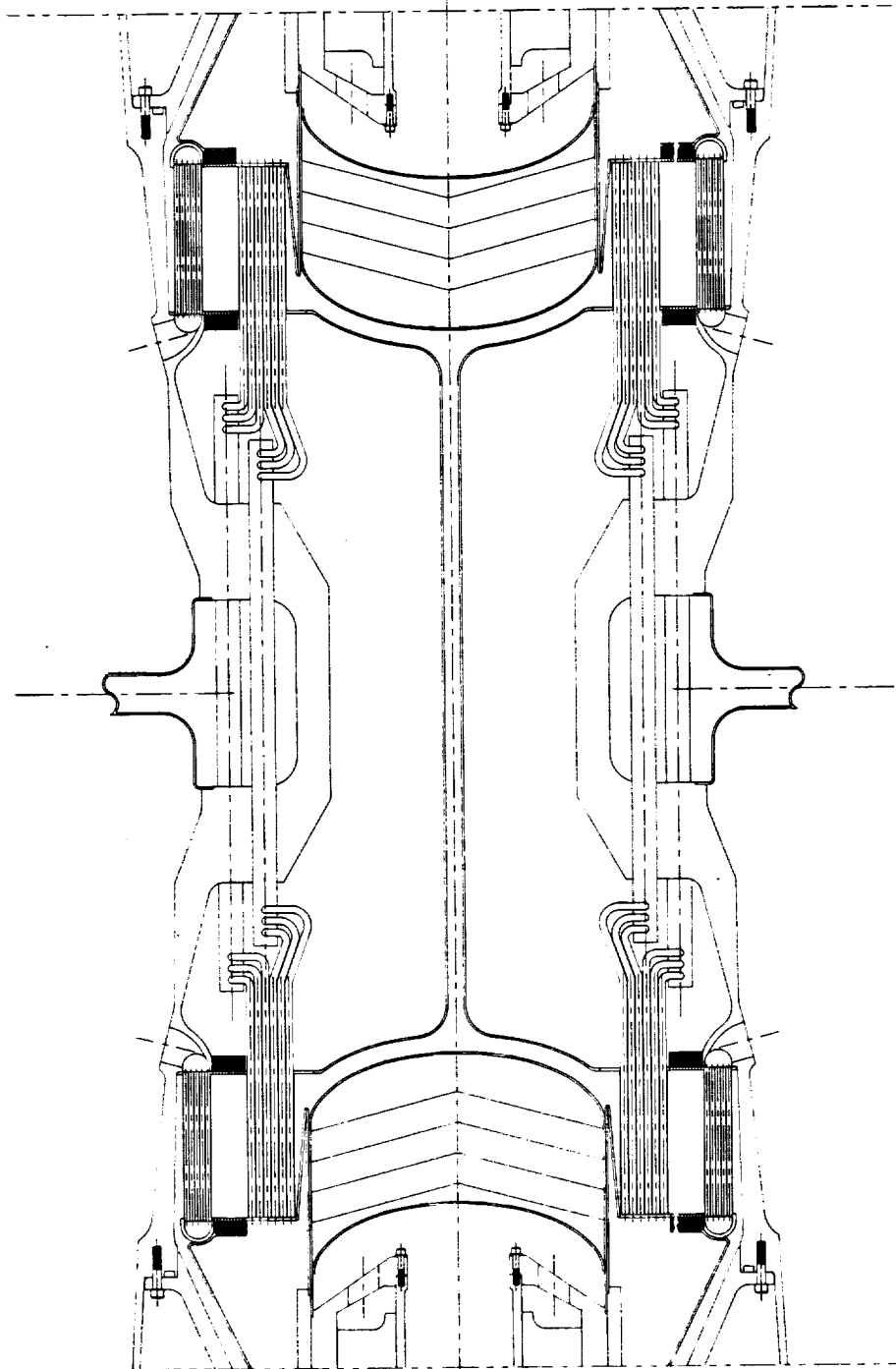
89733

Figure 4-41. Power Module Relative Efficiency versus Net Power



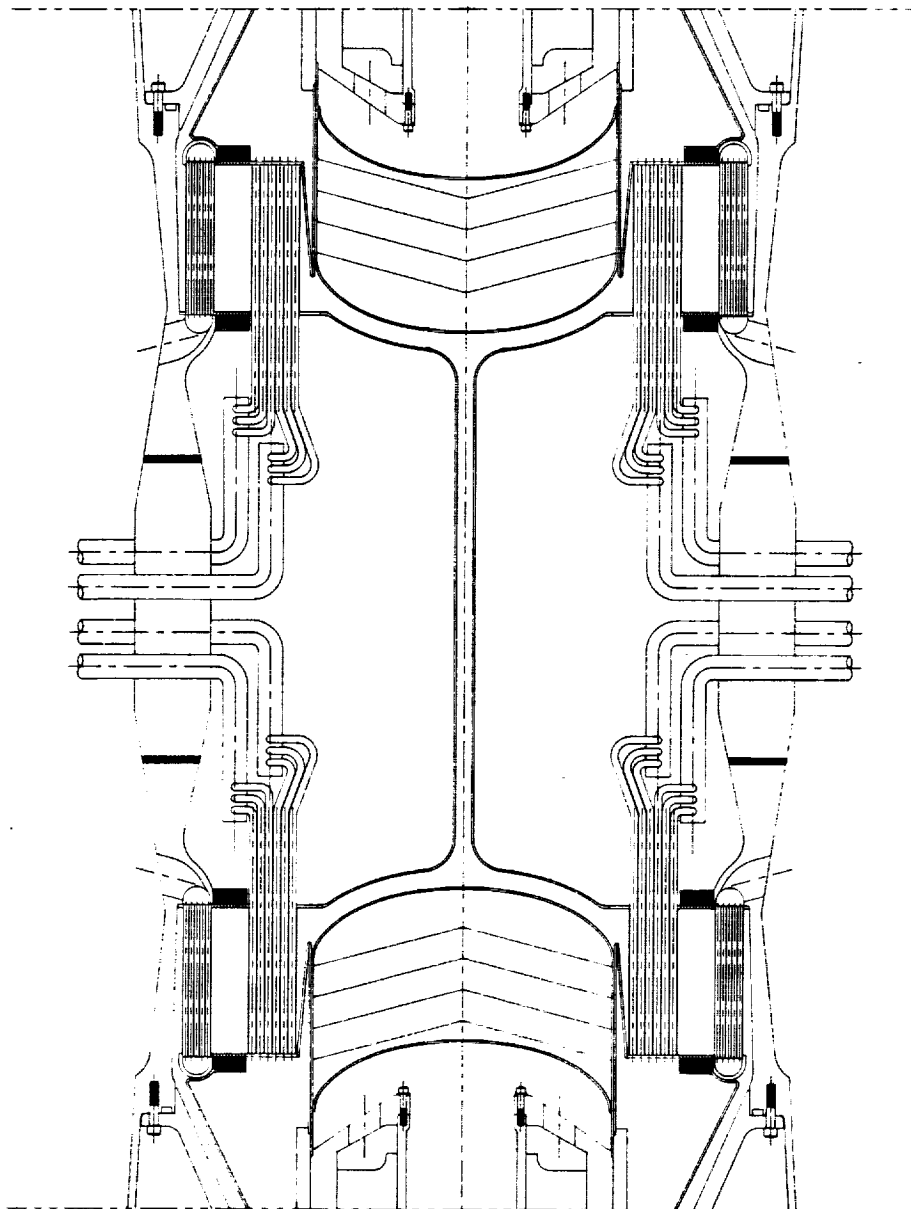
89732

Figure 4-42. Power Module Specific Mass versus Net Power



89776

Figure 4-43. FPSE Scaling Study - Double-Ended Radial Engine with Straight Main Heat Pipes



89777

Figure 4-44. FPSE Scaling Study - Double-Ended Radial Engine  
with Bent Main Heat Pipes



The design shown in Figure 4-43 used straight sections of the main heat pipes, with pipes from the opposed engine meeting in a central evaporator region. To avoid thermal expansion problems, the opposing heat pipes were separated by a small gap.

The domed section of the pressure vessel used in the single-cylinder designs was replaced with the cylindrical vessel inboard of the heat-pipe evaporators. The irregular shape of the pressure vessel in the central section was not considered structurally sound, and a second design, shown in Figure 4-44, was developed.

A thick-walled cylindrical vessel was used, with the heat pipes bent and exiting the vessel radially. By bending the heat pipes, the two engines can be moved closer together, and the length of the duct connecting the two expansion spaces is reduced from that of the first approach.

Based on the shortened duct length and improved structural design, the second configuration was selected for the purposes of calculating the specific mass of an opposed power module. The additional specific mass relative to a single-cylinder module (without balancer) is  $0.2 \text{ kg/kW}_e$ .

To obtain the resultant specific mass of the opposed power modules, this  $0.2 \text{ kg/kW}_e$  was added to the calculated specific mass values for the single-cylinder power module designs, and the dynamic balancer assembly specific mass was subtracted. The efficiency penalty of the connecting duct was negligibly small.

The efficiencies of the opposed power modules were simply the calculated efficiency values for the single-cylinder power module designs divided by the dynamic balancer efficiencies.

Figures 4-45 through 4-47 show the power module efficiency versus specific mass curves for the opposed power modules. The net power output of the opposed power modules is twice that of the single-cylinder power modules. Comparison with the results for the single-cylinder power module including dynamic balance assembly shows that the balancer increases power module specific mass by 20-30%, but has only a small impact on power module efficiency.

#### 4.4 Empirical Equation - Empirical Relationship Between Power Module Thermal Efficiency and Power Module Specific Mass, Net Power Output, and Temperature Ratio

Empirical equations were developed relating the power module relative net thermal efficiency (fraction of Carnot),  $\eta$ , to the power module specific mass,  $SM(\text{kg/kW}_e)$ , net power output,  $P_n(\text{kW}_e)$ , and heat exchanger temperature ratio,  $TR$ . One equation was developed for the single-cylinder power module with dynamic balancer, and one for the opposed power module. The 36 optimization points from the parametric study were used as the data base for the equations, with the efficiency and specific mass values modified for the second equation as noted in Section 4.3.3, and the power levels doubled.

Using a multiple linear regression analysis routine, the data were fit using quadratic functional relationships for  $SM$  and  $P_n$ , and a cubic functional relationship for  $TR$ :

$$\eta = f(SM) \times g(P_n) \times h(TR)$$

where

$$f(SM) = F_0 + F_1 SM + F_2 SM^2$$

$$g(P_n) = G_0 + G_1 P_n + G_2 P_n^2$$

$$h(TR) = H_0 + H_1 TR + H_2 TR^2 + H_3 TR^3$$

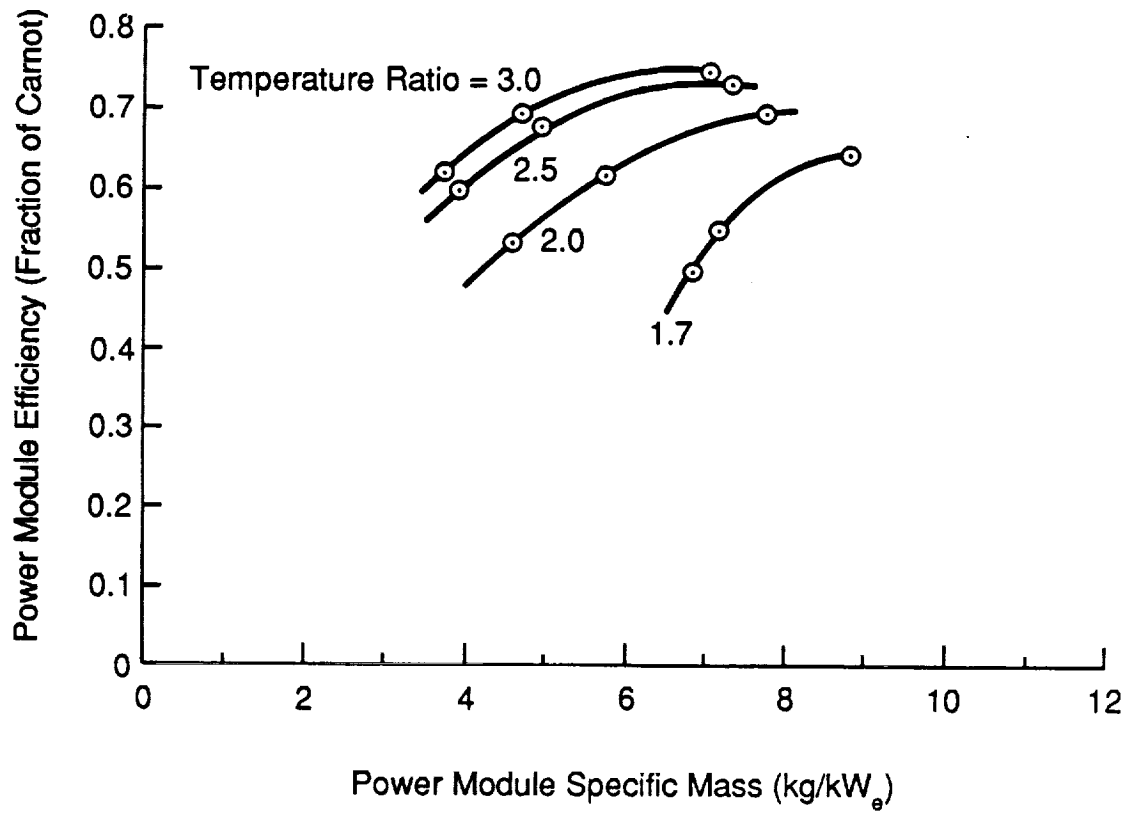
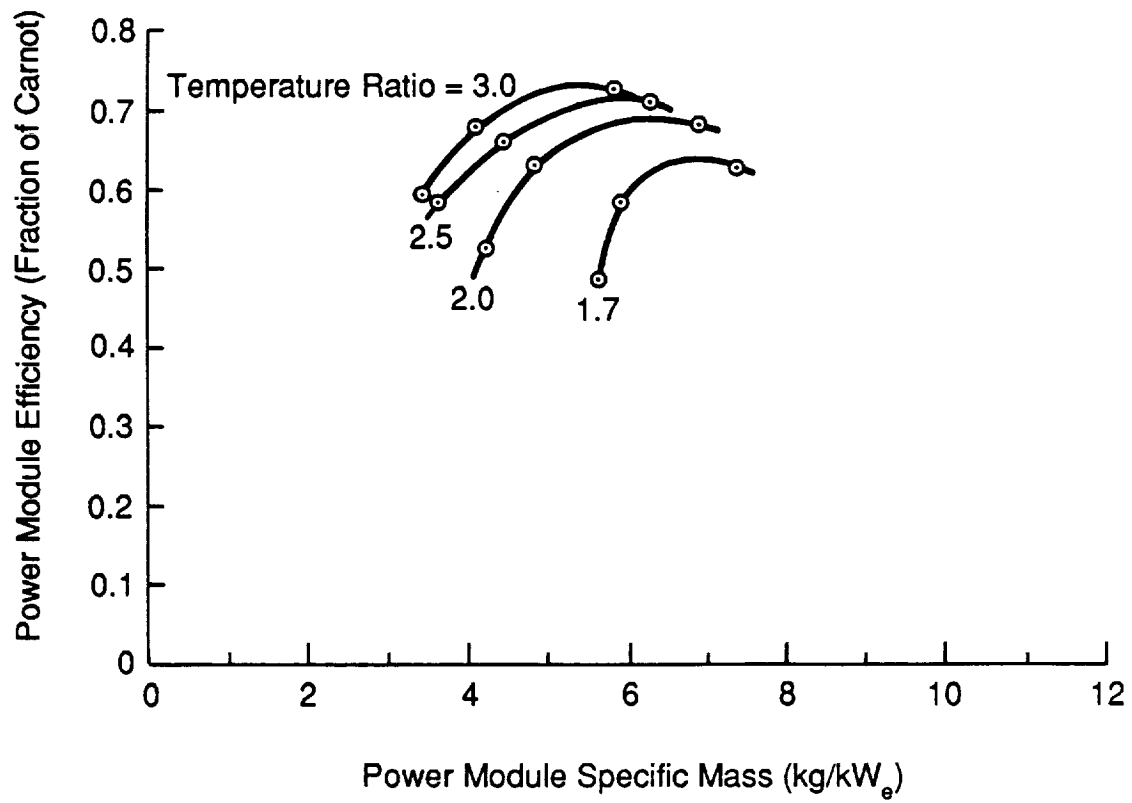


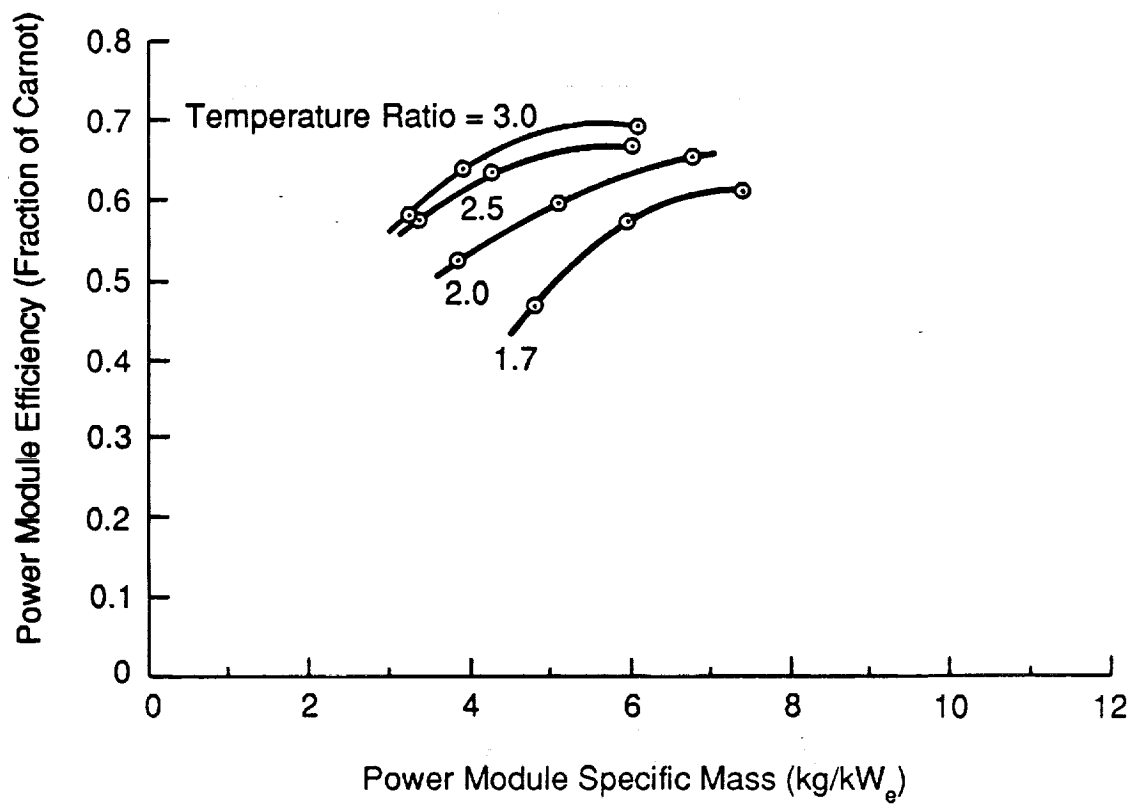
Figure 4-45. Two 150-kW<sub>e</sub> Opposed Power Modules  
(No Dynamic Balancer)

89747



89748

Figure 4-46. Two 75-kW<sub>e</sub> Opposed Power Modules  
(No Dynamic Balancer)



89746

Figure 4-47. Two 25-kW<sub>e</sub> Opposed Power Modules  
(No Dynamic Balancer)

The resulting equation, having 36 terms when expanded, is presented in Table 4-4. A listing of the curvefit coefficients for both the single-cylinder power module with dynamic balancer and the opposed power module is given in Table 4-5. The coefficients must be used as listed (without roundoff) to enable a good match with the parametric study results.

A separate empirical equation was developed (see Table 4-6) relating the power module relative net thermal efficiency to the power module specific mass and the heat exchanger temperature ratio for each of the three power levels of the study.

Figures 4-28 through 4-30 plot the parametric study results ( $\eta$  versus SM) for the single-cylinder power module with dynamic balancer. The study results are shown as points, with the lines showing the predicted efficiency using the empirical equation. Figures 4-36 through 4-38 show similar plots for the opposed power module results.

Table 4-4. Empirical Equation for Power Module Performance

Defining:

- $\eta$  = Power module relative thermal efficiency (% of Carnot)
- SM = Power module specific mass (kg/kW<sub>e</sub>)
- P<sub>n</sub> = Net power output (kW<sub>e</sub>)
- TR = Engine heat exchanger temperature ratio

The empirical equation correlating the parametric study data for both the single-cylinder power module and the opposed power module follows:

$$\begin{aligned} \eta = & C_1 TR^3 SM^2 P_n^2 + C_2 TR^2 SM^2 P_n^2 + C_3 TR \cdot SM^2 P_n^2 + C_4 SM^2 P_n^2 + C_5 TR^3 SM \cdot P_n^2 + \\ & C_6 TR^2 SM \cdot P_n^2 + C_7 TR \cdot SM \cdot P_n^2 + C_8 SM \cdot P_n^2 + C_9 TR^3 P_n^2 + C_{10} TR^2 P_n^2 + C_{11} TR \cdot P_n^2 + \\ & C_{12} P_n^2 + C_{13} TR^3 SM^2 P_n + C_{14} TR^2 SM^2 P_n + C_{15} TR \cdot SM^2 P_n + C_{16} SM^2 P_n + C_{17} TR^3 SM \cdot P_n + \\ & C_{24} P_n + C_{25} TR^3 SM^2 + C_{26} TR^2 SM^2 + C_{27} TR \cdot SM^2 + C_{28} SM^2 + C_{29} TR^3 SM + C_{30} TR^2 SM + \\ & C_{31} TR \cdot SM + C_{32} SM + C_{33} TR^3 + C_{34} TR^2 + C_{35} TR + C_{36} \end{aligned}$$

Table 4-5. Empirical Equation Coefficients

The 36 coefficients to the empirical equation (Table 4-4) are listed below according to the column headings for both power module configurations.

Single-Cylinder Power Module; Net Power Output: 25-150 kW<sub>e</sub>

$C_1-C_{12}$	$C_{13}-C_{24}$	$C_{25}-C_{36}$
0.0000098126717665	-0.0016329804199243	0.0890683179779442
-0.0000637899866933	0.0104733696192269	-0.6201434716902405
0.0001314383596679	-0.0211407942653943	1.3961589355952988
-0.0000831982928165	0.0129288569125929	-1.0190148425084742
-0.0001070690918442	0.0147095409843797	-1.0495845437253557
0.0006779935352504	-0.0879397940635658	7.3201968939974229
-0.0013353629589081	0.1565998914837785	-16.5148661844430649
0.0007714376539985	-0.0713870059425583	12.0952368836848549
0.0002654406564558	-0.0179266268831351	2.9801288845948442
-0.0016037282210588	0.0653517398685111	-20.9036177754398977
0.0028897151160238	0.0292806595266200	47.5575315482910810
-0.0013380782065787	-0.2035176538874985	-34.6706282623105153

Opposed Power Module; Net Power Output: 50-300 kW<sub>e</sub>

$C_1-C_{12}$	$C_{13}-C_{24}$	$C_{25}-C_{36}$
0.0000034032833664	-0.0010875921861443	0.1213563790573966
-0.0000218412667305	0.0068410851961330	-0.8435689869773280
0.0000437741181410	-0.0132359745435727	1.8868908638134485
-0.0000256019867646	0.0071580510664109	-1.3502897815778780
-0.0000279566619235	0.0065222672217835	-1.1092895625624735
0.0001714350325242	-0.0353412754405280	7.6879896739497617
-0.0003156829610467	0.0487993690371502	-17.0981398150323685
0.0001490999830328	-0.0010526706678782	12.1294862742535656
0.0000470175725501	0.0016662937919611	2.3039537954144507
-0.0002575752474368	-0.0463636806234717	-15.9131421819329262
0.0003634104541441	0.2121982920741097	35.1995043821637523
-0.0000201920576890	-0.2717606249352293	-24.1889054574081115

Table 4-6. Empirical Equation and Coefficients for Power Module Performance Operating at Specified Power Levels

Defining:

- $\eta$  = Power module relative thermal efficiency (% of Carnot)  
 $SM$  = Power module specific mass (kg/kW<sub>e</sub>)  
 $TR$  = Engine heat exchanger temperature ratio

The empirical equation correlating the parametric study data is as follows:

$$\eta = C_1 TR^3 SM^2 + C_2 TR^2 SM^2 + C_3 TR SM^2 + C_4 SM^2 + C_5 TR^3 SM + C_6 TR^2 SM + C_7 TR SM + C_8 SM + C_9 TR^3 + C_{10} TR^2 + C_{11} TR + C_{12}$$

Coefficients for each of three specified power levels of the single-cylinder and opposed power modules are listed below in order from  $C_1$  through  $C_{12}$ :

#### Single-Cylinder Power Module

$P_n = 25 \text{ kW}_e$	$P_n = 75 \text{ kW}_e$	$P_n = 150 \text{ kW}_e$
0.0543767273338744	0.0217910651699640	0.0649063697346719
-0.3981779728928814	-0.1934594253980322	-0.4844127294054488
0.9497880537528545	0.5499401388224214	1.1824028883129358
-0.7477923527039820	-0.5173409711569548	-0.9516478939913213
-0.7487642015184974	-0.5486326115205884	-1.2522079625632614
5.5454480019398034	4.5384259750135243	9.3840823275968432
-13.4344707466661930	-12.2812909670174122	-23.0705490373075008
10.7927102688699961	11.0805482417345047	18.7445332072675228
2.6978636228013784	3.1287355609238148	6.2635496223811060
-20.2721544168889523	-25.0232085287570953	-47.1847417689859867
50.0956199839711189	66.0082285404205322	116.9682205878198150
-40.5948684886097908	-57.4611422158777714	-95.3050359934568405

#### Opposed Power Module (No Balancer)

$P_n = 50 \text{ kW}_e$	$P_n = 150 \text{ kW}_e$	$P_n = 300 \text{ kW}_e$
0.0754849781660596	0.0347914268786553	0.1013742261857260
-0.5561178939969977	-0.3088347089942545	-0.7569574338849634
1.3345274319872260	0.8864123404491693	1.8557691334281117
-1.0563921951688826	-0.8526268238201737	-1.5070532704703510
-0.8530678562819958	-0.7599743725731969	-1.6687089691404253
6.3495134832337499	6.2440865896642208	12.5147599689662457
-15.4473787657916546	-16.8811010830104351	-30.8697955980896950
12.4496026984415948	15.3263352923095226	25.2326835468411446
2.5048124163877219	3.6117932465858757	7.0354234625119716
-18.8752643316984177	-28.6631373427808285	-53.0040186382830143
46.7179451212286949	75.2059834115207195	131.5659328773617740
-37.8274168483912945	-65.4073204956948757	-107.5343781299889090



## 5.0 ALTERNATIVE CONFIGURATIONS

The purpose of Task III in the Statement of Work was to review alternative FPSE configurations that may offer advantages over the FPSE/LA configuration for a power output of 100 to 150 kW<sub>e</sub>. Due to the limited available time to perform this task, it was agreed at the start of the program that the alternative configurations would be limited to the following two cases: (1) multicylinder FPSE (Renia configuration), and (2) alternative power takeoff using a magnetic coupling and rotary alternator. The results of the brief review of these concepts, summarized below, show the FPSE/LA configuration to be the best choice for meeting the design requirements.

### 5.1 Multicylinder Arrangement

The possible motivations for using multicylinder FPSEs for this application are as follows:

- For 100- to 150-kW<sub>e</sub> power output, the piston size in an eight-cylinder, double-acting Renia configuration engine is close to current practice
- Potentially compact configuration -- reduced specific mass
- Simple mechanical design
- Naturally balanced
- Good load stability characteristics.

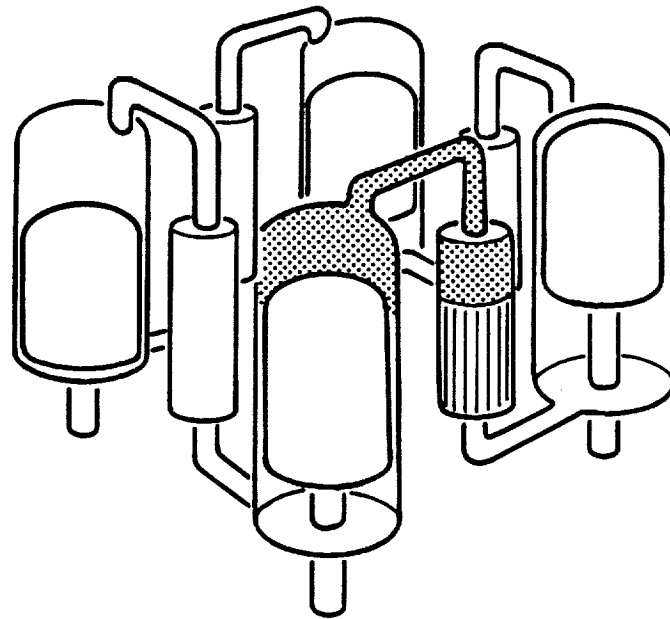
#### 5.1.1 Renia Configuration FPSE/LA Description

The general arrangement of a four-cylinder Renia engine configuration is shown in Figure 5-1. The arrangement investigated for this study is shown in a rough cutaway sketch in Figure 1-5. The engine is composed of eight hot-cylinder assemblies welded between two base plates, forming an octagonal array. Each hot-cylinder assembly is comprised of an expansion cylinder, heater, regenerator, and cooler section. The hot-cylinder assemblies are alternately reversed (i.e., the first assembly has the expansion cylinder-heater-regenerator-cooler, while the adjacent assembly has the cooler-regenerator-heater-expansion cylinder, etc.). The double-acting piston fits in the expansion cylinder pressure vessel, the cold end of which attaches to the base plate. The cold end of the piston fits in a cold cylinder, which is bolted to the base plate. A rod attached to the cold piston face passes through the base plate and drives a gas spring piston and the alternator plunger. The gas spring cylinder is bolted to the back side of the base plate, and the alternator stator attaches to the cylinder. The gas spring/alternator assembly is mounted within a pressure vessel that is sealed by welding to the base plates.

With proper adjustment of heat exchanger and piston lengths, the hot sections of the hot cylinder assembly all line up in a central zone between base plates, thus isolating the attachment points at the cylinder ends from the hot zone. Shell-and-tube type heaters and coolers would be used, with wicks on the shell side of the heater tubes, connected to sodium heat pipes. The cooler would be part of a NaK pumped-loop heat rejection system.

The piston is supported on hydrodynamic gas bearings and is spun by a small motor located in the gas spring cylinder. The seals in the engine are all close-clearance, nonrubbing seals.

This Renia arrangement is thermodynamically attractive because the flow path from expansion to compression spaces is straight and clean, with no hot ducting and only a short cold duct connecting the cooler of one assembly to the compression space of the adjacent cylinder. Also, the power module actually consists of two opposed Renia engines, each composed of four double-acting pistons moving at 90° phase separation. Dynamic vibration of the assembly can be nominally balanced by running the engines



Working Gas in One of the Cycles of a  
Four-Cylinder Stirling Engine Module

89736

Figure 5-1. Typical Renia Engine Configuration

in phase, thereby internally canceling the forces from the reciprocating masses. Perfect balance is only achieved, however, for identical cycle-to-cycle dynamic, thermodynamic, and electrical parameters. Since some variation in parameters is expected, some degree of dynamic imbalance and system vibration will be experienced. For a 150-kW<sub>e</sub> power module with a specific mass of 6 kg/kW<sub>e</sub>, a dynamic imbalance equal to 20% of the mass of one piston would be required to result in a free vibration casing amplitude of 0.038 mm. Since this is a large imbalance, it is expected that the opposed engine configuration could easily meet the maximum vibration level requirements.

### 5.1.2 Thermodynamics

Analysis of the thermodynamic performance of the Renia FPSE was performed using the MTI harmonic analysis code. Table 5-1 shows the operating conditions, predicted performance, and estimated specific mass of this concept. The power module thermal efficiency of 30% is comparable to the single-cylinder baseline design. The engine-indicated efficiency is slightly lower than that for the baseline case, while the mechanical efficiency is greater since the number of seals and gas springs per cylinder is less. The performance predictions do not account for increased appendix gap seal loss, which is described below. The estimated power module specific mass is slightly lower than that for the baseline design.

The drawback to this configuration is the appendix gap seal requirements. In a displacer-type FPSE, the pressure gradient across the appendix gap seal is only the heat exchanger pressure drop, and a relatively loose clearance seal can be used. In a Renia engine the expansion volume pressure at the top of a piston is 90° out of phase with the compression space pressure at the bottom of the piston. This occurs because the two volumes are in different thermodynamic cycles. Therefore, the appendix gap seal  $\Delta P$  in the Renia engine is the full engine pressure amplitude, and the use of a clearance seal introduces a large loss on the engine. This loss is not simply a leakage loss, but also enthalpy flux, since the gas entering the seal from the appendix gap is at a higher temperature than the compression space gas.

One possible solution to the enthalpy flux loss would be to route the leakage flow through a regenerator, but this introduces added complexity to the system and requires further evaluation. Use of a contacting piston ring would greatly reduce the leakage problem, but compromises the machine life.

Because of this appendix gap difficulty, the Renia FPSE concept is not a recommended engine configuration as an improvement over the single-cylinder FPSE/LA configuration.

### 5.2 Alternative Power Takeoff

The baseline FPSE/LA used in this study is a direct-connected configuration -- a configuration in which the reciprocating piston of the engine is directly coupled to the reciprocating plunger of the linear alternator. This configuration provides a mechanically simple convertor unit with good electrical efficiency and reasonably low specific mass. However, the inherent synchronous tie between the linear alternator electrical frequency and the engine mechanical frequency forces a design compromise in the selection of power module operating frequency. The engine favors a low frequency for efficiency reasons, and the alternator favors a high frequency for mass reasons. This compromise penalizes the power module efficiency, and imposes a mass penalty on the alternator and downstream power conditioning components such as the tuning capacitors and, if required, the rectifier filtering system.

**Table 5-1. Multicylinder FPSE/LA (Renia Configuration) Summary**

**Operating Conditions**

• Mean Pressure	15 MPa
• Frequency	90 Hz
• Engine Temperature Ratio	2.0
• Piston Stroke	31 mm

**Performance**

• Net Output Power	150 kW <sub>e</sub>
• Power Module Thermal Efficiency	30%
• Indicated Engine Efficiency	34%
• Mechanical Efficiency	96%
• Alternator Efficiency	92%

**Specific Mass**

• Power Module (Total)	6.3 kg/kW <sub>e</sub>
• Pressure Vessel and Structure	1.9 kg/kW <sub>e</sub>
• Engine Internals	2.9 kg/kW <sub>e</sub>
• Alternators	1.5 kg/kW <sub>e</sub>

In earlier FPSE/LA systems, the alternator specific mass ranged from 2 to 3 kg/kW<sub>e</sub>. This range indicated the possibility of significant mass reduction by use of an indirect-connected configuration. In such a configuration, a linear-to-rotary convertor (see Figure 1-6) is interposed between the engine and a conventional rotary alternator. The synchronous tie inherent in the direct-connected configuration is thus broken, and the alternator electrical frequency can be increased above the engine mechanical frequency by using multiple poles. The critical component in this system is the linear-to-rotary convertor. The weight, efficiency, and reliability debits associated with this component must not outweigh the credits obtained by breaking the synchronous tie. In addition, the convertor must integrate with the engine and alternator from stability, operational, mechanical, and structural points of view.

For the baseline configuration of this study, the alternator specific mass has been reduced to less than 1.5 kg/kW<sub>e</sub>\* making the potential benefits associated with an indirect-connected configuration relatively small.

A permanent magnet coupling/rotary alternator was evaluated and compared with the baseline system. Table 5-2 shows the operating conditions, predicted performance, and estimated specific mass of this concept. The power module thermal efficiency of 30% is comparable to the single-cylinder baseline design. The engine indicated efficiency and mechanical efficiency are the same as the baseline case (since the same engine is assumed). The converter loss is due to eddy currents induced in the converter back iron, and amounts to 5% of the total engine power. The alternator efficiency was estimated based on an advanced 16-pole permanent magnet rotary alternator. The power module specific mass was estimated to be over 7 kg/kW<sub>e</sub> with the balancer assembly included, giving similar characteristics as the single-cylinder FPSE/LA baseline design.

The efficiency and specific mass values for this concept include allocation for a displacer linear drive motor, which is required to stabilize the power module. The system is unstable without a displacer motor because, if the engine-alternator coupling is lost, there is no sink to dissipate engine power. With the addition of a reasonably robust displacer motor, the displacer power is absorbed and the system is stabilized. This requirement adds complexity to the power module and impacts the displacer drive and engine structural designs. The engine specific mass would increase to accommodate the motor in the pressure vessel.

Based on the displacer motor requirement and the failure of this configuration to improve on the baseline FPSE/LA performance characteristics, it is not recommended as a preferred configuration.

---

\*Based on available data for magnet properties at operating temperature, and assuming 60% coil packing factor. Requirements of high-temperature wire insulation may reduce available packing factor and increase alternator size.

Table 5-2. FPSE with Magnetic Coupling and Rotary Alternator - Summary

**Operating Conditions**

• Mean Pressure	13 MPa
• Frequency	75 Hz
• Temperature Ratio	2.0
• Stroke	31 mm

**Performance**

• Net Output Power	150 kW <sub>e</sub>
• Power Module Thermal Efficiency	30%
• Indicated Engine Efficiency	35%
• Mechanical Efficiency	94%
• Converter Efficiency	95%
• Alternator Efficiency	95%

**Specific Mass**

• Power Module (Total)	7.4 kg/kW <sub>e</sub>
• Engine	4.4 kg/kW <sub>e</sub>
• Converter	0.7 kg/kW <sub>e</sub>
• Alternator	1.0 kg/kW <sub>e</sub>
• Balancer	1.4 kg/kW <sub>e</sub>

## 6.0 MAXIMUM ACHIEVABLE POWER LEVEL PER CYLINDER

### 6.1 Task Objective

The objective of this task was to determine the maximum feasible electrical power output that can be achieved in a single-cylinder radial engine configuration under the following constraints:

- Heater-to-cooler wall temperature ratio of 2.0 (1050 K/525 K)
- Power module net thermal efficiency greater than or equal to 20%
- Design life of 7 years
- Maximum power module vibration level of 0.0038 cm
- Power module specific mass less than or equal to 10 kg/kW<sub>e</sub>.

### 6.2 Summary

The 150-kW<sub>e</sub> baseline power module configuration was analytically scaled up to 500 kW<sub>e</sub>. At this power level, the power module specific mass reached the design constraint of 10 kg/kW<sub>e</sub>. Higher power levels could not be achieved without exceeding the specified specific mass limit. The power module net thermal efficiency at this power level is predicted to be 25% (50% of Carnot). The limiting factors in the power scale-up are the increasing pressure-vessel specific mass and the heat exchanger pumping loss, which at the 500-kW<sub>e</sub> power level is over 40% of the net thermodynamic power generated by the engine. Figure 6-1 shows the layout of the 500-kW<sub>e</sub> engine. Table 6-1 shows the operating conditions and details of the engine geometry. Table 6-2 shows the predicted power module performance and specific mass breakdown.

### 6.3 Technical Discussion

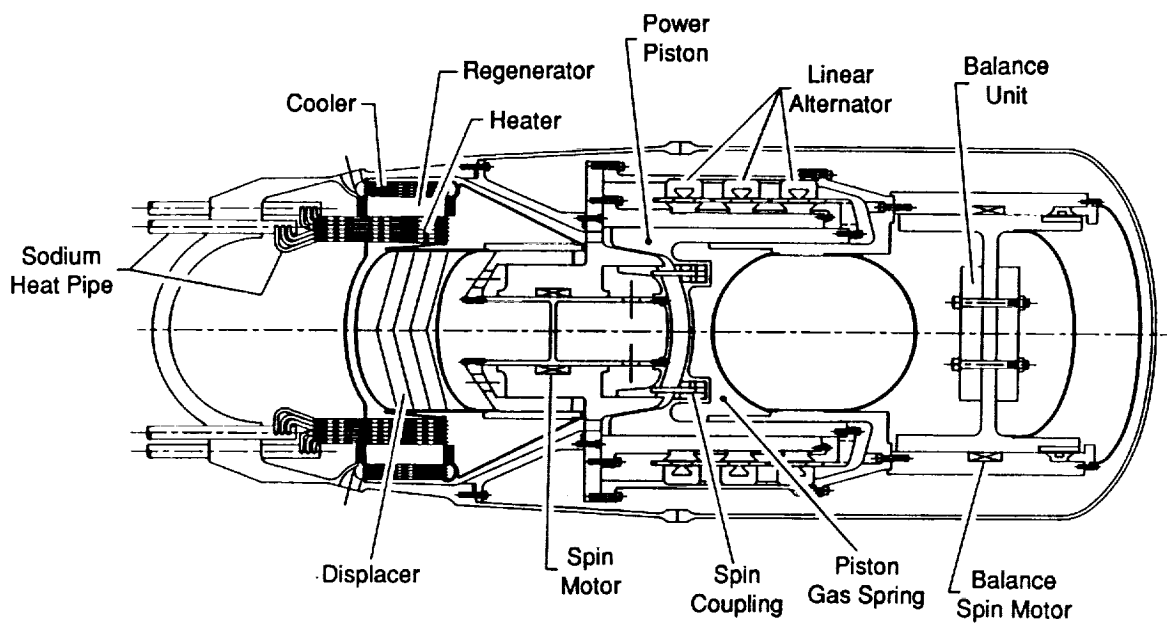
The computer codes developed during the first phase of the scaling study were used without modification. The power module scaling was performed under the following additional constraints:

- Minimum bearing length-to-diameter ratio = 1.0
- The displacer and power piston seal clearances increase linearly with diameter for sizes greater than 152 mm. At a diameter of 152 mm, the radial seal clearance was set at 12.7 μm. For concentric seals, as in the displacer drive, the outer seal clearance was increased by 30% to allow for tolerance stackups
- Maximum heat-pipe axial flux level = 4.5 kW/cm<sup>2</sup>.

The 150-kW<sub>e</sub> baseline power module design at a temperature ratio of 2.0 was analytically scaled up in 50-kW<sub>e</sub> increments. At each power point the engine geometry and operating parameters were optimized to maximize the ratio of power module efficiency to specific mass. Explanations for the decrease in power module performance (efficiency and specific power) with increasing power level are contained in the following subsections.

#### 6.3.1 Seal Clearances

Higher power levels require larger engine swept volume and therefore larger power piston and displacer diameters. From manufacturing considerations, larger piston and displacer diameters require larger seal clearances, as reflected in the seal clearance constraint mentioned above. Since the leakage loss varies with clearance cubed, the leakage loss increases much faster than the engine power. This results in a significant efficiency penalty with increasing power level. To limit the leakage losses to an acceptable



89781

Figure 6-1. 500-kW<sub>e</sub> FPSE/LA Layout



Table 6-1. 500-kW<sub>e</sub> Power Module Operating Conditions and Geometry

**Operating Conditions**

P <sub>m</sub> (bar)	125
Frequency (Hz)	70
Heater Wall Temperature (K)	1050
Cooler Wall Temperature (K)	525

**Geometry**

Engine Size (kW <sub>e</sub> )	500
Displacer Diameter (mm)	535
Piston Diameter (mm)	745
Displacer Amplitude (mm)	25.7
Piston Amplitude (mm)	22
Displacer/Piston Phase (deg)	80
Balance Piston Diameter (mm)	925
Balance Piston Amplitude (mm)	8.0

**Regenerator**

Frontal Area (cm <sup>2</sup> )	6280
Wire Diameter (μm)	25.4
Porosity (%)	84.9
Radial Length (mm)	63.8
Axial Length (mm)	250

**Heater**

Hydraulic Diameter (mm)	1.13
No. of Passages (-)	27,000
Frontal Area (cm <sup>2</sup> )	366
Surface Area (m <sup>2</sup> )	9.93
Effectiveness (%)	93
Effective Surface Area (m <sup>2</sup> )	9.20
Radial Length (mm)	76

**Cooler**

Hydraulic Diameter (mm)	0.45
No. of Passages (-)	117,000
Frontal Area (cm <sup>2</sup> )	681
Surface Area (m <sup>2</sup> )	16.3
Effectiveness (%)	85
Effective Surface Area (m <sup>2</sup> )	13.9
Radial Length (mm)	27.0

**Manifolds/Ducts**

Cold Volume (m <sup>3</sup> )	0.04
-------------------------------	------

Table 6-2. 500-kW<sub>e</sub> Power Module Performance Summary

Engine Pressure Amplitude (bar)	17.2
Heat Input (kW <sub>i</sub> )	1946
Indicated Power (kW)	624
Displacer Mechanical Loss (kW)	27.6
Piston Mechanical Loss (kW)	18.9
Balancer Loss Supplied by Engine (kW)	13
Gross Engine Power (kW)	564.5
Alternator Loss (kW)	51
Gross Alternator Power (kW)	513.5
Balancer Motor Power (kW)	13.5
Net Output Power (kW <sub>e</sub> )	500
Indicated Efficiency (%)	32.1
Net Thermal Efficiency (%)	25.7
Specific Mass Breakdown (kg/kW <sub>e</sub> )	
Pressure Vessel - Hot	1.15
Pressure Vessel - Cold	1.75
Heat Exchangers	1.13
Displacer Assembly	0.64
Piston Assembly	0.63
Structure	0.65
Alternator Assembly	1.31
Balancer Assembly	2.23
Miscellaneous	0.20
Total	9.69

level from a performance viewpoint, pressure amplitude in the engine is decreased with increasing power level (leakage losses are proportional to pressure amplitude squared). This results in an increase in specific mass with increasing power level.

### 6.3.2 Ratio of Bearing Length to Diameter

From purely performance considerations, scaling of power by area maintains a constant specific mass and efficiency over the power range. This is possible because the engine and gas spring pressure waves as well as the basic thermodynamic parameters (friction and heat transfer coefficients, fluid temperatures, and velocities) remain constant. However, in practice, scaling purely by area is not possible because of manufacturing, mechanical operation, and heat-input and heat-reject considerations. Consider a power piston reciprocating in a cylinder. Due to side loads on the power piston there is a tendency for the power piston to tilt about on its axis. If the tilt angle is large, the power piston can jam in the cylinder. One way to avoid the piston lock-up is to make the piston length-to-diameter ratio at least 1.0. Therefore, scaling power by area increase (strokes held fixed) under the minimum length-to-diameter constraint will result in a significant increase in specific mass with increase in power level. In order to limit the increase in specific mass to an acceptable level, the power piston, displacer, and vibration absorber strokes were increased with increasing power level, which resulted in higher gas spring losses. Gas spring stiffness is directly proportional to piston area and pressure amplitude, and is inversely proportional to stroke. Therefore, to compensate for the increase in stroke and decrease in piston area (relative to the piston area with constant stroke), the gas spring pressure amplitude must be increased, with an increase in gas spring losses.

### 6.3.3 Heat Pipes

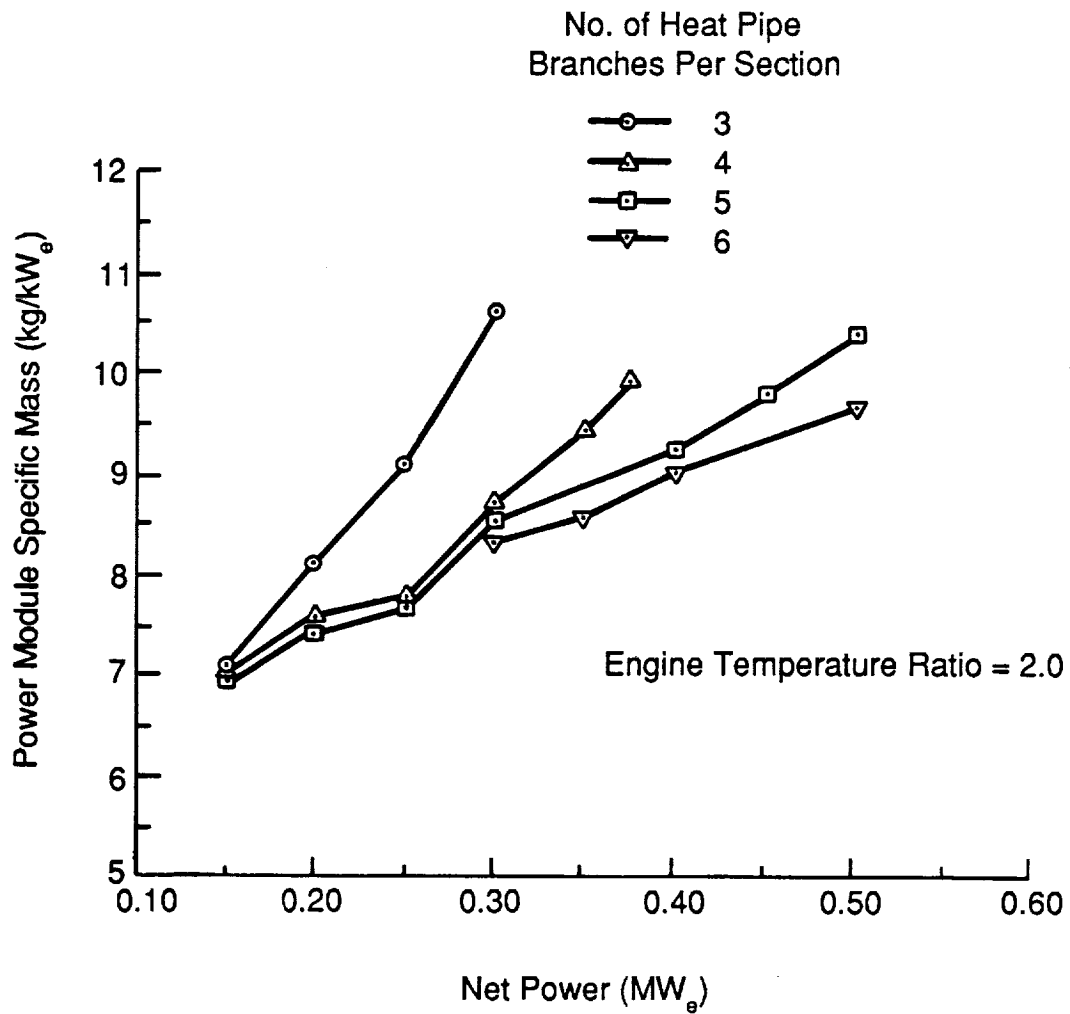
The required heat-pipe cross-sectional area increases linearly with increasing power level. Since the displacer diameter was not increased linearly with power level, the number of heat-pipe branches (per main heat pipe) had to be increased in the radial direction. The number of heat-pipe "legs" was increased from 3 at 150-kW<sub>e</sub> power level to 4 at 200 kW<sub>e</sub>, 5 at 300 kW<sub>e</sub>, and 6 at 500 kW<sub>e</sub>. However this resulted in an increased heater passage length, thereby increasing the heat exchanger pumping losses. Figures 6-2 and 6-3 show the power module specific mass and efficiency-versus-power level, with the number of heat-pipe legs in the radial direction as a parameter. As shown, rearrangement of the heat pipes becomes attractive when the power module specific mass can be reduced without an excessive efficiency penalty.

### 6.3.4 Heat Exchanger Relative Location

The heat exchanger assembly in the 150-kW<sub>e</sub> baseline design was positioned such that the top of the displacer dome was even with the middle of the heat exchanger. With increasing power level, the heat exchanger assembly was moved down relative to the displacer to decrease pressure vessel length. This modification also provided a more favorable manifold flow distribution.

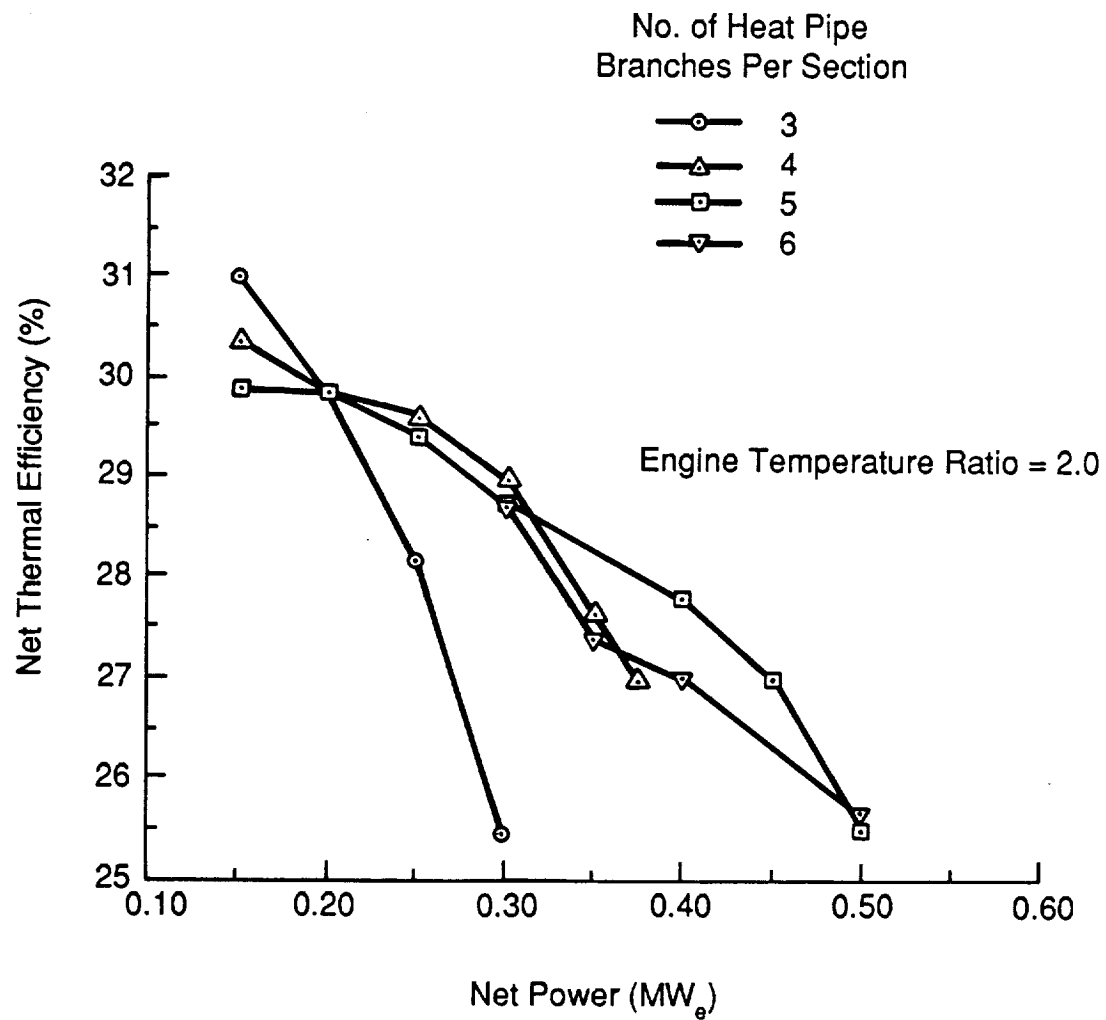
### 6.3.5 Vibration Absorber

The balancer stroke was increased with increasing power level to maintain reasonable specific mass. This resulted in increased balancer gas spring pressure amplitude, and therefore increased power loss. In order to meet the casing vibration constraint, the balancer drive motor power increased from 500 W at the 200-kW<sub>e</sub> power module power level, to 12 kW<sub>e</sub> at the 500-kW<sub>e</sub> power module power level.



89784

Figure 6-2. Single-Cylinder Power Module Scaleup Specific Mass versus Power Level



89783

Figure 6-3. Single-Cylinder Power Module Scaleup Efficiency versus Power Level

### 6.3.6 Alternator

The 150-kW<sub>e</sub> alternator configuration (three stator sections) was maintained for all higher power levels. Use of more than three sections was mechanically unattractive, and resulted in a large increase in plunger mass and overall specific mass.

### 6.4 Large-Engine Design Problems

Potential problem areas of the 500-kW<sub>e</sub> power module design that require further evaluation include the following.

- Although the seal clearance was increased linearly with piston (and displacer) diameter, maintaining tight tolerances at large diameters (635 mm) may present manufacturing difficulties.
- Thermal distortion may occur in large parts due to thermal gradients. Detailed thermal analysis must be performed to determine the effect of heat dissipation due to gas spring and seal leakage losses.
- High power loss may occur in the vibration absorber tuning motor. Detailed cooling analysis needs to be performed.
- Windage losses due to rotation of the displacer, power piston, alternator plunger, and vibration absorber need to be assessed.
- Increased performance uncertainty is present due to increased pumping losses. At the 500-kW<sub>e</sub> power level, pumping losses are as high as 40% of the indicated power. Therefore, net available power is very sensitive to uncertainties in friction coefficients and velocity head drops. If the pumping losses are limited to a maximum of 20% (upper limit in MTT's past designs) of indicated power, the maximum feasible power level would be only 250 kW<sub>e</sub>.

## 7.0 REFERENCES

1. Penswick, L. Barry: 1050 K Stirling Space Engine Design. NASA CR-182149, 1988.
2. Smith, J. Gerald: Nibron Nickel Boron Wear Resistant Coatings. Pure Coatings, Inc., West Palm Beach, Florida. 1983 ASM Metals Congress, Philadelphia, Pa., 1983.
3. Sinclair, J. H.: Compatibility of Several Iron, Cobalt, and Nickel-Base Alloys with Refluxing Potassium at 1800°F. NASA TM X-1617, Lewis Research Center, Cleveland, Ohio, August 1968.
4. Efficiency Standards for Stirling Engine Systems. A Proposal for Modifications to J. L. Crowley's paper (ORNL/CON-131) for adoption by the Stirling Engine Committee of the American Society of Mechanical Engineers, August 1986.
5. Crowley, J. L.: Efficiency Terms for Stirling Engines. ORNL/CON-31, June 1983.



National Aeronautics and  
Space Administration

## Report Documentation Page

1. Report No. CR182218	2. Government Accession No.	3. Recipient's Catalog No.	
4. Title and Subtitle  Space Power Free-Piston Stirling Engine Scaling Study		5. Report Date 1 October 1989	
		6. Performing Organization Code	
7. Author(s)  D. Jones		8. Performing Organization Report No. 89TR6	
		10. Work Unit No. 586-01-11	
9. Performing Organization Name and Address Mechanical Technology Incorporated 968 Albany-Shaker Road Latham, New York 12110		11. Contract or Grant No. NAS3-25148	
		13. Type of Report and Period Covered Contractor Final Report	
12. Sponsoring Agency Name and Address NASA-Lewis Research Center 21000 Brookpark Road Cleveland, Ohio 44135		14. Sponsoring Agency Code	
15. Supplementary Notes  Project Manager: Lanny Thieme, Power Technology Division, Mail Stop 301-2, Lewis Research Center			
16. Abstract  This report documents the design feasibility study of a single-cylinder, free-piston Stirling engine/linear alternator (FPSE/LA) power module generating 150 kW-electric (kW <sub>e</sub> ), and the determination of the module's maximum feasible power level. The study was conducted by Mechanical Technology Incorporated (MTI) for NASA-Lewis Research Center (NASA-LeRC) under contract No. NAS3-25148.  The power module configuration was specified to be a single-cylinder (single piston, single displacer) FPSE/LA, with tuning capacitors if required. The design requirements were as follows: <ul style="list-style-type: none"><li>• Maximum electrical power output</li><li>• Power module thermal efficiency <math>\geq 20\%</math> at a specific mass of 5 to 8 kg/kW<sub>e</sub></li><li>• Heater wall temperature/cooler wall temperature = 1050 K/525 K</li><li>• Sodium heat-pipe heat transport system; pumped loop NaK (sodium-potassium eutectic mixture) rejection system</li><li>• Maximum power module vibration amplitude = 0.0038 cm</li><li>• Design life = 7 years (60,000 hr).</li></ul>			
17. Key Words (Suggested by Author(s))  Stirling Engine      Linear Alternator Space Power      Dynamic Balancer Heat Pipe      Heat Engine			
19. Security Classif. (of this report) Unclassified		20. Security Classif. (of this page) Unclassified	
		21. No of pages 141	22. Price*



The results of the study show that a single-cylinder FPSE/LA is capable of meeting program goals and has attractive scaling attributes over the power range from 25 to 150 kW<sub>e</sub>. Scaling beyond the 150-kW<sub>e</sub> power level, the power module efficiency falls and the power module specific mass reaches 10 kg/kW<sub>e</sub> at a power output of 500 kW<sub>e</sub>.

A discussion of scaling rules for the engine, alternator, and heat transport systems is presented, along with a detailed description of the conceptual design of a 150-kW<sub>e</sub> power module that meets the requirements. Included is a discussion of the design of a dynamic balance system.

A parametric study of power module performance conducted over the power output range of 25 to 150 kW<sub>e</sub> for temperature ratios of 1.7, 2.0, 2.5, and 3.0 is presented and discussed. The results show that as the temperature ratio decreases, the efficiency falls and specific mass increases. At a temperature ratio of 1.7, the 150-kW<sub>e</sub> power module cannot satisfy both efficiency and specific mass goals. As the power level increases from 25 to 150 kW<sub>e</sub> at a fixed temperature ratio, power module efficiency is seen to increase slightly, but at the expense of increased specific mass. An empirical equation relating power module thermal efficiency as a function of power module specific mass, power output, and temperature ratio is developed.

Alternative configurations to the single-cylinder, direct-coupled linear alternator approach are also evaluated, but are shown to have technical drawbacks that lessen their attractiveness.

The dynamic balance assembly mass (moving mass and structure) represents 20 to 30% of the total single-cylinder power module mass. Joining two modules in a balanced opposed configuration eliminates the need for the balancer, and a hot-end junction can be made without significant addition of structural mass. Recommendations are made for evaluation of advanced heat pipe concepts, tests of radial-flow heat exchangers, and evaluation of high-temperature alternator materials.

